# Incremental Nonlinear Dynamic Inversion Controller Design for Autoland

Tim Hokke


TUDelft

Source: [1]

# Incremental Nonlinear Dynamic Inversion Controller Design for Autoland

Thesis report

by

Tim Hokke

to obtain the degree of Master of Science
at the Delft University of Technology
to be defended publicly on October 27th, 2025 at 14:00

*Thesis committee*:

| | |
|---|---|
| Chair: | Dr. ir. R. van Paassen |
| Supervisor: | Dr. ir. E. van Kampen |
| External examiner: | Dr. ir. E. Mooij |
| Place: | Faculty of Aerospace Engineering, Delft |
| Project Duration: | February, 2025 - October, 2025 |
| Student number: | 5072395 |

An electronic version of this thesis is available at `https://repository.tudelft.nl/`.

Faculty of Aerospace Engineering · Delft University of Technology

# Abstract

Autolanding remains a challenging task due to changing environmental conditions and the sensitivity of conventional control methods to model uncertainties and delays. This work investigates the application of Incremental Nonlinear Dynamic Inversion (INDI) to an autoland scenario using the PH-LAB Cessna Citation aircraft model. INDI reduces the model dependency by utilising sensor-based feedback, thereby enhancing robustness to modelling inaccuracies and external disturbances. Emphasis is placed on addressing variable sensor and actuator delays, which can degrade control accuracy and stability. The proposed INDI controller integrates multiple feedback loops and Pseudo-Control Hedging (PCH), complemented by a hybrid filter for angular acceleration estimation and a novel altitude estimator. The latter utilises linear accelerations measured by the IMU, which are subject to smaller delays than altitude measurements from the Digital Air Data Computer (DADC). This estimate is fused with the DADC altitude through a Kalman filter for improved accuracy and mitigation of cumulative errors. Simulation results demonstrate that the controller achieves safe landings under external disturbances and variable delays. Sensitivity analyses further show consistent performance across multiple scenarios, while identifying the controller's operational limits.

# Contents

# Nomenclature

**List of Abbreviations**

| | |
|---|---|
| $IAS$ | Indicated Airspeed |
| $TAS$ | True Airspeed |
| AC | Attitude Control |
| AD-INCA | Adaptive Dynamic Incremental Nonlinear Control Allocation |
| AHRS | Attitude Heading and Reference System |
| AHRS | Attitude and Heading Reference System |
| CE | Control Effectiveness |
| D-INCA | Dynamic Incremental Nonlinear Control Allocation |
| DADC | Digital Air Data Computer |
| DCM | Direction Cosine Matrix |
| DOF | Degree of freedom |
| EOM | Equations of Motion |
| FBW | Fly-By-Wire |
| FCS | Flight Control System |
| FTCS | Fault Tolerant Control System |
| FTIS | Flight Test Instrumentation System |
| GM | Gain Margin |
| IBS | Incremental Backstepping |
| ICE | Innovative Control Effectors |
| IFR | Instrument Flight Rules |
| INCA | Incremental Nonlinear Control Allocation |
| INDI | Incremental Nonlinear Dynamic Inversion |
| KF | Kalman Filtering |
| LMS | Least-Mean-Square |
| LTI | Linear Time Invariant |
| MINDI | Modified INDI |
| NDI | Nonlinear Dynamic Inversion |
| OBM | On-board Model |
| PCH | Pseudo Control Hedging |
| PID | Proportional-Integral-Derivative |
| PM | Phase Margin |
| RCAH | Rate Control Attitude Hold |
| REQ | Requirement |
| RLS | Recursive Least Squares |
| RMS | Root Mean Square |
| RMSE | Root Mean Square Error |
| RQ | Research Question |
| SISO | Single-Input Single-Output |
| TD | Time Delay |
| TDM | Time Delay Margin |
| TDS | Time Delay System |
| UAV | Unmanned Aerial Vehicle |
| V&V | Verification and Validation |
| VFR | Visual Flight Rules |

**List of Symbols**

| | |
|---|---|
| $\alpha$ | Angle of attack (deg) |
| $\beta$ | Angle of sideslip (deg) |
| $\delta_a$ | Aileron deflection (deg or rad) |
| $\delta_e$ | Elevator deflection (deg or rad) |
| $\delta_r$ | Rudder deflection (deg or rad) |
| $\Omega$ | Angular velocity (deg/s or rad/s) |
| $\phi$ | Bank angle (deg or rad) |
| $\psi$ | Yaw angle (deg or rad) |
| $u$ | Forward velocity component (m/s) |

| | |
|---|---|
| $v$ | Sideways velocity component (m/s) |
| $w$ | Vertical velocity component (m/s) |
| $\bar{c}$ | Mean aerodynamic chord (m) |
| $\boldsymbol{f}$ | State dynamics function |
| $\boldsymbol{u}$ | Input vector |
| $\boldsymbol{v}$ | Virtual control input |
| $\boldsymbol{x}$ | State vector |
| $\boldsymbol{y}$ | Output vector |
| $\Delta$ | Difference |
| $\gamma$ | Flight path angle (deg or rad) |
| **M** | Moment |
| $\omega$ | Angular rate (deg/s or rad/s) |
| $\omega_n$ | Natural frequency (Hz) |
| $\rho$ | Air density (kg/m$^3$) |
| $\sigma$ | Prandtl's interference coefficient |
| $\tau$ | Time delay (ms or s) |
| $\theta$ | Pitch angle (deg or rad) |
| $\zeta$ | Damping coefficient (-) |
| $a$ | Acceleration (m/s$^2$) |
| $f_x$, $f_y$, $f_z$ | IMU specific forces (g) |
| $I$ | Moment of Inertia (kg·m$^2$) |
| $J$ | Inertia matrix (kg·m$^2$) |
| $K$ | Gain (-) |
| $l$ | Roll moment |
| $m$ | Pitch moment |
| $n$ | Load factor (-) |
| $n$ | Yaw moment |
| $p$ | Roll rate (deg/s or rad/s) |
| $q$ | Pitch rate (deg/s or rad/s) |
| $r$ | Yaw rate (deg/s or rad/s) |
| $T_s$ | Sampling time (s) |
| $V$ | Velocity (m/s) |
| b | Wingspan (m) |
| D | Derivative gain (-) |
| I | Integrator gain (-) |
| M | Mach number (-) |
| P | Proportional gain (-) |
| S | Wing surface area (m$^2$) |
| T | Thrust (N) |

# List of Figures

# List of Tables

# 1 Introduction

This chapter introduces the Master of Science thesis report: ”Incremental Nonlinear Dynamic Inversion Controller Design for Autoland”, conducted at the Control & Simulation department of the Faculty of Aerospace Engineering, Delft University of Technology. Section 1.1 outlines the motivation for the project, while Section 1.2 defines the research objective and questions. Finally, Chapter 2 provides an overview of the planning and the report outline.

## 1.1. Motivation

Landing incidents remain a significant cause of accidents in aviation. According to the Annual Safety Review 2024 by EASA, in the time period of 2013-2022, 34.5% of accidents and serious incidents occurred during the approach and landing phase (18.2% and 16.3% respectively) [2]. In addition, in 2023, the percentage of accidents and serious incidents grew to 25.5% during landing. Moreover, loss of control has been the main or second cause of fatal accidents in the last decades [3]. Therefore, advanced control methods which are better able to cope with uncertainties and changing system dynamics during the landing phase have gained interest from the aviation industry, where nonlinear control techniques offer advantages.

Current flight control systems (FCSs) predominantly use linear controllers, which generally perform well under nominal flight conditions. However, linear controllers, such as PID, require gain scheduling around specific operating points, which can be labour-intensive and limits adaptability. Moreover, linear FCSs suffer from performance degradation in altering scenarios, such as gusty crosswinds or control surface failures. In contrast, nonlinear control techniques can better handle system nonlinearities, reducing the need for gain tuning and improving robustness against disturbances. Several nonlinear control methods are currently being developed, including Nonlinear Dynamic Inversion (NDI), adaptive control, Incremental Backstepping (IBS), and Incremental Nonlinear Dynamic Inversion (INDI) [4] [5]. NDI linearises system dynamics by inverting nonlinearities, forming a cascade of integrators that establishes a direct relationship between the virtual control input and system output [5]. While NDI can achieve good performance under accurate models, unmodeled dynamics or external disturbances can degrade its effectiveness.

INDI is a sensor-based control strategy that has demonstrated strong robustness against disturbances [6]. INDI addresses NDI’s limitations by computing incremental control updates, reducing the dependency on an accurate model while retaining NDI’s benefits. Rather than fully inverting system nonlinearities, it determines control adjustments ($\boldsymbol{\Delta u}$) based on local system behaviour, regulating the desired output and its derivatives while disregarding state-dependent terms. By utilising feedback from the system output’s derivatives, such as angular accelerations, INDI directly measures unmodelled effects and disturbances, allowing for their compensation in the subsequent control update. Unlike incremental backstepping, INDI does not require complex higher-order derivative computations, simplifying implementation while retaining robustness. This makes it a good candidate for handling the autoland task.

Although INDI has been successfully applied in flight tests for fixed-wing aircraft [7] [8], several challenges arise when adapting it to autolanding scenarios. Factors such as time delays, slower actuator and sensor dynamics, and lower control frequencies can compromise stability and performance [6] [9] [10]. Addressing these challenges is important for safe autoland, where precise control and timely responses are essential for a safe landing.

To contribute to the existing research on INDI, this study aims to develop an INDI controller for the autoland of the PH-LAB Cessna Citation platform in a simulated environment. The goal is to identify and investigate potential causes of stability and performance issues, such as delays and actuator limits, and propose solutions or mitigation methods to enhance the reliability of INDI in autoland scenarios.

## 1.2. Research Objective and Questions

The research objective is to build an INDI controller for autoland of the PH-LAB Cessna Citation platform in a simulated environment. Furthermore, the most important factors causing performance degradation and stability issues shall be identified. After this identification, methods to mitigate said problems shall be found and implemented for the INDI autoland control system. The research objective is used to define the main research question, which is subsequently divided into multiple sub-questions. The answers to the sub-questions and main question together form the contribution of this research. The proposed main question and sub-questions are as follows:

**Research Question Main**

Which measures are required to successfully mitigate the causes of performance degradation and stability issues in an INDI autoland system?

**Research Question 1**

What is the state-of-the-art in INDI and autoland systems?

**Research Question 2**

What are the requirements for the autoland system?

**Research Question 3**

What are the components/factors of the INDI autoland system that cause performance degradation, and how do they affect stability?

**Research Question 4**

What methods can mitigate performance degradation and stability issues in control systems, and how can they be adapted for INDI-based autoland?

## 1.3. Outline

After this introduction, the project plan follows in Chapter 2 along with a Gantt chart. The remainder of this report is divided into three parts. Part I is a standalone research paper, which presents all key findings.

Part II contains the reviewed literature and consists of five chapters. Chapter 3 presents the basic derivation of INDI, and several novel versions or adaptations. Chapter 4 introduces effects experienced during real-world applications, including delays, dynamic effects, noise, and bias. This is followed by time- and frequency-based stability analyses. Chapter 5 presents straight and curved approach paths applicable for autoland, and the physics behind the ground effect. The metrics used for controller evaluation are introduced in Chapter 6. Finally, Chapter 7 presents the aircraft-specific characteristics and the design requirements.

Part III contains all additional results. Chapter 8 presents the design and tradeoff of two fusion filter options. Chapter 9 contains the Verification and Validation procedure carried out for the aircraft model and controller. Chapter 10 presents the modelling and influence on performance due to real-world factors,

followed by a summary of the requirement compliance. The report is completed by Chapter 11, presenting the conclusions and recommendations.

# 2

# Project Plan

For the research to be successful, a project plan has been created. This begins with the methodology, where the plan behind answering the Research Questions as defined in Section 1.2 is presented. For all research questions, the approach is clarified, after which a comprehensive list of tasks is provided. Next, the expected results from the research are illustrated hypothetically. Finally, the planning of the entire research is shown using a Gantt chart.

## 2.1. Methodology

The methodology outlined in this chapter is designed to systematically address all research questions, leading to an answer to the main research question and satisfying the research objective. The approach consists of a progression from understanding the current state of INDI and autoland systems, defining the necessary system requirements, identifying sources of performance degradation, and developing mitigation strategies to enhance performance and stability. This is achieved through a combination of literature review, mathematical modelling, sensitivity analyses, and simulation-based verification and validation.

Each section of this chapter corresponds to a research question, ensuring a logical flow towards developing an INDI-based autoland controller. In addition, tasks are defined for each research question which serve as guidance for the project planning (see Section 2.3). The methodology begins with a review of existing research (RQ1) to establish a foundation for defining the system's requirements (RQ2). An analysis of factors affecting system performance and stability (RQ3) is then conducted, followed by the exploration and implementation of mitigation strategies (RQ4). Finally, the controller is synthesised, tested in a simulation environment, and compared to other controllers to evaluate its effectiveness.

### 2.1.1. Research Question 1

Finding the state-of-the-art in INDI and autoland systems is essential to ensure a meaningful contribution to existing research. A comprehensive literature review is conducted, analysing Incremental Nonlinear Dynamic Inversion (INDI), its advantages over other nonlinear control methods, and its application in aircraft control. Additionally, current autoland systems are reviewed, highlighting their limitations and identifying research gaps related to performance degradation and stability in INDI-based autoland. Sources include academic publications, industry reports, and flight test studies to ensure a well-rounded understanding. The remainder of the literature review supports the research motivation, introduces potential solutions, and provides an overview of the PH-LAB Cessna Citation, the platform used in this study.

*Tasks:*

- Perform literature review on INDI and autoland systems

### 2.1.2. Research Question 2

Following the literature review, the requirements for the INDI autoland system are defined. These requirements are derived from regulatory guidelines, such as EASA and FAA standards for autoland systems, as well as aircraft-specific constraints for the PH-LAB Cessna Citation platform. Performance metrics, such as touchdown accuracy, velocity and disturbance rejection properties are considered. Safety aspects are also taken into account to ensure compliance with aviation standards. This phase is used to evaluate the control system under safe operational limits.

*Tasks:*

- Perform literature review on aircraft performance
- Read certification documents
- Make a list of requirements

### 2.1.3. Research Question 3

The next step involves identifying the components and factors that contribute to performance degradation and stability issues in an INDI autoland system. First, potential issues are identified based on findings from the literature review (RQ1), supplemented by further analysis of system behaviour. A mathematical model of the INDI control laws is developed without sensor dynamics and actuator limitations. Once stability is confirmed, these factors are incrementally incorporated to analyse their effects. Sensitivity analyses are conducted to assess the impact of delays, noise and bias, and disturbances on system stability. Simulation-based testing is used to analyse various degradation scenarios, including the effects of sensor noise, actuator limitations such as rate limits and saturation, and environmental disturbances. The results of this analysis provide a basis for developing mitigation strategies to enhance system performance.

*Tasks:*

- Basic INDI model creation
- Include sensor dynamics and actuator limits
- Sensitivity analysis on the basic model
- Sensitivity analysis on the complete model

### 2.1.4. Research Question 4

To address these challenges, various control enhancement methods are explored. These include filtering techniques to improve sensor signal quality, compensation methods for actuator dynamics and delays, and control techniques designed to handle uncertainties and disturbances. Additionally, hybrid approaches that incorporate adaptive elements are considered to further improve stability and performance. The effectiveness of these methods is evaluated through simulations in MATLAB/Simulink. Stability is assessed using analytical methods when possible. Finally, the findings from the previous steps are integrated into the final INDI autoland control system. This involves synthesising the controller while incorporating the selected mitigation strategies and verifying its performance in a simulated environment. The controller is tested against the predefined requirements to ensure it meets the necessary performance criteria.

*Tasks:*

- Include mitigation methods in the model (Alternative INDIs)
- Test new models
- Sensitivity analysis on new models
- Select final model
- Evaluate basic and final model

## 2.2. Expected Results

The expected outcome of this study is that the initial implementation of the INDI-based autoland controller will perform well under nominal conditions, demonstrating stable and reasonably accurate trajectory tracking. However, once sensor dynamics such as delays, noise and bias, and filtering effects are introduced, a decline in performance is expected. This degradation may lead to an increased tracking error, lag, or potential instability, highlighting the limitations of a standard INDI controller in autoland scenarios. Additionally, the landing phase itself is expected to introduce challenges, including rapid altitude transitions and environmental disturbances such as turbulence. These factors may necessitate modifications to the controller earlier than initially anticipated.

To address these issues, mitigation strategies such as filtering techniques, actuator compensation methods, and control adaptations will be explored. It is expected that these measures will improve stability and disturbance rejection, allowing the controller to maintain adequate performance when taking into account

sensor dynamics and environmental uncertainties. The final version of the controller should be able to follow the reference trajectory satisfactorily while ensuring a safe and precise landing in line with the defined requirements. Given the iterative nature of controller development, it is likely that additional refinements will be necessary as new challenges emerge throughout the testing process. Ultimately, the study aims to demonstrate that an INDI-based autoland system, with the appropriate modifications, can provide enhanced performance and reliability compared to traditional approaches.

## 2.3. Planning

The project planning is visualised using a Gantt chart (Figure 2.1). Tasks are defined and divided based on deadlines and were meant to guide the project. While this planning is not entirely fixed, it provides an overview of the tasks and the duration spent on each.

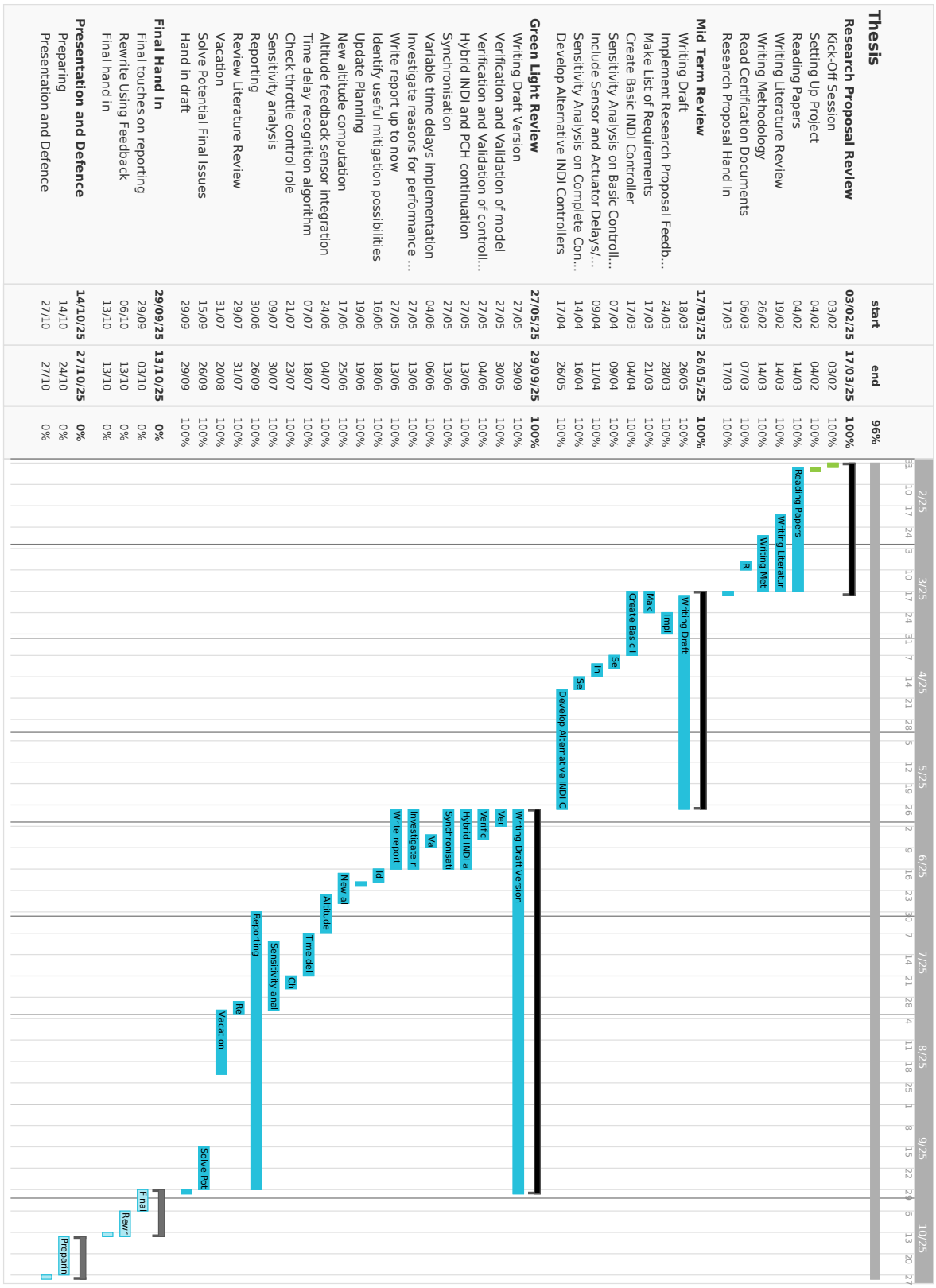


**Figure 2.1:** Gantt chart with planning

# Part I

## Research Paper

# Incremental Nonlinear Dynamic Inversion Controller Design for Autoland

T.P. Hokke *
*Delft University of Technology, Delft, Zuid-Holland, 2629 HS, the Netherlands*

**Autolanding remains a challenging task due to changing environmental conditions and the sensitivity of conventional control methods to model uncertainties and delays. This work investigates the application of Incremental Nonlinear Dynamic Inversion (INDI) to an autoland scenario using the PH-LAB Cessna Citation aircraft model. INDI reduces the model dependency by utilising sensor-based feedback, thereby enhancing robustness to modelling inaccuracies and external disturbances. Emphasis is placed on addressing variable sensor and actuator delays, which can degrade control accuracy and stability. The proposed INDI controller integrates multiple feedback loops and Pseudo-Control Hedging (PCH), complemented by a hybrid filter for angular acceleration estimation and a novel altitude estimator. The latter utilises linear accelerations measured by the IMU, which are subject to smaller delays than altitude measurements from the Digital Air Data Computer (DADC). This estimate is fused with the DADC altitude through a Kalman filter for improved accuracy and mitigation of cumulative errors. Simulation results demonstrate that the controller achieves safe landings under external disturbances and variable delays. Sensitivity analyses further show consistent performance across multiple scenarios, while identifying the controller's operational limits.**

## Nomenclature

| | | |
|---|---|---|
| $D$ | = | Derivative gain (-) |
| $h$ | = | Altitude (m); $\dot{h}$ Vertical speed (m/s) |
| $I$ | = | Integrator gain (-) |
| $J$ | = | Inertia matrix (kg$\cdot$ m$^2$) |
| $M$ | = | Mach number (-) |
| $m$ | = | Aircraft mass (kg) |
| $P$ | = | Proportional gain (-) |
| $R$ | = | Rotation matrix |
| $S$ | = | Wing surface area (m$^2$) |
| $T_{\max}$ | = | Maximum thrust (N) |
| $\boldsymbol{u}$ | = | Input vector |
| $V$ | = | Airspeed (m/s) |
| $b$ | = | Wingspan (m) |
| $\bar{c}$ | = | Mean aerodynamic chord (m) |
| $C_l, C_m, C_n$ | = | Aerodynamic moment coefficients (-) |
| $f_x, f_y, f_z$ | = | IMU specific forces (g) |
| $p, q, r$ | = | Body angular rates roll/pitch/yaw (deg/s or rad/s) |
| $v$ | = | Virtual control (multiple) |
| $\boldsymbol{x}$ | = | State vector |
| $\boldsymbol{y}$ | = | Output vector |
| $\Delta t$ | = | Time step (s) |

*Graduate student, Faculty of Aerospace Engineering, Control and Simulation Division, Delft University of Technology

| | | |
|---|---|---|
| $\alpha$ | = | Angle of attack (rad) |
| $\beta$ | = | Sideslip angle (rad) |
| $\delta_a, \delta_e, \delta_r$ | = | Aileron, elevator and rudder deflection (deg or rad) |
| $\gamma$ | = | Flight path angle (deg or rad) |
| $\rho$ | = | Air density (kg/m$^3$) |
| $\tau$ | = | Time delay (s or ms) |
| $\theta, \phi, \psi$ | = | Euler attitude angles (deg or rad) |
| $\dot{\theta}, \dot{\phi}, \dot{\psi}$ | = | Euler angle rates (deg/s or rad/s) |

**Acronyms**

| | | |
|---|---|---|
| DADC | = | Digital Air Data Computer |
| DCM | = | Direction Cosine Matrix |
| IAS | = | Indicated Airspeed |
| IMU | = | Inertial Measurement Unit |
| INDI | = | Incremental Nonlinear Dynamic Inversion |
| NDI | = | Nonlinear Dynamic Inversion |
| PCH | = | Pseudo-Control Hedging |
| RMS | = | Root Mean Square |
| TAS | = | True Airspeed |

**Notation**

| | | |
|---|---|---|
| $(\cdot)_c$ | = | Commanded |
| $(\cdot)_f$ | = | Filtered |
| $(\cdot)_s$ | = | Sensor measurement |
| $(\cdot)_0$ | = | Previous value |
| $(\cdot)^\wedge$ | = | Estimate |
| $\dot{(\cdot)}$ | = | Time derivative |

# I. Introduction

The aerospace industry's increasing focus on autonomous flight systems necessitates the development of robust and reliable control laws, particularly for critical flight phases such as takeoff and landing. Autoland systems in modern aircraft are designed for nominal operating conditions and may struggle to cope with unforeseen circumstances such as strong external disturbances or control surface failures. To address these limitations, nonlinear control techniques offer improved robustness and adaptability. One such nonlinear control method applicable during autoland is Incremental Nonlinear Dynamic Inversion (INDI). INDI preserves the advantages over closely related Nonlinear Dynamic Inversion (NDI) while reducing model dependency. This reduced reliance makes INDI computationally efficient and ensures consistent performance across the flight envelope without the need for repeated gain adjustments.

In recent years, INDI has attracted significant attention, with over 1500 publications as of 2024 [1]. Rather than explicitly inverting system nonlinearities, control adjustments are determined based on local system behaviour, regulating the desired output and its derivatives while neglecting state-dependent terms [2]. Although INDI has been successfully demonstrated in flight tests for fixed-wing aircraft, several challenges arise when applying it to autoland scenarios [3] [4]. Factors such as delays, slower actuator and sensor dynamics, and lower control frequencies can lead to degraded performance and reduced stability margins [5] [6] [7]. These challenges become particularly important during autoland, where precise control and timely responses are essential for a safe touchdown. Moreover, research has shown that synchronisation between angular acceleration feedback and control deflection measurements is crucial for performance, as unsynchronised signals lead to oscillatory behaviour [3] [8] [9]. To contribute to this ongoing research, this paper investigates the application of INDI to the PH-LAB Cessna Citation aircraft model in an autoland scenario.

The main contributions of this paper are threefold: 1) the design and implementation of a longitudinal INDI

controller for the PH-LAB Cessna Citation aircraft during an autoland simulation scenario, covering approach and flare, 2) an analysis of the main causes of performance degradation, and 3) the development and integration of a novel IMU-based altitude estimation method to reduce the effective delay in the altitude feedback.

The outline of this paper is as follows. First, section II provides a derivation of the theoretical foundations of INDI. Section III details the controller design and the gain tuning procedure. Next, section IV explains the time delay problem and presents the IMU-based altitude method and Kalman filter implementation. The simulation results and sensitivity analyses are presented in section V. Finally, section VI provides the conclusions and future recommendations.

## II. Incremental Nonlinear Dynamic Inversion

INDI has been derived through various approaches in literature. One commonly used formulation is sensor-based and relies on direct measurements to account for system dynamics, while an alternative formulation utilises an onboard model to represent the system behaviour. By implementing a complementary filter to fuse these two signals, Hybrid INDI is obtained.

### A. Sensor-based INDI

The state vector and output vector are defined as follows

$$\dot{\boldsymbol{x}} = \boldsymbol{f}(\boldsymbol{x}(t), \boldsymbol{u}(t)) \tag{1}$$

$$\boldsymbol{y} = \boldsymbol{h}(\boldsymbol{x}(t)) \tag{2}$$

with state vector $\boldsymbol{x}(t) \in \mathbb{R}^n$, output vector $\boldsymbol{y}(t) \in \mathbb{R}^r$, and input vector $\boldsymbol{u}(t) \in \mathbb{R}^m$. Applying a first-order Taylor series expansion to the system dynamics and neglecting higher-order terms yields:

$$\dot{\boldsymbol{x}} = \underbrace{\boldsymbol{f}(\boldsymbol{x}_0, \boldsymbol{u}_0)}_{\dot{\boldsymbol{x}}_0} + \left.\frac{\partial \boldsymbol{f}}{\partial \boldsymbol{x}}\right|_{\boldsymbol{x}_0,\boldsymbol{u}_0} (\boldsymbol{x} - \boldsymbol{x}_0) + \left.\frac{\partial \boldsymbol{f}}{\partial \boldsymbol{u}}\right|_{\boldsymbol{x}_0,\boldsymbol{u}_0} (\boldsymbol{u} - \boldsymbol{u}_0) \tag{3}$$

Differentiating Eq. (2) with the chain rule and subsequently substituting Eq. (3) yields:

$$\begin{aligned} \dot{\boldsymbol{y}} &= \left.\frac{\partial \boldsymbol{h}}{\partial \boldsymbol{x}}\right|_{\boldsymbol{x}_0} \dot{\boldsymbol{x}} \\ \dot{\boldsymbol{y}} &= \left.\frac{\partial \boldsymbol{h}}{\partial \boldsymbol{x}}\right|_{\boldsymbol{x}_0} \dot{\boldsymbol{x}}_0 + \left.\frac{\partial \boldsymbol{h}}{\partial \boldsymbol{x}}\right|_{\boldsymbol{x}_0} \left.\frac{\partial \boldsymbol{f}}{\partial \boldsymbol{x}}\right|_{\boldsymbol{x}_0,\boldsymbol{u}_0} (\boldsymbol{x} - \boldsymbol{x}_0) + \left.\frac{\partial \boldsymbol{h}}{\partial \boldsymbol{x}}\right|_{\boldsymbol{x}_0} \left.\frac{\partial \boldsymbol{f}}{\partial \boldsymbol{u}}\right|_{\boldsymbol{x}_0,\boldsymbol{u}_0} (\boldsymbol{u} - \boldsymbol{u}_0) \end{aligned} \tag{4}$$

The time separation principle is used to reduce complexity and model dependency. This principle assumes that the aircraft state changes at a much slower rate than the actuator states. Mathematically, this means that $\frac{\partial \boldsymbol{f}}{\partial \boldsymbol{x}}|_{\boldsymbol{x}_0,\boldsymbol{u}_0} \Delta\boldsymbol{x} \ll \frac{\partial \boldsymbol{f}}{\partial \boldsymbol{u}}|_{\boldsymbol{x}_0,\boldsymbol{u}_0} \Delta\boldsymbol{u}$ such that the second term in Eq. (4) can be neglected. The resulting equation is:

$$\begin{aligned} \dot{\boldsymbol{y}} &= \underbrace{\left.\frac{\partial \boldsymbol{h}}{\partial \boldsymbol{x}}\right|_{\boldsymbol{x}_0} \dot{\boldsymbol{x}}_0}_{\dot{\boldsymbol{y}}_0} + \underbrace{\left.\frac{\partial \boldsymbol{h}}{\partial \boldsymbol{x}}\right|_{\boldsymbol{x}_0} \left.\frac{\partial \boldsymbol{f}}{\partial \boldsymbol{u}}\right|_{\boldsymbol{x}_0,\boldsymbol{u}_0}}_{\boldsymbol{B}(\boldsymbol{x}_0,\boldsymbol{u}_0)} \underbrace{(\boldsymbol{u} - \boldsymbol{u}_0)}_{\Delta\boldsymbol{u}} \\ \dot{\boldsymbol{y}} &= \dot{\boldsymbol{y}}_0 + \boldsymbol{B}(\boldsymbol{x}_0, \boldsymbol{u}_0)\Delta\boldsymbol{u} \end{aligned} \tag{5}$$

The incremental dynamics are inverted by computing the inverse of the control effectiveness matrix ($\boldsymbol{B}(\boldsymbol{x}_0, \boldsymbol{u}_0)$), allowing the command increments $\Delta\boldsymbol{u}$ to be determined from the difference between the pseudo-command $\dot{\boldsymbol{y}}_c = \boldsymbol{\nu}$ and the measured output derivative. Note that the output and input vectors are assumed to be of equal dimension ($r = m$) and $\boldsymbol{B}(\boldsymbol{x}_0, \boldsymbol{u}_0)$ to be full rank, such that it is invertible. This results in:

$$\Delta\boldsymbol{u}_c = \boldsymbol{B}(\boldsymbol{x}_0, \boldsymbol{u}_0)^{-1}(\boldsymbol{\nu} - \dot{\boldsymbol{y}}_0) \tag{6}$$

The commanded control input is then obtained by adding the computed command increments to the previous control input $\boldsymbol{u}_0$:

$$\boldsymbol{u}_c = \boldsymbol{u}_0 + \Delta\boldsymbol{u}_c \tag{7}$$

**B. Hybrid INDI**

As an angular accelerometer is not standard equipment for the PH-LAB Cessna Citation aircraft, $\dot{q}$ cannot always be obtained by measurement. Therefore, a Hybrid INDI approach is employed. Hybrid INDI fuses the gyroscope measurement of $q$ with the model-based angular acceleration $\dot{q}_{mod}$ through a complementary filter to estimate $\dot{q}$. Both signals differ from the true state, since the sensor signal $q_s$ is affected by noise and sensor dynamics, while $\dot{q}_{mod}$ depends on aerodynamic coefficients and may not capture all dynamics and external disturbances.

The rotational equations of motion can be described by Eq. (8) [9].

$$\begin{bmatrix} \dot{p} \\ \dot{q} \\ \dot{r} \end{bmatrix} = \mathbf{J}^{-1} \left\{ \begin{bmatrix} \frac{1}{2}\rho V^2 S b C_l \\ \frac{1}{2}\rho V^2 S \bar{c} C_m \\ \frac{1}{2}\rho V^2 S b C_n \end{bmatrix} - \begin{bmatrix} p \\ q \\ r \end{bmatrix} \times \left( \mathbf{J} \begin{bmatrix} p \\ q \\ r \end{bmatrix} \right) \right\} \tag{8}$$

where $\mathbf{J}$ is the inertia matrix. Since only the pitch rate derivative is of interest here and $p$ and $r$ can be assumed negligible, this expression simplifies to:

$$\begin{aligned} \dot{q} &= \frac{1}{I_{yy}} (\frac{1}{2}\rho V^2 S \bar{c} C_m) - \underbrace{(J_{xx} p - J_{xz} r) r - (-J_{xz} p + J_{zz} r) p}_{\approx 0} \\ &\approx \frac{1}{I_{yy}} (\frac{1}{2}\rho V^2 S \bar{c} C_m) = \dot{q}_{mod} \end{aligned} \tag{9}$$

which is the equation used for the modelled pitch rate derivative. Parameters $C_m$ and $I_{yy} = \mathbf{J}_{yy}$ are taken from the aircraft model.

As illustrated in Figure 1, the model output $\dot{q}_{mod}$ is combined with the gyroscope measurement $q_s$ through a complementary filter [10]. There is an integral block in the feedback signal since the estimate is a derivative of the sensor measurement. The innovation signal $i$ represents the discrepancy between the measured and estimated angular rate and serves as corrective feedback to adjust the estimated angular acceleration, ensuring that the model-based predictions remain consistent with sensor data without the need for explicit differentiation.

The dynamics in the Laplace domain to estimate the angular acceleration can be described as:

$$\dot{q}_{est} = (q_s - \dot{q}_{est} \frac{1}{s})(P + \frac{I}{s}) + \dot{q}_{mod} \tag{10}$$

with P a proportional gain and I an integrator gain. This can be rearranged to

$$\dot{q}_{est} = S(s) q_s + M(s) \dot{q}_{mod} \tag{11}$$

where

$$S(s) = \frac{Ps + I}{s^2 + Ps + I} s, M(s) = \frac{s^2}{s^2 + Ps + I} \tag{12}$$

The factor $s$ in the sensor transfer function represents an implicit differentiation of the measured rate $q_s$, ensuring that the sensor contribution has the same physical units as $\dot{q}_{mod}$. Analytically, the transfer functions satisfy $\frac{1}{s} S(s) + M(s) = 1$ which confirms the consistency of the derivation in the Laplace domain.

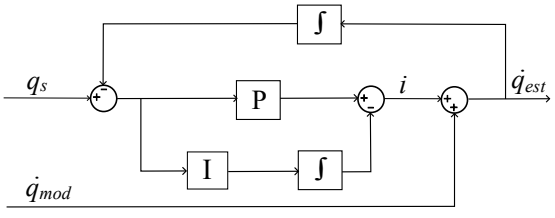


**Fig. 1 Hybrid INDI filter**

$S(s)$ acts as a low-pass filter on the sensor measurement $q_s$, smoothing high-frequency noise while preserving the aircraft dynamics. $M(s)$ acts as a high-pass filter on the model output $\dot{q}_{mod}$, allowing the system to respond quickly to control inputs. This complementary filtering allows Hybrid INDI to retain the robustness of sensor-based INDI against model uncertainties while providing a fast response to disturbances and control commands. Reducing the cutoff frequency increases noise attenuation but slows the system's response.

## III. Controller Design

The controller consists of three loops: pitch rate control, pitch angle control, and altitude control, complemented by a separate throttle-driven velocity control loop. For this study, the simulated aircraft is assumed to be aligned with the centerline of the landing strip at the start of the approach phase. As a result, the focus is solely on the longitudinal dynamics, meaning that controlling pitch and velocity is sufficient to analyse and mitigate performance degradation and stability issues in the control system. Elevator deflection limits were set to 15° (≈ 0.26 radians) and -17° (≈ −0.30 radians) [3].

### A. Attitude Loops

The pitch rate inner loop is based on Euler's equations of motion, see Eq. (8). When observing Eq. (6), the $B(x_0, u_0)$ matrix must be obtained (Eq. (13)). Substituting in Eq. (6) then gives Eq. (14) with the remaining variables defined as in Eq. (15). As only pitch rate control is considered in this research, exclusively $\Delta\delta_e$ is controlled, and the other two control surfaces remain in trim position.

$$\boldsymbol{B}(\boldsymbol{x}_0, \boldsymbol{u}_0) = J^{-1}\, \tfrac{1}{2}\rho V^2 S \begin{bmatrix} bC_{l_{\delta_a}} & 0 & bC_{l_{\delta_r}} \\ 0 & \bar{c}C_{m_{\delta_e}} & 0 \\ bC_{n_{\delta_a}} & 0 & bC_{n_{\delta_r}} \end{bmatrix} \tag{13}$$

$$\boldsymbol{\Delta u} = \frac{2J}{\rho V^2 S} \begin{bmatrix} bC_{l_{\delta_a}} & 0 & bC_{l_{\delta_r}} \\ 0 & \bar{c}C_{m_{\delta_e}} & 0 \\ bC_{n_{\delta_a}} & 0 & bC_{n_{\delta_r}} \end{bmatrix}^{-1} (\boldsymbol{\nu} - \dot{\boldsymbol{\omega}}_0) \tag{14}$$

$$\boldsymbol{\nu} = \begin{bmatrix} \nu_{\dot{p}} \\ \nu_{\dot{q}} \\ \nu_{\dot{r}} \end{bmatrix}, \quad \dot{\boldsymbol{\omega}} = \begin{bmatrix} \dot{p} \\ \dot{q} \\ \dot{r} \end{bmatrix}, \quad \boldsymbol{\Delta u} = \begin{bmatrix} \Delta\delta_a \\ \Delta\delta_e \\ \Delta\delta_r \end{bmatrix} \tag{15}$$

The output of the slower outer attitude control loop is used as input for the faster pitch rate controller. The relation between the attitude angles $\phi$, $\theta$ and $\psi$, and angular rates $p$, $q$ and $r$ is denoted in Eq. (16). This is a kinematic relationship independent of aircraft characteristics, hence NDI can be used instead of INDI.

$$\begin{bmatrix} \dot{\phi} \\ \dot{\theta} \\ \dot{\psi} \end{bmatrix} = \begin{bmatrix} 1 & \sin\phi\tan\theta & \cos\phi\tan\theta \\ 0 & \cos\phi & -\sin\phi \\ 0 & \sin\phi\sec\theta & \cos\phi\sec\theta \end{bmatrix} \begin{bmatrix} p \\ q \\ r \end{bmatrix} \tag{16}$$

To obtain the outer NDI loop, one inverts the previously given relation, and the attitude rates are replaced by virtual control inputs. This results in Eq. (17):

$$\begin{bmatrix} p_c \\ q_c \\ r_c \end{bmatrix} = \begin{bmatrix} 1 & 0 & -\sin\theta \\ 0 & \cos\phi & \sin\phi\cos\theta \\ 0 & -\sin\phi & \cos\phi\cos\theta \end{bmatrix} \begin{bmatrix} \nu_p \\ \nu_q \\ \nu_r \end{bmatrix} \tag{17}$$

Since only longitudinal is considered, $p_c = r_c = 0$, and under the small angle approximation, this reduces to:

$$q_c \approx \nu_q = K_{P\theta}(\nu_\theta - \theta_s) \tag{18}$$

As the outer attitude loop is slower than the inner pitch rate loop, the gain will be lower. Furthermore, the relation between the attitude loop and the altitude loop is similar, again with a gain after computing the error between the commanded altitude and the actual altitude, which then provides the input to the attitude loop. The commanded altitude calculation and gain selection will be presented later in subsection III.E.

### B. Velocity Loop

The velocity loop is used to control the thrust level of the aircraft. The thrust level is a separate control variable not included in the pitch control design. The process is very similar to the pitch control, with an inner INDI loop on the acceleration ($\dot{V}$) and a proportional gain on the difference between the desired velocity and the actual velocity. The used control law is [11]:

$$\delta_t = \delta_{t0} + B_{\dot{V}}^{-1}(\nu_V - \dot{V}_0) \tag{19}$$

where $B_{\dot{V}}^{-1} = \frac{T_{max}}{m}$ with $T_{max}$ the maximum thrust and $m$ the aircraft mass. When one ascends or descends, the True Airspeed ($V_{TAS}$) automatically changes due to an increase/loss of potential energy and alternating density. Because of this, the Indicated Airspeed ($V_{IAS}$) is implemented for the velocity control loop. This leads to more stable results as $V_{TAS}$ is directly linked to the altitude via $\dot{h}$, but $V_{IAS}$ is not. The control loop structure is shown in Figure 2, with the desired thrust output, $\dot{V}_{IAS}$ and $V_{IAS}$ as feedback signals and $V_{ref}$ as a controlled reference variable. The proportional gain P is tuned for a smooth transition in velocity based on thrust.

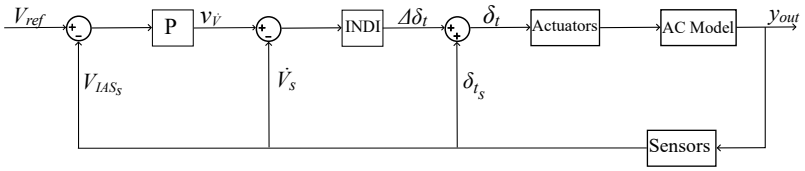


**Fig. 2 Velocity control loop**

### C. Pseudo-Control Hedging

The actuator transport delay present in the aircraft can cause oscillatory elevator deflection behaviour, potentially resulting in actuator saturation due to physical limits [12]. Pseudo-Control Hedging (PCH) may be used to address this problem [3] [7]. With PCH, a reference model is modified such that the inversion law does not adapt through actuator delays or saturation [13]. The reference model enforces desired first-order dynamics on the pseudo-control signal. Moreover, the derivative of the command signal can be used as a feedforward term. The dynamics of the reference model are defined by

$$\nu_{\dot{q}_{rm}} = P_{rm}(\nu_q - \nu_{q_{rm}}) \tag{20}$$

$$\nu_{q_{rm}} = \frac{1}{s}(\nu_{\dot{q}_{rm}} - \nu_h) \tag{21}$$

The subscript $rm$ indicates the reference model. $P_{rm}$ introduces a new tunable variable which adapts the error dynamics before inverting. $\nu_h$ is the pseudo-control hedge and denotes the difference between the commanded elevator deflection $\delta_{e_c}$ and the achieved elevator deflection $\delta_{e_0}$ to quantify the unachievable portion of the pseudo-control. Subtracting $\nu_h$ from the reference model input causes the reference model to track the achievable pseudo-control rather than the commanded pseudo-control. The pseudo-control hedge is obtained by using the control effectiveness:

$$\nu_h = I^{-1}\frac{1}{2}\rho V^2 \bar{c} C_{m_{\delta e}}(\delta_{e_c} - \delta_{e_0}) = G(\delta_{e_c} - \delta_{e_0}) \tag{22}$$

The original INDI changes from:

$$\delta_{e_c} = \delta_{e_0} + G^{-1}(\nu_{\dot{q}} - \dot{q}_0) \tag{23}$$

to:

$$\delta_{e_c} = \delta_{e_0} + G^{-1}(P(\nu_{q_{rm}} - q_0) - \dot{q}_0 + \nu_{\dot{q}_{rm}}) \tag{24}$$

where $\nu_{\dot{q}} = P(\nu_q - q_0)$. Applying this method compensates for the pure time delay in the actuator dynamics, as the oscillatory elevator deflection motion is reduced. Increasing $P_{rm}$ results in a lower settling time during the approach, but eventually reintroduces oscillatory behaviour similar to the case without PCH. The PCH block diagram is shown in Figure 3.

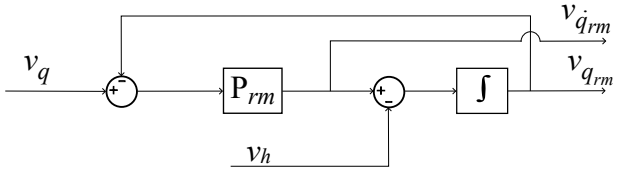


**Fig. 3 PCH block diagram**

### D. Initial Gains Selection

The gains are tuned starting at the inner and hence fastest loop (pitch rate control) and ending with the altitude loop. Some initial gains are chosen while identifying stability regions. Note that the aircraft already has its flaps out and is flying horizontally. To tune the first gain, a step input of 0.05 rad/s is given for the pitch rate loop. Focus is put here on a fast response whilst watching the overshoot. After testing gains in the range of 5-20, it was found that increasing the gain beyond 15 leads to little improvement in rise time but higher overshoot, while gains below 8 respond slowly and only reach 0.05 rad/s after a few seconds. A conservative gain of 12 is chosen, with a rise time of 0.26 s and an overshoot of 15%. After selecting this gain, the pitch angle loop is added and the same procedure is applied, however the elevator deflection is monitored as well. A heavy elevator deflection input is undesirable as this may lead to stability issues later. Gains are tested in the range of 1 - 3. A gain of 2.5 results in an overshoot of 14%, but also heavy elevator activity. The gain can be increased up to 2 before fluctuations in the elevator deflection occur, while $\theta$ slightly undershoots. Therefore, the initial gain is set to 2.

### E. Approach Phase

The goal of the controller is to follow a reference path. The altitude reference is computed separately and passed to the controller. During the approach, the reference path begins at an altitude of 80 m and follows a $-3^\circ$ flight path angle. This path is maintained until reaching an altitude of 40 ft (12.2 m), after which the flare phase begins. A new path is computed using Eq. (25) [14]:

$$h = h_0 - (h_f - h_c)e^{-k_x x} \tag{25}$$

where $h_0$ is the altitude in the previous time step, $h_f$ the altitude at the start of the flare, $h_c$ the convergence altitude for the exponential function and $k_x$ a fixed exponential decay. The reference path converges below the runway, which is situated at 0 m, ensuring that the aircraft lands and does not float just above the runway (so $h_c < 0$). Touchdown dynamics are not simulated in this work, so the simulation is stopped when the runway is reached.

The aircraft is trimmed for a flight path $\gamma = -2^\circ$ at an altitude of 80 m and a velocity of 55 m/s with the flaps fully deployed. The trim angle differs from the actual flight path angle to ensure the controller provides corrective input. Separate gain sets are used for the approach and flare phases in the altitude control loop, as these have different performance requirements. During the approach phase, slower responses are acceptable, whereas during the flare phase a faster and more precise response is more important to satisfy the landing requirements.

Using only a proportional gain during the approach phase results in a steady-state error, where the actual trajectory slightly deviates from the reference path. This error persists until the flare phase begins. To eliminate the steady-state offset, an integrator gain was added to the altitude control loop. While there are some oscillations in the path following, they eventually damp out. To improve the damping and response speed, a derivative gain was added, resulting in a PID controller.

**Table 2 Controller performance metrics**

| Metric | Description | Unit | Requirement |
|---|---|---|---|
| RMSer | RMS error for tracking | m | - |
| RMSur | RMS for control input | rad | - |
| VARur | Variance for control input | $rad^2$ | - |
| $n$ | Max experienced $n$ dev. | - | ±0.2 [15] |
| Sink Rate | Sink rate during touchdown | ft/s | -1 to -10 [16] |
| e | Error relative to the real altitude | m | - |

The approach phase gains were tuned not only for accurate reference path tracking, but also for passenger comfort. Therefore, the control effort, sink rate and load factor were monitored as well, see Table 2 for an overview of the recorded performance metrics. Root Mean Square (RMS) errors are used as relative metrics to compare runs, while quantitative requirements were imposed on the load factor deviation and touchdown sink rate. In addition, a desired sink rate between -1 ft/s and -6 ft/s was selected as a performance target [16].

### F. Flare Phase

The flare phase commences at an altitude of 40 ft, as explained in subsection III.E. Since the flare phase is at a low altitude, high accuracy and effectiveness are of importance, but also landing safety. Since the touchdown velocity is required to be lower than the approach velocity, the thrust input is forced to zero under normal conditions at an altitude of 20 m (65 ft) [15]. In the presence of turbulence, a power-on approach should be used at an airspeed slightly higher than the approach speed, providing more control [17]. Therefore, the velocity control loop is still active under turbulent conditions. Furthermore, the load factor during the entire landing phase and the sink rate at touchdown are factors subject to landing quality requirements. An individual proportional controller cannot accurately land the aircraft. Furthermore, higher proportional gains lead to more aggressive inputs and higher experienced load factors. Due to the desire for a quick response, a derivative gain is added and a small integrator gain for the steady-state error. A similar analysis was performed as explained for the approach phase, where many sets of gains were evaluated based on Table 2. Three of the plots used to evaluate the gains are shown in Figure 4.

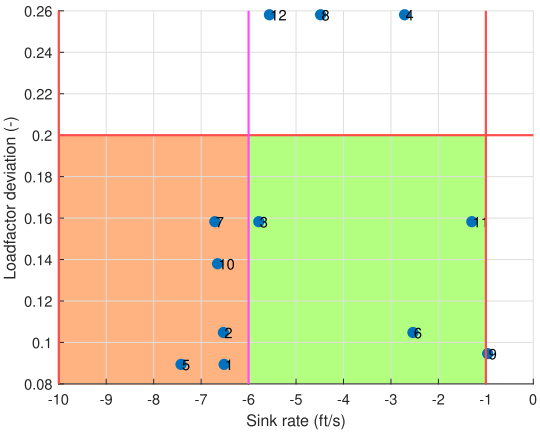


**(a) Load factor versus sink rate**

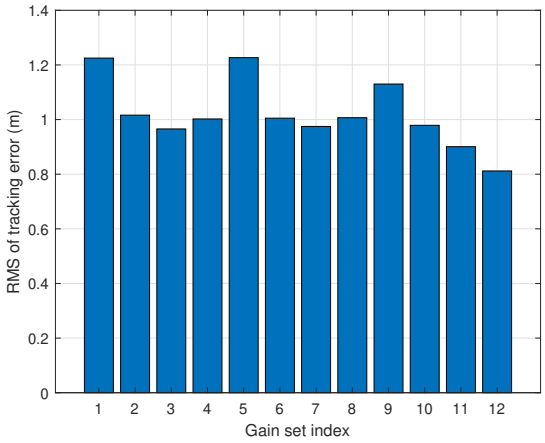


**(b) RMS of tracking error**

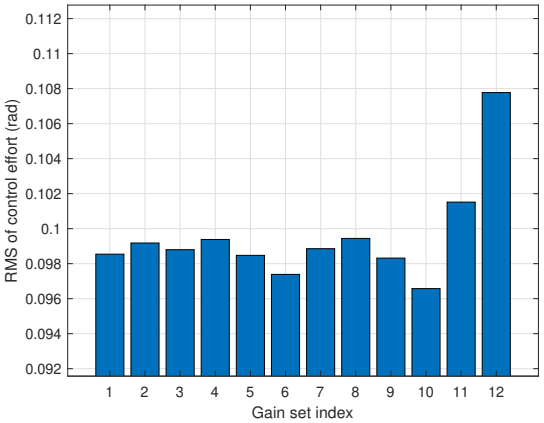


**(c) RMS of control effort**

**Fig. 4 Flare gain tuning procedure**

The gain sets are indicated by numbers. The tested gain sets are grouped as follows:

- Sets 1–4: $K_i = 0.005$, $K_d = 0.01$, varying $K_p = \{0.01, 0.02, 0.03, 0.04\}$.
- Sets 5–8: $K_i = 0.005$, $K_d = 0.005$, varying $K_p = \{0.01, 0.02, 0.03, 0.04\}$.
- Sets 9–12: $K_i = 0.01$, $K_d = 0.005$, varying $K_p = \{0.01, 0.02, 0.03, 0.04\}$.

In Figure 4a, only points within the limits indicated by red are considered, since these lines refer to the requirements. The magenta line denotes the preferred maximum sink rate, with points in the green area being desirable and those in the orange area remaining acceptable but not ideal. This eliminates sets 4, 8 and 12 because they exceed the load factor

deviation requirement. These sets contain $K_p = 0.04$, so the aggressive error punishment leads to higher load factors. Sets 3, 6 and 11 have desired final sink rates. The worst performers focused on tracking are sets 1, 5 and 9. Looking at control effort, these are 4, 8, 11 and 12. This means the final two candidates are sets 3 and 6. Based on the small load factor deviation of set 6, this set is preferred and chosen. The analysis resulted in the set of gains as shown in Table 3. Please note that the first subscript indicates the type of gain (P, I, D) and the second the controlled variable. The approach and flare phases are indicated by subscripts (a and f respectively).

**Table 3 Selected gains for the controller**

| Gains | $K_{Pq}$ | $K_{P\theta}$ | $K_{Pha}$ | $K_{Iha}$ | $K_{Dha}$ | $K_{Phf}$ | $K_{Ihf}$ | $K_{Dhf}$ | $K_{PV}$ |
|---|---|---|---|---|---|---|---|---|---|
| Value | 12 | 2 | 0.02 | 0.005 | 0.01 | 0.02 | 0.005 | 0.005 | 1 |

## IV. Time Delays

Since no signal or disturbance can propagate instantaneously, time delays are an inherent property of all physical systems. By identifying these delays and limiting their impact, performance can be improved.

### A. Problem Description

Delays in sensor measurements may cause stability issues [8]. In simulation environments, these delays are usually constant, whereas in real-life applications they may be variable due to sampling and signal processing, for example during A/C conversion or when loading the signals into the flight computer. This would result in an additional delay of one sample rate.

To replicate this, variable time delays are introduced in the simulations by applying an artificial unit sample delay on a randomised basis. Once a delay is applied, it is held for a minimum number of samples to avoid jitter. This produces intermittent switches between the nominal delay and an additional sample delay, with persistence in each state. While such variability has little impact on most controller components as long as stability is preserved, it is important for accurate signal synchronisation.

**Table 4 Sensor characteristics PH-LAB Cessna Citation [3] [18]**

| Signal | Noise ($\sigma^2$) | Bias | Resolution | Delay (ms) | Sampling Rate (Hz) |
|---|---|---|---|---|---|
| $p, q, r, \dot{\theta}, \dot{\phi}, \dot{\psi}$ [rad/s] | $4.0 \cdot 10^{-7}$ | $3.0 \cdot 10^{-5}$ | $6.8 \cdot 10^{-7}$ | 90 (15) | 52 (1000) |
| $\theta, \phi$ [rad] | $1.0 \cdot 10^{-9}$ | $4.0 \cdot 10^{-3}$ | $9.6 \cdot 10^{-7}$ | 90 | 52 |
| $f_x, f_y, f_z$ [g] | $1.5 \cdot 10^{-5}$ | $2.5 \cdot 10^{-3}$ | $1.2 \cdot 10^{-4}$ | 117 | 52 |
| $V_{TAS}, V_{CAS}$ [m/s] | $8.5 \cdot 10^{-4}$ | 2.5 | $3.2 \cdot 10^{-2}$ | 300 | 16, 8 |
| $h$ [m] | $4.5 \cdot 10^{-3}$ | $8.0 \cdot 10^{-3}$ | $3.0 \cdot 10^{-1}$ | 300 | 16 |
| $\dot{h}$ [m/s] | $5.5 \cdot 10^{-4}$ | $4.5 \cdot 10^{-2}$ | $8.1 \cdot 10^{-2}$ | 300 | 16 |
| $M$ [-] | $1.0 \cdot 10^{-8}$ | $7.0 \cdot 10^{-7}$ | $6.3 \cdot 10^{-5}$ | 300 | 8 |
| $\delta_a, \delta_e, \delta_r$ [rad] | $5.5 \cdot 10^{-7}$ | $2.4 \cdot 10^{-3}$ | - | $\sim 0$ | 100 |
| $\alpha_{\text{boom}}, \beta_{\text{boom}}$ [rad] | $7.5 \cdot 10^{-8}$ | $1.8 \cdot 10^{-3}$ | $9.6 \cdot 10^{-5}$ | 100 | 100 |
| $\alpha_{\text{body}}$ [rad] | $4.0 \cdot 10^{-10}$ | - | $1.0 \cdot 10^{-5}$ | 280 | 1000 |

Sensor characteristics for the PH-LAB were obtained by Grondman et al. following a signal analysis of flight data [3]. More recent research shows different data for the IMU, which indicate a higher sampling rate and lower delay [18]. The results are presented in Table 4, where these new values are added in brackets after the first ones. The largest delay as seen from this table is 300 ms. After the implementation of these time delays, the elevator's behaviour is oscillatory, underscoring the importance of accounting for them in the controller design.

### B. Time Delay Estimator

Synchronisation between the angular acceleration feedback and the elevator deflection improves stability and control performance. This can be achieved by compensating for delays and ensuring filter equivalence. If one signal experiences a larger delay than the other, an artificial delay may be added to the lesser delayed signal to align them. Furthermore, if one signal requires filtering (e.g., for noise reduction), the same filter can be applied to the other to preserve signal consistency and avoid introducing phase mismatches. In this research, frequency response analysis is used to design filters for the measured signals. These filters reduce noise levels, leading to improved performance. The combination of these two methods leads to the following elevator deflection estimate:

$$\hat{\delta} = H_{fil}(s)H_{sync}(s)\delta \tag{26}$$

Since time delays are often unknown and may be variable, a time delay estimator based on cross-correlation is implemented. The goal of the estimator is to determine how much the elevator deflection command leads or lags the aircraft's pitch rate response, enabling improved signal synchronisation. In a steady state, a step input is applied to the elevator, after which $\delta_e$ and $\dot{q}$ are stored. The signals are first detrended by subtracting their mean, which decreases bias effects and ensures the cross-correlation captures relative variations between the signals rather than offsets. An active set based on a threshold is then defined to select only portions of the elevator signal corresponding to actual control inputs, avoiding noisy or idle segments.

The normalised cross-correlation between the detrended signals within the active set is then computed. Normalising makes the correlation dimensionless and bounded between -1 and 1, improving comparability and interpretability. The lag corresponding to the peak of the absolute normalised cross-correlation indicates the best alignment between the two signals and can be used for synchronisation. Mathematically, this procedure can be expressed as:

$$\begin{cases} \text{Detrending:} & \delta_e'[n] = \delta_e[n] - \frac{1}{N}\sum_{i=1}^{N}\delta_e[i], \quad \dot{q}'[n] = \dot{q}[n] - \frac{1}{N}\sum_{i=1}^{N}\dot{q}[i], \\ \text{Active set:} & \mathcal{A} = \{\, n \mid |\delta_e'[n]| > \gamma \,\}, \quad \gamma > 0, \\ \text{Normalised cross-correlation:} & \tilde{R}_{\delta q}[k] = \dfrac{\sum_{n\in\mathcal{A}} \delta_e'[n]\,\dot{q}'[n+k]}{\sqrt{\sum_{n\in\mathcal{A}}(\delta_e'[n])^2}\,\sqrt{\sum_{n\in\mathcal{A}}(\dot{q}'[n+k])^2}}, \\ \text{Delay estimate:} & \hat{k} = \arg\max_k \left|\tilde{R}_{\delta q}[k]\right|, \qquad \hat{\tau} = \hat{k}\,\Delta t. \end{cases} \tag{27}$$

A positive delay estimate ($\hat{\tau} > 0$) indicates that the elevator command leads the pitch rate response, whereas a negative delay ($\hat{\tau} < 0$) indicates a lag. The resulting normalised cross-correlation function and the synchronisation resulst are shown in Figure 5.

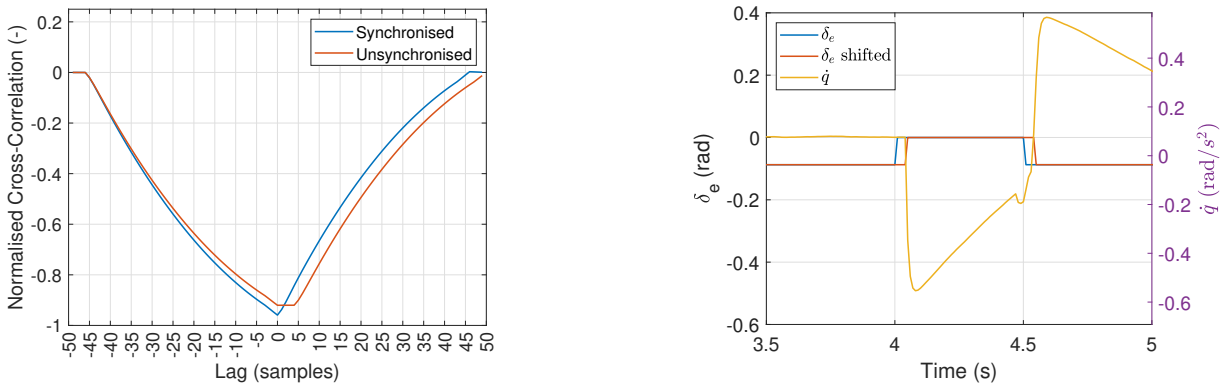


**(a) Estimator normalised cross-correlation** **(b) $\delta_e$ synchronised with $\dot{q}$**

**Fig. 5 Time delay estimator performance**

The results of the time delay estimation demonstrate the effectiveness of the synchronisation method. Figure 5a shows the cross-correlation curves. The unsynchronised signal, represented by the orange line, exhibits a noticeable delay, with the minimum normalised cross-correlation value occurring at a lag of approximately 4 samples. This indicates that $\dot{q}$ lags behind $\delta_e$. After synchronisation with the estimated delay, the minimum of the cross-correlation curve shifts to a lag of zero, indicating that the procedure was successful. The alignment is further verified in the time

domain, as shown in Figure 5b, where the signals visually align after synchronisation. These results demonstrate the accuracy of the estimator and the resultant shift experienced by the control system.

### C. IMU-based Altitude Method

The relatively high DADC time delay of 300 ms results in reduced performance, as it is used for the feedback in the altitude loop. When decreasing the outer loop time delay from the DADC delay to the AHRS delay, it is found that the maximum experienced load factor reduces to acceptable levels, the RMS of tracking effort halves and it is close to the undelayed scenario. This led to the design of an alternative altitude estimate.

Linear acceleration measurements from the accelerometer can be used to calculate the altitude, while subject to a lower delay of 117 ms and lower bias and noise characteristics than the DADC altitude measurement (see Table 4). The gravitational component must be removed from the accelerometer measurement to isolate the true linear acceleration of the aircraft. Moreover, as the measurements are in the body frame, they have to be transformed to the inertial frame. The coordinate transformation is done by the Direction Cosine Matrix (DCM). The rotation is performed in ZYX order, a rotation about the Z axis (yaw), then about the y axis (pitch), and finally about the x axis (roll), as shown in Eq. (28). Thereafter, the altitude can be computed by double integration of the transformed vertical acceleration. The Euler angle signals and angular rate signals are synchronised in time using the time delay estimator.

$$
\begin{aligned}
\mathrm{DCM} &= R_z(\psi)R_y(\theta)R_x(\phi) \\
&= \begin{bmatrix} \cos\psi & \sin\psi & 0 \\ -\sin\psi & \cos\psi & 0 \\ 0 & 0 & 1 \end{bmatrix} \begin{bmatrix} \cos\theta & 0 & -\sin\theta \\ 0 & 1 & 0 \\ \sin\theta & 0 & \cos\theta \end{bmatrix} \begin{bmatrix} 1 & 0 & 0 \\ 0 & \cos\phi & \sin\phi \\ 0 & -\sin\phi & \cos\phi \end{bmatrix} \\
&= \begin{bmatrix} \cos\theta\cos\psi & \cos\theta\sin\psi & -\sin\theta \\ \sin\phi\sin\theta\cos\psi - \cos\phi\sin\psi & \sin\phi\sin\theta\sin\psi + \cos\phi\cos\psi & \sin\phi\cos\theta \\ \cos\phi\sin\theta\cos\psi + \sin\phi\sin\psi & \cos\phi\sin\theta\sin\psi - \sin\phi\cos\psi & \cos\phi\cos\theta \end{bmatrix}
\end{aligned}
\tag{28}
$$

The double integration of the accelerometer signal is inherently susceptible to cumulative errors, as each integration step builds upon the previous one. Furthermore, small deviations in the initialisation of the rotation matrix or accelerometer measurements can propagate, leading to inaccurate altitude estimates. To mitigate this effect, careful initialisation of the relevant states is essential, and periodic corrections of the altitude estimate during flight are required.

### D. Kalman Filter

As explained above, the IMU based altitude computation is prone to errors. Therefore, sensor fusion can serve as a correction factor. By combining the DADC measurement and IMU-based computation with a Kalman filter, reliability increases. The core of a Kalman filter is its state vector, which represents the variable one desires to estimate. In this application, the state vector consists of the estimated vertical position $\hat{h}$, the estimated vertical speed $\hat{\dot{h}}$ and an estimate for the IMU bias $\hat{b}_a$:

$$x_k = \begin{bmatrix} \hat{h} & \hat{\dot{h}} & \hat{b}_a \end{bmatrix}^T$$

The state vector and correction matrix $P$ must be initialised. The altitude estimate is initialised using the trim altitude, and the vertical speed estimate is also initialised from the trim state. The IMU bias estimate is initialised at 0. $P_0$ is set as a 3x3 identity matrix to improve robustness for situations where its initial content is unknown. $P$ converges within three seconds, which is within the configuration phase.

Next is the prediction step, involving some new matrices which are defined below:

$$F_k = \begin{bmatrix} 1 & \Delta t & 0 \\ 0 & 1 & 0 \\ 0 & 0 & 1 \end{bmatrix} \quad B_k = \begin{bmatrix} \frac{1}{2}\Delta t^2 \\ \Delta t \\ 0 \end{bmatrix} \quad H_k = \begin{bmatrix} 1 & 0 & 0 \end{bmatrix}$$

with $F_k$ the state transition matrix, $B_k$ the control input matrix, $H_k$ the measurement matrix. The control input $u_k$ is computed by correcting the IMU acceleration with the bias estimate $\hat{b}_a$. Using these matrices, the prediction step follows:

$$
\begin{aligned}
x_k &= F_k x_{k-1} + B_k u_k \\
P_k &= F_k P_{k-1} F_k^T + Q_k
\end{aligned}
\tag{29}
$$

Using this prediction, the update step can be performed:

$$
\begin{aligned}
y_k &= h_s - H_k x_k \\
S_k &= H_k P_k H_k^T + R_k \\
K_k &= P_k H_k^T / S_k \\
x_k &= x_k + K_k y_k \\
P_k &= (I - K_k H_k) P_k
\end{aligned}
\tag{30}
$$

with $R_k$ the measurement noise covariance matrix, $Q_k$ the process noise covariance matrix, $y_k$ the innovation step, $S_k$ the innovation covariance and $K_k$ the Kalman gain. The state matrix's altitude can then be used for the altitude feedback. $Q_k$ and $R_k$ show the confidence in each respective signal. By tuning these, more emphasis can be placed on the computed altitude or the fed-back DADC altitude. The selected options are $Q_k = \text{diag}([1e-5, 1e-4, 1e-7])$, $R_k = 10$ based on performance metrics similar to those used to tune the gains. With this configuration, the Kalman filter primarily relies on the fast, dynamic updates from the IMU, while the slower DADC measurements are used to periodically correct for drift in the IMU-based estimate. The final controller structure can be observed in Figure 6, where the block "h est" contains the IMU-based altitude estimation and the Kalman filter.

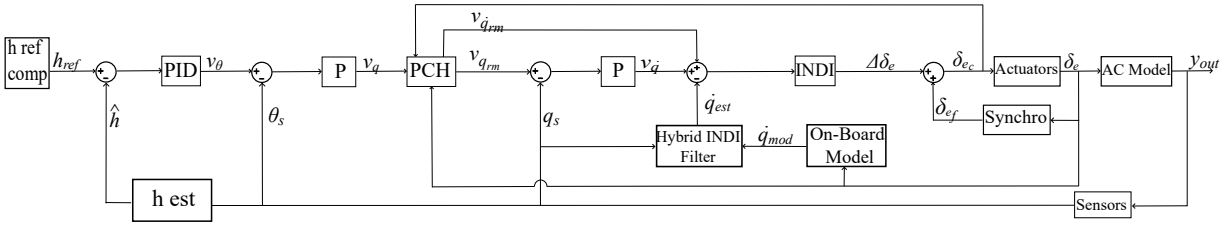


**Fig. 6 Altitude controller structure**

## V. Results

This section presents the performance evaluation of the controller in a simulated autoland scenario. First, the overall performance is assessed under calm and turbulent conditions, highlighting tracking accuracy, control effort, and disturbance rejection properties in several scenarios. Sensitivity analyses then examine how variations in aircraft and turbulence characteristics affect the controller's performance.

### A. Overall Performance

The path following performance of the controller was evaluated under moderate turbulence generated using the Dryden Turbulence Wind Model. The corresponding results are shown in Figure 7. As illustrated in Figures 7a and 7b, the Kalman filter maintains the altitude error with respect to the reference trajectory within approximately 2 m. The largest deviations occur around 12 seconds and during touchdown. When assessing the actual altitude, a drift from the reference is observed between 6 s and 11 s, after which the aircraft recovers to the desired path. A final drift starting around 24 seconds leads to a final altitude error of about 2.4 m.

Furthermore, Figure 7b highlights the necessity of the Kalman filter. While the IMU-based altitude estimate ("Estimate") accurately computes the altitude at first, it begins to drift as the actual altitude varies more significantly, starting around 16 seconds into the simulation. At touchdown, the IMU-based estimate deviates by approximately 1.6 m from the actual altitude and by roughly 4 m from the reference. This demonstrates that fusing the short-term accurate but drifting IMU estimate with the long-term stable DADC measurement through the Kalman filter improves the overall altitude estimation and trajectory tracking performance.

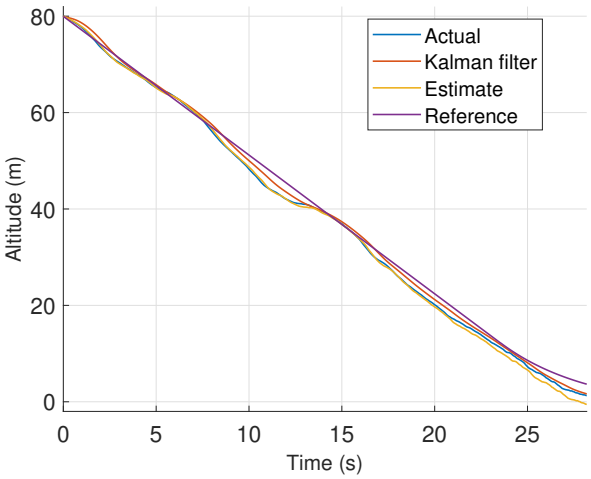


**(a) Altitudes from varying sensors/calculations**

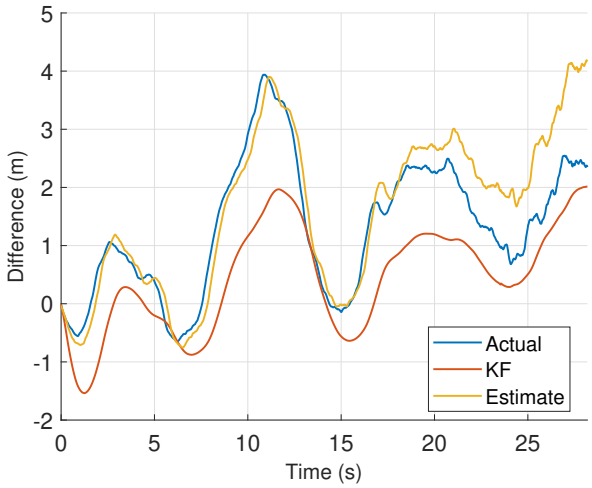


**(b) Error with respect to the reference altitude**

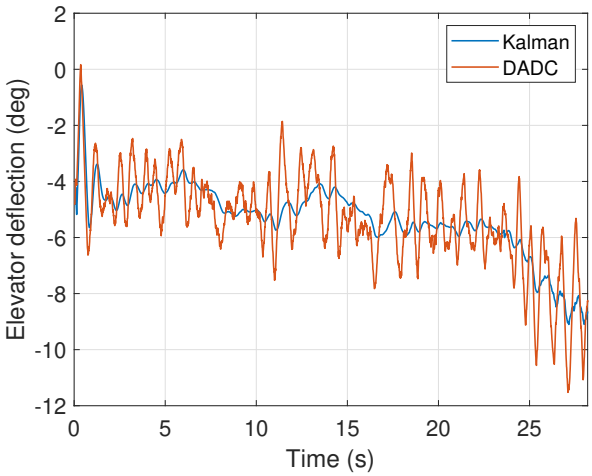


**(c) Elevator deflection when using Kalman filter or DADC measurement**

**Fig. 7 Performance plots**

The improved altitude estimation translates into smoother control actions. As shown in Figure 7c, reliance on the DADC measurement alone results in oscillatory elevator deflections under turbulent conditions. Incorporating the Kalman filter damps these oscillations and reduces the amplitude of elevator inputs. This not only decreases load factor deviations and therefore improves passenger comfort, but also lowers the risk of elevator saturation. Under stronger turbulence, the DADC-only case occasionally drives the elevator close to its physical limits, whereas the Kalman filter keeps control inputs within safe margins, making it the safer and more robust alternative.

To further evaluate the controller's performance, multiple scenarios were tested and compared using performance metrics. The performance of each scenario is summarised in Table 5. Please note that $RMSer_{act} = RMS(h_{ref} - h)$ and $RMSer_{con} = RMS(h_{ref} - h_{KF})$, and the remainder of the metrics are explained in Table 2. The final three metrics correspond to the maximum deviation between the Kalman filter estimate and the actual altitude, evaluated during the approach, the flare, and at the final time step, respectively.

The no turbulence scenario provides a baseline for controller performance, with the lowest RMS tracking and control values, demonstrating the controller's capability under nominal, disturbance-free conditions. The default scenario with moderate turbulence serves as a reference for assessing the effects of disturbances. While RMS tracking and control effort increase relative to the no-turbulence case, performance is still satisfactory. The maximum load factor deviation is

actually smaller than the no turbulence case, confirming the controller's disturbance rejection property.

Three additional setups were investigated to examine the effects of trim initialisation and model uncertainties.

1) The aircraft is trimmed with $\gamma = 0°$.
2) The aircraft is trimmed at an altitude of 82 m, while the reference path starts at 80 m.
3) The control effectiveness matrix contains an error of 60%.

A few remarks can be made. First, altering the trim initialisation does not have a clear effect on the reference tracking, with a similar RMSer$_{con}$. Because of the initial alignment with the -3° reference path, the maximum load factor deviation is slightly exceeded. The Kalman filter accuracy is reduced slightly during the flare, but the overall performance remains adequate, although the final sink rate is outside the desirable range.

An offset between the initial altitude and the reference path has little effect on overall performance. Similar to Setup 1, the initial alignment results in an increased load factor. Still, all metrics remain comparable to the default scenario, demonstrating that the controller easily adjusts to the reference path. The control effort is slightly lower, and the RMSer$_{act}$ as well. The latter is unexpected given the larger maximum errors, which highlights that RMSer$_{act}$ is partly sensitive to chance. Unlike RMSer$_{con}$, which directly measures tracking performance, RMSer$_{act}$ reflects the combined effect of the estimation error and tracking error. As a result, it can occasionally appear smaller when the two errors partially cancel each other, even though the underlying deviations are larger.

Third, an error of 60% in the control effectiveness matrix used for the inversion process, PCH, and the hybrid filter, produces results very similar to the default case. The variance in control effort increases by $\approx$ 10%, but the other performance metrics remain almost unchanged, confirming the robustness of INDI to modelling inaccuracies.

Overall, these results demonstrate that while an initial offset in altitude or flight path angle can influence short-term tracking performance, the controller maintains performance under both trim variations and modelling errors. This confirms the practical reliability of the INDI approach in handling uncertainties typical of autoland scenarios.

**Table 5 Effects of trim and model uncertainty**

| **Setup** | **RMSer$_{act}$** (m) | **RMSer$_{con}$** (m) | **RMSur** (rad) | **Varur** (rad$^2$) | $n$ (-) | **Sink** (ft/s) | **e$_{app}$** (m) | **e$_{fl}$** (m) | **e$_{fin}$** (m) |
|---|---|---|---|---|---|---|---|---|---|
| No turb | 1.17 | 0.66 | 8.79e-02 | 9.30e-04 | 1.14 | -1.67 | -1.54 | -0.92 | -0.23 |
| Default | 1.75 | 1.00 | 9.74e-02 | 4.45e-04 | 0.90 | -2.54 | -2.36 | -0.95 | -0.33 |
| Setup 1 | 1.56 | 1.33 | 8.98e-02 | 1.76e-04 | 0.79 | -7.14 | -2.38 | -1.07 | -0.33 |
| Setup 2 | 1.61 | 1.17 | 9.50e-02 | 2.77e-04 | 1.22 | -6.55 | -2.52 | -1.12 | 0.14 |
| Setup 3 | 1.75 | 0.99 | 9.79e-02 | 4.98e-04 | 1.12 | -1.96 | -2.35 | -0.94 | -0.24 |

### B. Sensitivity Analyses

Sensitivity analyses are conducted to evaluate the influence of design parameters and aircraft characteristics on the controller's performance. The common performance metrics are the RMS of tracking error, the load factor deviation and the RMS of control effort, although other metrics may also be considered. The first parameter examined is the IMU transport delay, which is varied from the baseline value of 0.12 s up to 0.80 s, as illustrated in Figures 8a-8c. The same randomised procedure for generating variable time delays as described in subsection IV.A is applied.

The analysis shows that the performance degrades as the IMU delay increases. The RMS tracking error grows gradually and then more rapidly from about 1.3 m to 1.5 m, while load-factor deviations begin to increase notably after the delay exceeds 400 ms (Figures 8a-8b), but remain within the requirement up to a delay of $\approx$ 0.75 seconds. Moreover, the analysis shows that the control effort increases rapidly, with a peak about 20% above its original value. This initial growth is consistent with expectations, since larger delays deteriorate tracking performance and require more aggressive elevator inputs.

The subsequent decrease in control effort observed in Figure 8c is less intuitive, as one would anticipate a continued increase with growing delay. Closer inspection of individual simulations revealed that this peak arises when the controller attempts to correct a residual error near touchdown. With limited delay, the feedback remains sufficiently fast for the controller to apply a final elevator input just before ground contact, thereby increasing the RMS of elevator deflection. When the delay is further increased, the feedback becomes too slow for the controller to respond in time, and the final corrective input is not commanded. As a result, the RMS of control effort decreases again and subsequently stabilises.

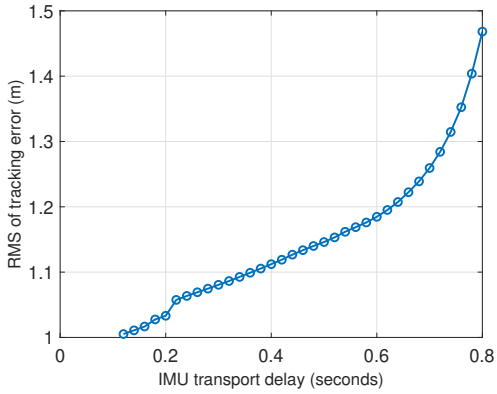


**(a) Tracking RMS vs IMU delay**

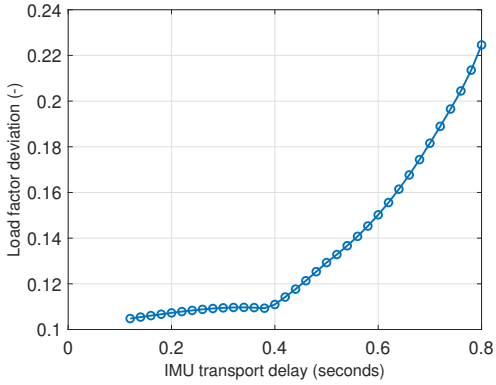


**(b) Load factor deviation vs IMU delay**

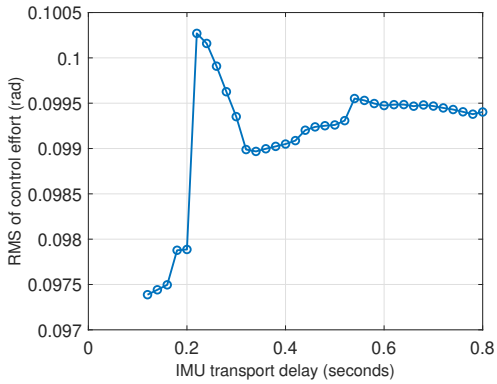


**(c) Control effort RMS vs IMU delay**

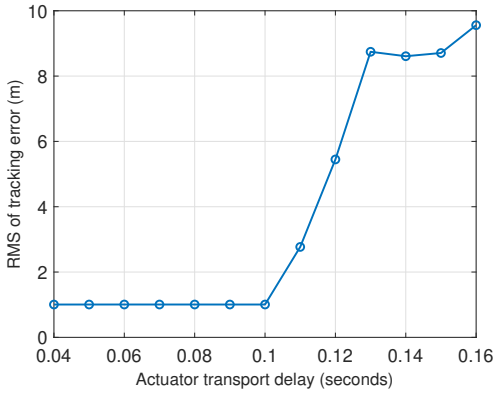


**(d) Tracking RMS vs actuator delay**

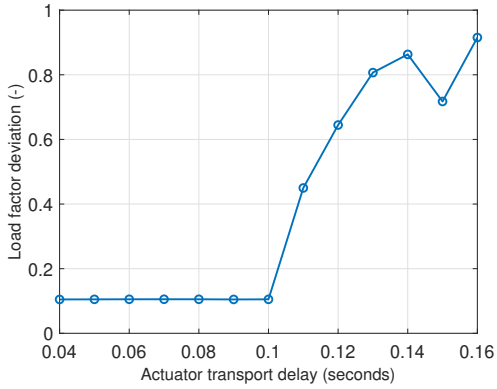


**(e) Load factor deviation vs actuator delay**

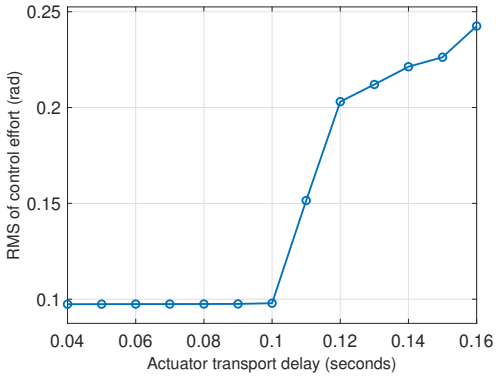


**(f) Control effort RMS vs actuator delay**

**Fig. 8 Effect of actuator delay on system performance metrics**

Taken together, these findings show that the controller can tolerate moderate IMU delays without violating performance criteria, but exhibits a peak in control effort at moderate delays due to late corrective inputs near touchdown, followed by a regime where excessive delays suppress such corrections. The performance degradation becomes critical when delays approach the order of 0.75 seconds, such that the time delay margin is 0.63 seconds.

The second parameter to be examined is the actuator transport delay. This delay is varied from the baseline value of 0.04 seconds up to 0.16 seconds and the results are shown in Figures 8d-8f. All performance metrics experience significant degradation when increasing this delay beyond 100 ms. The control effort approximately doubles, leading to exceedingly large load factor deviation and decreased tracking performance. This analysis suggests that the actuator

time delay margin is about 60 ms from the regular value.

Next, the sensitivity to turbulence is tested. By increasing the turbulence speed at an altitude of 20 ft in the Dryden Turbulence model, the disturbances are amplified. Speeds in the range of 10-30 m/s are tested, and the maximum load factor deviations and final sink rates are shown in Figure 9. These values represent the range from light/moderate turbulence up to severe levels [19]. From a turbulence speed of 21 m/s the maximum load factor deviation limit is reached. The final sink rate is more susceptible to sudden wind gusts and consequently is slightly too low at times. The tracking error increases linearly as expected, as the aircraft is forced away from the reference path. The control effort increases accordingly as the aircraft is navigated back. Since 21 m/s at 6 ft altitude is relatively high for turbulence and the aircraft effectively combats the disturbances, the controller is relatively unsensitive to turbulence.

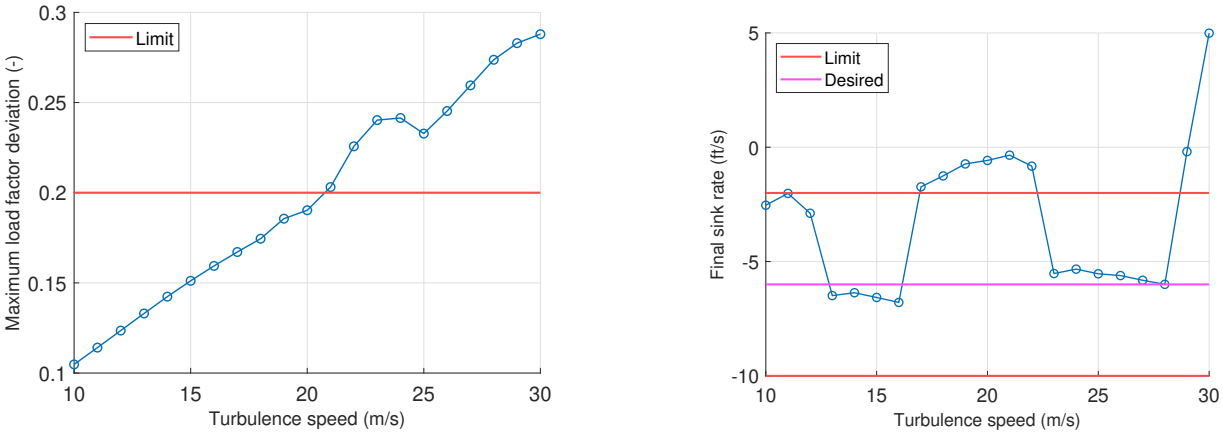


**(a) Maximum load factor deviation vs turbulence speed**

**(b) Final sink rate relative vs turbulence speed**

**Fig. 9 Requirement plots for different turbulence speeds**

For all simulations, a specific randomisation seed was taken. To evaluate the controller's sensitivity to different turbulence realisations, the seed was varied over 100 samples while collecting performance metrics. Green areas represent regions that satisfy the requirements, and the orange region depicts an area where the sink rate is not desirable, but within the required limits. Figure 10a shows that the majority of the seeds meet these requirements, as most of the points lie within the red boundary lines and within the green area. The points outside this region can be attributed to inconvenient regions of turbulence, i.e. a wind gust that increases a load factor induced by manoeuvring. When analysing figures 10b-10f, it becomes evident that higher final altitude errors, higher load factor deviations and worse tracking accompany the sink rates exceeding the limits. The closer the aircraft lands to the designated landing spot (around 1500 m horizontally from the starting point), the smaller the final altitude error becomes. Please note that this error is defined as $e = h - h_{ref}$. Control effort is relatively constant over all simulations, while the tracking is somewhat randomly distributed for the different seeds. The statistical variation of the evaluated performance metrics under different turbulence seeds is presented in Table 6.

**Table 6 Turbulence seed variance statistics**

| Metric | Mean | Std | Var |
|---|---|---|---|
| LF deviation (-) | 0.171 | 4.14e-02 | 1.70e-03 |
| Final sink rate (ft/s) | -5.86 | 3.69 | 13.64 |
| Final altitude error (m) | 2.10 | 1.49 | 2.21 |
| RMS of control effort (rad) | 2.13e-02 | 3.5e-03 | 1.21e-05 |
| RMS of tracking error (m) | 1.29 | 0.315 | 9.92e-02 |

The mean final sink rate is -5.86 ft/s, which lies within the admissible range of [-1,-10] ft/s and also the desired range of [-1,-6] ft/s. The relatively large standard deviation and variance also observed in Figure 10b indicate that some realisations deviate from these bounds, even though most remain within limits. The maximum load factor deviation

shows a mean of 0.171, below the limit of 0.2, and the majority of cases remain within the limits. Altogether, the plots and statistics demonstrate that the controller is robust to seed variation. The majority of cases satisfy the requirements, with deviations limited to a few edge cases.

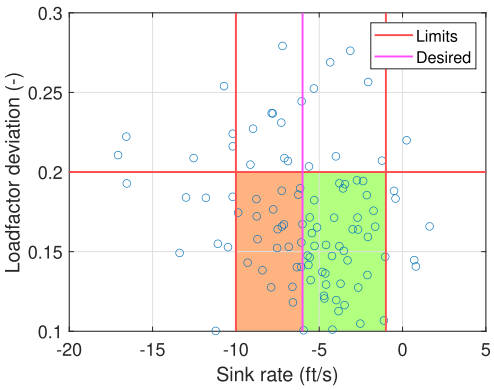


**(a) Maximum load factor deviation vs sink rate**

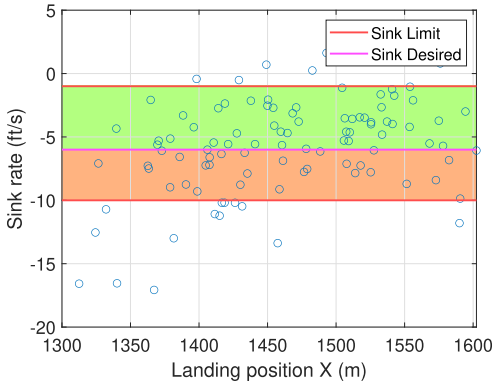


**(b) Maximum load factor deviation relative to landing spot**

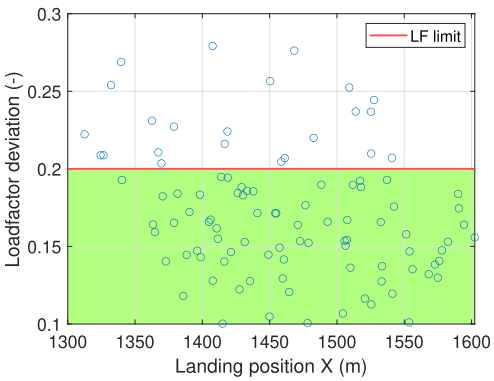


**(c) Sink rate relative to landing spot**

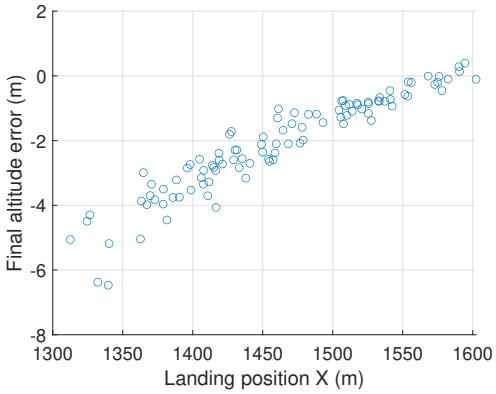


**(d) Final altitude error relative to landing spot**

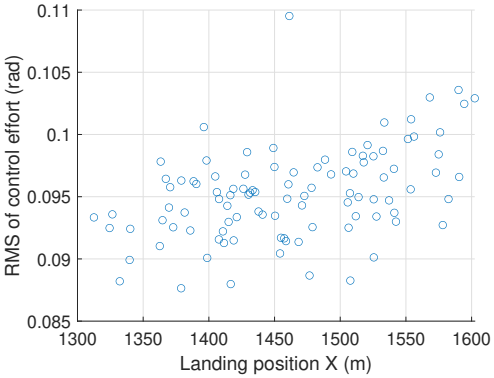


**(e) Control effort relative to landing spot**

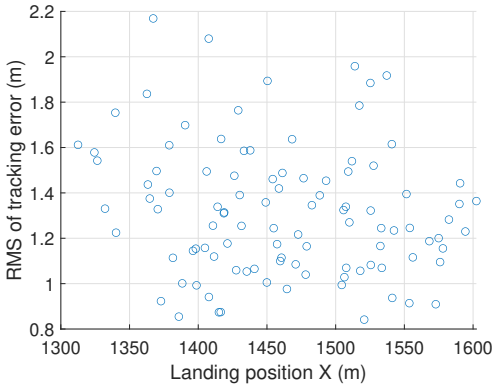


**(f) Tracking error relative to landing spot**

**Fig. 10 Performance metrics comparison for different turbulence seeds**

## VI. Conclusion

Incremental Nonlinear Dynamic Inversion (INDI) control can be applied to the autoland of the PH-LAB Cessna Citation aircraft in a simulated environment. The proposed framework addresses key limitations of the autoland application, particularly those arising from sensor and actuator delays, while maintaining stability and overall performance under turbulent conditions.

A novel altitude estimator based on IMU linear accelerations, fused with the long-term stable Digital Air Data Computer (DADC) altitude through a Kalman filter, effectively reduces sensor delay while avoiding cumulative integration errors that would otherwise compromise the accuracy of the estimate. Combined with Pseudo-Control Hedging (PCH) to mitigate actuator delays, the controller reduces elevator oscillations and improves passenger comfort. The hybrid filter design eliminates reliance on angular accelerometers, which are not standard equipment on the aircraft, thereby enhancing the practical applicability.

The controller meets the specified landing comfort requirements and demonstrates resilience to turbulence and variable delays. Sensitivity analyses confirm that performance margins are finite but sufficient for operational scenarios, with occasional deviations attributable to stochastic effects rather than systematic shortcomings. These findings indicate that the proposed Hybrid INDI framework provides a reliable solution that consistently meets performance requirements in the autoland application.

While the results are promising, the current model has several limitations that represent important areas for future research. The simulation does not yet account for the dynamics of ground effect or the physical interactions during touchdown. To validate the controller for real-world applications, future work should integrate a ground effect model into the simulation environment. In addition, enhancing the altitude estimation by incorporating radar altimeter measurements into the IMU-DADC fusion could further improve reliability and accuracy. Furthermore, the current design focuses on longitudinal control. Extending the control design to include lateral and directional axes would enable the aircraft to handle crosswind landings and more complex flight paths.

Despite these areas of future research, the proposed framework demonstrates potential for practical autoland applications. Its ability to handle sensor and actuator delays while maintaining smooth and accurate altitude control provides a solid foundation for further development. With the integration of additional aircraft dynamics and full-axis control, this framework can serve as a basis for real-world autoland operations.

## References


[1] Steinert, A., Raab, S., Hafner, S., Holzapfel, F., and Hong, H., "From fundamentals to applications of incremental nonlinear dynamic inversion: A survey on INDI – Part I," *Chinese Journal of Aeronautics*, 2025, p. 103553. https://doi.org/10.1016/j.cja.2025.103553.

[2] Stam, N., and de Visser, C. C., "Adaptive Dynamic Incremental Nonlinear Control Allocation for Aircraft With Innovative Control Effectors," *AIAA SCITECH 2025 Forum*, American Institute of Aeronautics and Astronautics, 2025. https://doi.org/10.2514/6.2025-0082.

[3] Grondman, F., Looye, G., Kuchar, R. O., Chu, Q. P., and Van Kampen, E.-J., "Design and Flight Testing of Incremental Nonlinear Dynamic Inversion-based Control Laws for a Passenger Aircraft," *2018 AIAA Guidance, Navigation, and Control Conference*, AIAA SciTech Forum, American Institute of Aeronautics and Astronautics, 2018. https://doi.org/10.2514/6.2018-0385.

[4] Steinleitner, A., Frenzel, V., Pfeifle, O., Denzel, J., and Fichter, W., "Automatic Take-Off and Landing of Tailwheel Aircraft with Incremental Nonlinear Dynamic Inversion," *AIAA SCITECH 2022 Forum*, American Institute of Aeronautics and Astronautics, 2022. https://doi.org/10.2514/6.2022-1228.

[5] Huang, Y., Zhang, Y., Pool, D. M., Stroosma, O., and Chu, Q., "Time-Delay Margin and Robustness of Incremental Nonlinear Dynamic Inversion Control," *Journal of Guidance, Control, and Dynamics*, Vol. 45, No. 2, 2022, pp. 394–404. https://doi.org/10.2514/1.G006024.

[6] Wang, X., van Kampen, E.-J., Chu, Q., and Lu, P., "Stability Analysis for Incremental Nonlinear Dynamic Inversion Control," *Journal of Guidance, Control, and Dynamics*, Vol. 42, No. 5, 2019, pp. 1116–1129. https://doi.org/10.2514/1.G003791, publisher: American Institute of Aeronautics and Astronautics.

[7] Zhang, S., Zhang, H., and Ji, K., "Incremental Nonlinear Dynamic Inversion Attitude Control for Helicopter with Actuator Delay and Saturation," *Multidisciplinary Digital Publishing Institute*, Vol. 10, No. 6, 2023, p. 521. https://doi.org/10.3390/aerospace10060521.

[8] van 't Veld, R. C., "Incremental Nonlinear Dynamic Inversion Flight Control," Ph.D. thesis, Delft University of Technology, 2016. URL https://repository.tudelft.nl/record/uuid:f85a9c88-7bdb-42cd-a01c-aa85251d365c.

[9] Sieberling, S., Chu, Q. P., and Mulder, J. A., "Robust Flight Control Using Incremental Nonlinear Dynamic Inversion and Angular Acceleration Prediction," *Journal of Guidance, Control, and Dynamics*, Vol. 33, No. 6, 2010, pp. 1732–1742. https://doi.org/10.2514/1.49978.

[10] Kumtepe, Y., Pollack, T. S. C., and van Kampen, E. J., "Flight Control Law Design using Hybrid Incremental Nonlinear Dynamic Inversion," *AIAA SciTech Forum*, 2022. https://doi.org/10.2514/6.2022-1597.

[11] Salahudden, S., Agrawal, H., Karnam, A., and Roy, A., "Decoupled incremental nonlinear dynamic inversion control for aircraft autonomous landing with ground-effect," *Aerospace Science and Technology*, Vol. 149, 2024, p. 109156. https://doi.org/10.1016/j.ast.2024.109156.

[12] Smeur, E. J. J., Höppener, D. C., and Wagter, C., "Prioritized Control Allocation for Quadrotors Subject to Saturation," 2017. URL https://repository.tudelft.nl/record/uuid:54c4659a-3a6d-4d44-873d-aec6ae5e2376.

[13] Johnson, E., and Calise, A., "Pseudo-Control Hedging: A New Method For Adaptive Control," Tech. rep., Georgia Institute of Technology, Atlanta, Sep. 2001.

[14] Singh, S., and Padhi, R., "Automatic path planning and control design for autonomous landing of UAVs using dynamic inversion," *2009 American Control Conference*, 2009, pp. 2409–2414. https://doi.org/10.1109/ACC.2009.5160444, iSSN: 2378-5861.

[15] Roskam, J., and Edward Lan, C.-T., *Airplane Aerodynamics And Performance*, DARcorporation, 1997.

[16] Siegel, D., and Hansman, R. J., "Development of an Autoland System for General Aviation Aircraft," 2011. URL https://dspace.mit.edu/handle/1721.1/66604, accepted: 2011-10-27T18:46:36Z.

[17] Administration, F. A., "Short Field Approach and Landing," FAASTeam Document SO15131753, FAA Safety Team, 2024. URL https://www.faasafety.gov/files/events/SO/SO15/2024/SO15131753/ShortFieldApproachLanding_afh_ch9.pdf.

[18] Konatala, R. B., Van Kampen, E.-J., Looye, G., Milz, D., and Weiser, C., "Flight Testing Reinforcement Learning based Online Adaptive Flight Control Laws on CS-25 Class Aircraft," *AIAA SCITECH 2024 Forum*, American Institute of Aeronautics and Astronautics, Orlando, FL, 2024. https://doi.org/10.2514/6.2024-2402.

[19] Moorhouse, D. J., and Woodcock, R. J., "Background Information and User Guide for MIL-F-8785C, Military Specification - Flying Qualities of Piloted Airplanes," Tech. Rep. AFWAL-TR-81-3109, Flight Dynamics Laboratory, Control Dynamics Branch, Sep. 1981.

# Part II

## Literature Review

# 3

# Incremental Nonlinear Dynamic Inversion (INDI)

INDI builds on NDI to enable incremental control updates using sensor feedback. NDI provides the foundation by linearising the system dynamics via inversion, while INDI reduces the dependency on accurate models and compensates unmodelled effects through measured system responses. The following sections present the basic derivation of NDI, INDI, and novel approaches.

## 3.1. Basic Derivation NDI

This subsection provides the basic derivation of NDI, which serves as the foundation for understanding the INDI technique discussed in the next section. NDI is a control strategy designed to linearise nonlinear systems by inverting the nonlinear dynamics and establishing a direct relationship between the control inputs and the system outputs. It is typically applied to control-affine systems, where the control input $\boldsymbol{u}$ enters the system dynamics in a linear fashion. An NDI system assumes that the system model is accurately known, and complete and accurate knowledge of system state feedback is available. While NDI offers promising results in terms of system performance, it is sensitive to uncertainties, external disturbances, and model inaccuracies

Consider a general control-affine nonlinear system represented in state-space form as [4]:

$$\begin{aligned} \dot{x} &= f(x) + g(x)u \\ y &= h(x) \end{aligned} \tag{3.1}$$

where $x \in \mathbb{R}^n$ is the state vector, $u \in \mathbb{R}^m$ the input vector, $y \in \mathbb{R}^d$ the output vector, $f \in \mathbb{R}^{n\times 1}$ the body and thrust model matrix (state dynamics), $g \in \mathbb{R}^{n\times m}$ the control effectiveness matrix and $h \in \mathbb{R}^{d\times 1}$ a function to obtain the output vector. If $g(x)$ is invertible, Eq. (3.1) can be rewritten for $u$ as:

$$\boldsymbol{u} = \boldsymbol{g}(x)^{-1}(\boldsymbol{v} - \boldsymbol{f}(x)) \tag{3.2}$$

The virtual control input $\boldsymbol{v}$ is the input used within the linearisation loop, and defined as $\boldsymbol{v} = \dot{\boldsymbol{x}}$, such that it represents the desired system response. The virtual control input is determined by the linear controllers, which are designed based on the desired dynamics of the control variables. For instance, a Proportional-Integral-Differential (PID) controller can be used to shape these dynamics [11].

## 3.2. Basic Derivation INDI

For general nonlinear, nonaffine system dynamics, the concept of INDI will be explained here [12]. The state vector and output vector are defined as follows:

$$\dot{\boldsymbol{x}} = \boldsymbol{f}(\boldsymbol{x}(t), \boldsymbol{u}(t)) \tag{3.3}$$

$$\boldsymbol{y} = \boldsymbol{h}(\boldsymbol{x}(t)) \tag{3.4}$$

with state vector $\boldsymbol{x}(t) \in \mathbb{R}^n$, output vector $\boldsymbol{y}(t) \in \mathbb{R}^r$, and input vector $\boldsymbol{u}(t) \in \mathbb{R}^m$. When applying a first-order Taylor series expansion to the system dynamics around an operating point $(\boldsymbol{x}_0, \boldsymbol{u}_0)$, one obtains:

$$\dot{\boldsymbol{x}} = \underbrace{\boldsymbol{f}(\boldsymbol{x}_0, \boldsymbol{u}_0)}_{\dot{\boldsymbol{x}}_0} + \frac{\partial \boldsymbol{f}}{\partial \boldsymbol{x}}\Big|_{\boldsymbol{x}_0,\boldsymbol{u}_0} (\boldsymbol{x} - \boldsymbol{x}_0) + \frac{\partial \boldsymbol{f}}{\partial \boldsymbol{u}}\Big|_{\boldsymbol{x}_0,\boldsymbol{u}_0} (\boldsymbol{u} - \boldsymbol{u}_0) + \mathcal{O}\big((\boldsymbol{x} - \boldsymbol{x}_0)^2, (\boldsymbol{u} - \boldsymbol{u}_0)^2\big) \tag{3.5}$$

The higher-order terms $\mathcal{O}(\Delta \boldsymbol{x}^2, \Delta \boldsymbol{u}^2)$ are neglected, producing a locally linear incremental model that preserves the first-order sensitivity of the system to both state and actuator deviations. Differentiating the remainder of Eq. (3.4) with the chain rule and subsequently substituting Eq. (3.5) yields:

$$\begin{aligned} \dot{\boldsymbol{y}} &= \frac{\partial \boldsymbol{h}}{\partial \boldsymbol{x}}\Big|_{\boldsymbol{x}_0} \dot{\boldsymbol{x}} \\ \dot{\boldsymbol{y}} &= \frac{\partial \boldsymbol{h}}{\partial \boldsymbol{x}}\Big|_{\boldsymbol{x}_0} \dot{\boldsymbol{x}}_0 + \frac{\partial \boldsymbol{h}}{\partial \boldsymbol{x}}\Big|_{\boldsymbol{x}_0} \frac{\partial \boldsymbol{f}}{\partial \boldsymbol{x}}\Big|_{\boldsymbol{x}_0,\boldsymbol{u}_0} (\boldsymbol{x} - \boldsymbol{x}_0) + \frac{\partial \boldsymbol{h}}{\partial \boldsymbol{x}}\Big|_{\boldsymbol{x}_0} \frac{\partial \boldsymbol{f}}{\partial \boldsymbol{u}}\Big|_{\boldsymbol{x}_0,\boldsymbol{u}_0} (\boldsymbol{u} - \boldsymbol{u}_0) \end{aligned} \tag{3.6}$$

The time separation principle is used to reduce complexity and model dependency. This principle assumes that the aircraft state changes at a much slower rate than the actuator states. Mathematically, this means that $\frac{\partial \boldsymbol{f}}{\partial \boldsymbol{x}}|_{\boldsymbol{x}_0,\boldsymbol{u}_0} \Delta \boldsymbol{x} \ll \frac{\partial \boldsymbol{f}}{\partial \boldsymbol{u}}|_{\boldsymbol{x}_0,\boldsymbol{u}_0} \Delta \boldsymbol{u}$ such that the second term in Eq. (3.6) can be neglected. The resulting equation is:

$$\begin{aligned} \dot{\boldsymbol{y}} &= \underbrace{\frac{\partial \boldsymbol{h}}{\partial \boldsymbol{x}}\Big|_{\boldsymbol{x}_0} \dot{\boldsymbol{x}}_0}_{\dot{\boldsymbol{y}}_0} + \underbrace{\frac{\partial \boldsymbol{h}}{\partial \boldsymbol{x}}\Big|_{\boldsymbol{x}_0} \frac{\partial \boldsymbol{f}}{\partial \boldsymbol{u}}\Big|_{\boldsymbol{x}_0,\boldsymbol{u}_0}}_{\boldsymbol{B}(\boldsymbol{x_0},\boldsymbol{u_0})} \underbrace{(\boldsymbol{u} - \boldsymbol{u}_0)}_{\Delta \boldsymbol{u}} \\ \dot{\boldsymbol{y}} &= \dot{\boldsymbol{y}}_0 + \boldsymbol{B}(\boldsymbol{x_0}, \boldsymbol{u_0}) \Delta \boldsymbol{u} \end{aligned} \tag{3.7}$$

The incremental dynamics are inverted by computing the inverse of the control effectiveness matrix ($\boldsymbol{B}(\boldsymbol{x_0}, \boldsymbol{u_0})$), allowing the command increments $\Delta \boldsymbol{u}$ to be determined from the difference between the pseudo-command $\dot{\boldsymbol{y}}_c = \boldsymbol{v}$ and the measured output derivative. Note that the output and input vectors are assumed to be of equal dimension ($r = m$) and $\boldsymbol{B}(\boldsymbol{x_0}, \boldsymbol{u_0})$ to be full rank, such that it is invertible. This results in:

$$\Delta \boldsymbol{u_c} = \boldsymbol{B}(\boldsymbol{x_0}, \boldsymbol{u_0})^{-1} (\boldsymbol{v} - \dot{\boldsymbol{y}}_0) \tag{3.8}$$

The actual control input is then obtained by adding the computed command increments to the previous control input $\boldsymbol{u}_0$:

$$\boldsymbol{u_c} = \boldsymbol{u_0} + \Delta \boldsymbol{u_c} \tag{3.9}$$

## 3.3. Novel INDI Versions

In addition to the general sensor-based INDI, various extensions have been developed to address its limitations, aiming to enhance robustness, improve disturbance rejection, and mitigate the effects of actuator dynamics and sensor delays. A couple of these alternative INDI methods are handled in this section, highlighting their principles.

### 3.3.1. Decoupled INDI

Coupled dynamics pose challenges during precise manoeuvres, such as autolanding, where high accuracy is of importance. In situations where one wants to pitch up, for example, unwanted following roll behaviour could lead to stability issues. By decoupling the roll, pitch, and yaw angles, more independent and accurate control of each axis can be realised.

A potential decoupling technique is the application of a modified INDI (MINDI) controller to eliminate the coupling between roll and yaw angles [13]. The designed control law for both loops follows a proportional structure between the current and desired states for the inner and outer loops. This means that the virtual control per roll rate consists of the desired state's derivative, then subtracting a gain times the error between the desired angular rate and the measurement. By structuring the control law this way, MINDI explicitly reduces the coupling between roll and yaw dynamics, leading to improved lateral control performance. The designed control law guarantees global asymptotic stability of the system, as it enforces first-order stable differential equations. Furthermore, MINDI enhances robustness against wind disturbances and model uncertainties, outperforming both NDI and standard INDI. The response to a $\pm 5^\circ$ pitch command is shown in Figure 3.1a, and to a $\pm 5^\circ$ roll command in Figure 3.1b.

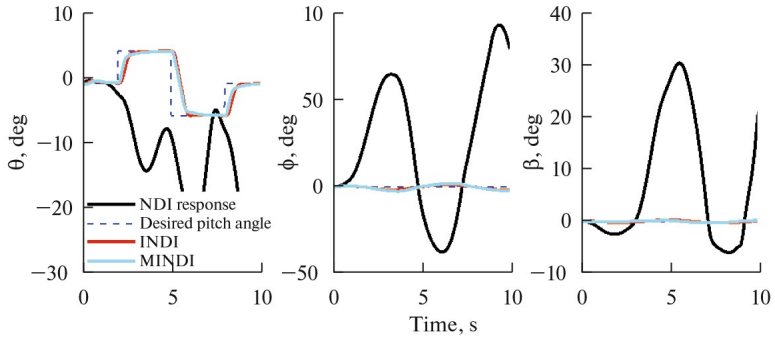


**(a)** Pitch response

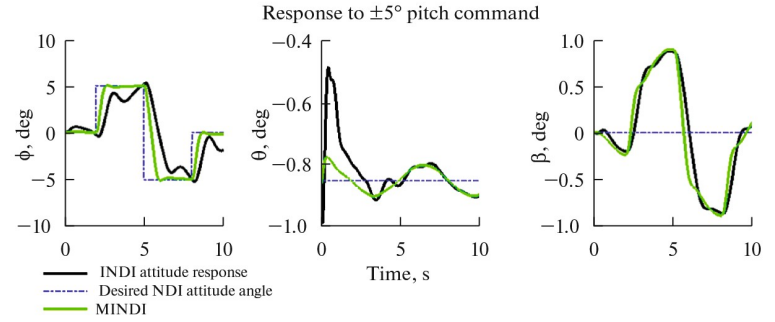


**(b)** Roll response

**Figure 3.1:** Comparison of pitch and roll response to a $\pm 5^\circ$ pitch/roll command respectively in the presence of wind disturbance and model uncertainties [13]

The error in coupling for the pitch angle is reduced by 86% compared to INDI, and MINDI also exhibits superior transient response characteristics, making it a more reliable choice for UAV flight control in uncertain conditions.

A decoupled INDI controller can also be used to deal with the presence of ground effect during landing autonomously [14]. The incorporation of the ground effect is elaborated upon in Chapter 5. The proposed controller aims to decouple the dynamics between the longitudinal and lateral planes to achieve better landing performance, particularly when the ground effect influences the aircraft's response (within a height of approximately one wingspan). A possibility is to treat the longitudinal and lateral dynamics independently, allowing for more precise control over the aircraft's pitch and roll during landing. The approach is applied to the inner and outer loop control laws. The assumptions made for designing the decoupled control law are the following:

1. The rolling motion induced by rudder deflection is neglected ($\frac{\delta \dot{p}}{\delta \delta_r} = 0$)
2. The yawing motion induced by aileron deflection is neglected ($\frac{\delta \dot{r}}{\delta \delta_a} = 0$)
3. When compared to principle inertia, product inertia is negligible and can be neglected ($I_{zx}, I_{xz} = 0$)
4. Weak derivatives are very small compared to strong derivatives and can be neglected ($\frac{\delta C_l}{\delta \delta_r}, \frac{\delta C_n}{\delta \delta_a} = 0$)

It is important to note that these assumptions do not hold in real world scenarios. Therefore, real flight tests would be required to evaluate the actual influence of these factors on system performance. As a result of these assumptions, separate control loops are designed for specific flight tasks, such as the heading hold loop, altitude hold loop, beta cancellation loop, and speed control loop. A diagram of the altitude hold loop is shown in Figure 3.2 to serve as an example.

The decoupling results in improved trajectory tracking and reduced sensitivity to external disturbances during simulation when compared to conventional coupled control methods. This decoupling strategy allows the autonomous landing system to maintain higher accuracy and stability in the presence of wind gusts and other environmental uncertainties.

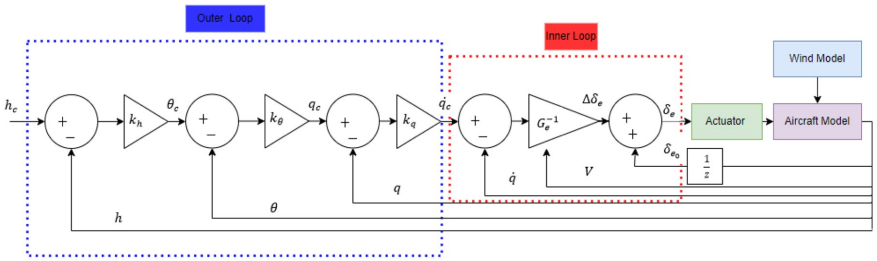


**Figure 3.2:** Decoupled altitude hold loop [14]

### 3.3.2. Adaptive INDI

In most simulations of INDI controllers, actuator dynamics are neglected for simplicity. However, in real-world applications, actuator dynamics do exist and can lead to performance degradation due to time delays, rate limits, and other physical constraints. These factors can affect the controller's accuracy and responsiveness, particularly in complex flight scenarios. To address these challenges, adaptive techniques have been developed to incorporate actuator dynamics and uncertainties into the INDI framework, improving robustness and performance under realistic conditions.

One novel manner of including actuator dynamics is Dynamic Incremental Control Allocation (D-INCA), a method that integrates actuator dynamics into nonlinear control allocation [15]. D-INCA is an extension of the INCA method that, in addition to computing control increments to achieve the desired pseudo-control reference, also accounts for actuator dynamics, which is a limitation of the traditional INCA method. INCA is a combination of INDI with a spline-based control allocation technique, where the spline model is used to capture the control effectiveness matrix. For the inclusion of actuator dynamics, it is assumed that these can be adequately modelled using a linear first-order dynamics model:

$$\boldsymbol{\delta}_{k+1} = \boldsymbol{A}\boldsymbol{\delta}_k + \boldsymbol{B}\boldsymbol{u}_k \tag{3.10}$$

By incorporating actuator dynamics, D-INCA improves control accuracy while ensuring the increment remains within the set limits imposed by the physical actuator position and rate constraints. For non-over-actuated systems ($p = m$), one can directly solve for $\boldsymbol{u}_k$ from Eq. (3.11):

$$\Delta\tau = \nabla_\delta \boldsymbol{\Phi}(\boldsymbol{A}\boldsymbol{\delta}_k + \boldsymbol{B}\boldsymbol{u}_k - \boldsymbol{\delta}_k) \tag{3.11}$$

For over-actuated systems, a cost function can be used, depending on the first-order actuator dynamics (Eq. (3.10)) and the control effectiveness Jacobian $\nabla_\delta \boldsymbol{\Phi} = \frac{\partial \boldsymbol{\Phi}(\boldsymbol{x}_k, \boldsymbol{\delta}_k)}{\partial \boldsymbol{\delta}}$. The introduction of Adaptive D-INCA (AD-INCA) further enhances the method by estimating actuator dynamics online using recursive least squares (RLS), which allows the system to adapt to changing conditions (i.e. disturbances) and actuator failures. Actuator parameters are updated only when a threshold of excitation is detected, preventing issues such as covariance windup. The resulting (A)D-INCA block diagram can be observed in Figure 3.3.

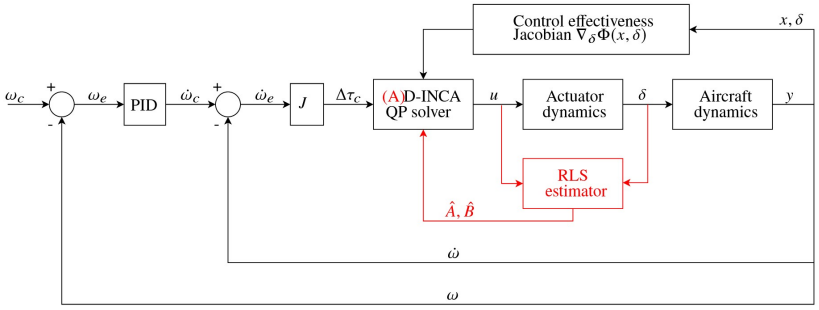


**Figure 3.3:** (A)D-INCA FCS block diagram [15]

Given the similarities between INCA and INDI, the principles behind D-INCA could be applied to enhance INDI's performance by accounting for actuator dynamics. This could mitigate the effects of actuator

delays and limitations, improving INDI's robustness and accuracy in real-world applications. Additionally, incorporating adaptive elements for actuator failure could further increase INDI's reliability in autonomous flight systems [15].

Following the philosophy of online computations, online parameter estimation has the potential to correct for the uncertainty in the on-board control effectiveness model [16]. Both the aerodynamic model and inertia uncertainties are lumped together in one uncertainty term ($g(\boldsymbol{x}_0, \boldsymbol{u}_0) = I_{yy}^{-1} C_{m_{\delta_e}}(\boldsymbol{x}_0, \boldsymbol{u}_0)$) and a correction factor is estimated online, used to scale the deviating model until it converges to the actual CE of the aircraft. This allows for linear parameter estimation methods, in this case based on the Least-Mean-Square (LMS) algorithm [17]. The regression model for the uncertain pitching motion can be expressed as:

$$\dot{q} - \dot{q}_0 = \Delta\dot{q} = \hat{C}\,\overline{q}_0 S\bar{c} g_{nom}(\boldsymbol{x}_0, \boldsymbol{u}_0)\Delta\delta_e = \hat{C} G_{nom}(\boldsymbol{x}_0, \boldsymbol{u}_0)\Delta\delta_e \triangleq \hat{C}\phi(\boldsymbol{x}_0, \boldsymbol{u}_0) \tag{3.12}$$

where $\phi(\boldsymbol{x}_0, \boldsymbol{u}_0)$ is the regression model basic function containing the nominal CE model. This leads to the following LMS parameter estimation algorithm:

$$\hat{C} = \hat{C}_0 + \mu\phi(\boldsymbol{x}_0, \boldsymbol{u}_0)(\Delta\dot{q} - \hat{C}_0\phi(\boldsymbol{x}_0, \boldsymbol{u}_0)) \tag{3.13}$$

which will be used to scale the nominal CE model as follows, to obtain the elevator deflection increment of the LMS adaptive INDI pitch rate control law:

$$\Delta\delta_e = (\hat{C} G_{0,nom})^{-1}(v_q - \dot{q}_0) \tag{3.14}$$

Linear parameter estimation methods have the potential for application because of their generally lower computational complexity with respect to nonlinear estimation methods. Application of this method leads to a decrease in variations in Handling Quality Sensitivity (HQ&S) results, but also to significantly varying PI compensator gains over different flight conditions. If a smoother gain scheduling is desired, it is proposed to use a different scheduling method, for example based on the dynamic pressure or to optimise all designs for one specified cross-over frequency.

### 3.3.3. Hybrid INDI

Model-based INDI uses the modeled dynamics $\boldsymbol{f}_{mod}(\boldsymbol{x}_0) + \boldsymbol{g}_{mod}(\boldsymbol{x}_0)\boldsymbol{u_0}$ of an on-board model rather than a sensor-based estimation, instead of relying on the Taylor series expansion used in sensor-based INDI [18]. The resulting control law is:

$$\boldsymbol{\Delta u} = \boldsymbol{g}_{mod}^{-1}(\boldsymbol{x_0})(\boldsymbol{v} - \boldsymbol{f}_{mod}(\boldsymbol{x}_0)) \tag{3.15}$$

which is similar to the NDI control law. This approach requires a full system model and therefore lacks robustness against model mismatches. In Hybrid INDI, this model-based method is combined with the sensor-based method to enhance the stability of angular acceleration estimation by reducing the influence of sensor noise and disturbances. Sensor-based estimation captures low-frequency dynamics, while model-based estimation accounts for high-frequency components [11].

Model-based INDI does not introduce the delays associated with obtaining and processing sensor measurements, making it well-suited for the high-frequency dynamics where a fast response is required. Conversely, at low frequencies, the real-time sensor feedback is used to retain the robustness against model mismatches. A complementary filter fuses model-based and sensor-based estimates, ensuring a smooth transition between these two methods. Block diagrams of a classical complementary filter and a complementary filter for angular acceleration estimation are shown in Figure 3.4.

As illustrated in Figure 3.4, the modelled acceleration $\dot{x}_m$ is combined with the gyroscope measurement $x_s$ through a complementary filter [19]. The diagram shows an integral block in the feedback path because the control loop uses the angular rate error $e = x_s - \frac{1}{s}\hat{\dot{x}}$ to drive the estimated angular acceleration. This structure enables the innovation signal $i$ to serve as corrective feedback without the need for explicit differentiation of the noisy gyroscope signal.

The dynamics in the Laplace domain can be described by the acceleration estimate as follows:

$$\hat{\dot{x}} = (x_s - \frac{1}{s}\hat{\dot{x}})(K_P + \frac{K_I}{s}) + \dot{x}_m \tag{3.16}$$

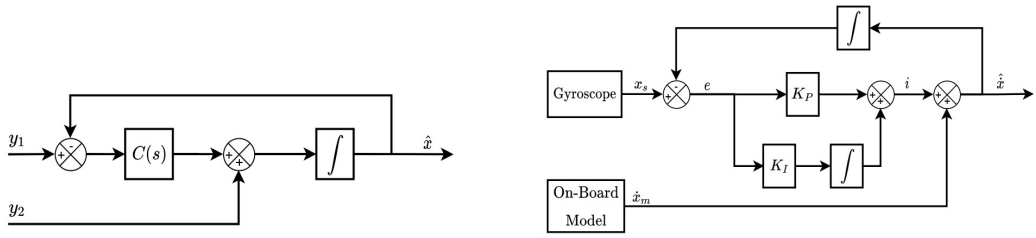


**Figure 3.4:** Classical complementary filter (left) vs. complementary filter for angular acceleration estimation (right) [19]

such that the error and innovation dynamics are defined as:

$$E(s) = x_s - \frac{1}{s}\hat{\dot{x}} \tag{3.17}$$

$$I(s) = E(s)(K_P + \frac{K_I}{s}) \tag{3.18}$$

resulting in $\hat{\dot{x}} = I(s) + \dot{x}_m$. By rearranging Eq. (3.16), the characteristic equation is defined as:

$$\begin{aligned}
\hat{\dot{x}} &= (x_s - \frac{1}{s}\hat{\dot{x}})(K_P + \frac{K_I}{s}) + \dot{x}_m \\
\hat{\dot{x}}\left(1 + \frac{K_P + \frac{K_I}{s}}{s}\right) &= \left(K_P + \frac{K_I}{s}\right)x_s + \dot{x}_m \\
\hat{\dot{x}}\left(\frac{s^2 + K_P s + K_I}{s^2}\right) &= \left(K_P + \frac{K_I}{s}\right)x_s + \dot{x}_m \\
\hat{\dot{x}} &= \frac{s^2}{s^2 + K_P s + K_I}\left(K_P + \frac{K_I}{s}\right)x_s + \frac{s^2}{s^2 + K_P s + K_I}\dot{x}_m \\
\hat{\dot{x}} &= \underbrace{\frac{K_P s + K_I}{s^2 + K_P s + K_I}}_{S(s)} s\, x_s + \underbrace{\frac{s^2}{s^2 + K_P s + K_I}}_{M(s)}\dot{x}_m
\end{aligned} \tag{3.19}$$

The sensor and model transfer functions ($S(s)$ and $M(s)$ respectively) are complementary, adhering to the identity $\frac{1}{s}S(s) + M(s) = 1$. The transfer functions $S(s)$ and $M(s)$ govern the signal fusion, leveraging the strengths of each input. $S(s)$ functions as a low-pass filter on the sensor measurement $x_s$, smoothing high-frequency noise while retaining low-frequency disturbances and model mismatches. $M(s)$ acts as a high-pass filter on the modelled acceleration $\dot{x}_m$, exploiting the model's rapid response to control inputs. This complementary blending allows Hybrid INDI to preserve the robustness of sensor-based INDI against model uncertainties while achieving the necessary fast dynamic response. The filter's design is parametrized by the natural frequency $\omega_n$ and damping coefficient $\zeta$, which are set by the linear controller gains as $K_I = \omega_n^2$ and $K_P = 2\zeta\omega_n$. These parameters define the cutoff frequency and overall response characteristics. A lower $\omega_n$ enhances noise attenuation, but slows the system's reaction time.

To increase robustness against delays, one can use the low-pass component of the complementary filter in a synchronisation filter. The cost function used to evaluate the performance of the control system consists of the RMS of tracking error $\epsilon$ and the additional actuator deflection per time step $\delta_E$. A block diagram of the overall system is presented in Figure 3.5 [19].

During simulation, Hybrid INDI demonstrates a reduced overshoot and a faster settling time when measurement delays are underestimated. Additionally, even without a synchronisation filter, Hybrid INDI achieves satisfactory performance due to the transient state derivative provided by the on-board model. The simulation performance in the presence of measurement delays and aerodynamic uncertainties is shown in Figure 3.6 [19].

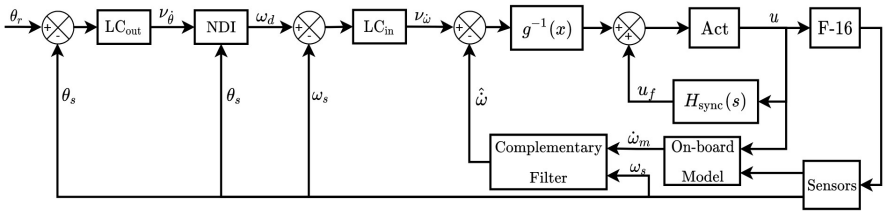


**Figure 3.5:** Overall block diagram of Hybrid INDI [19]

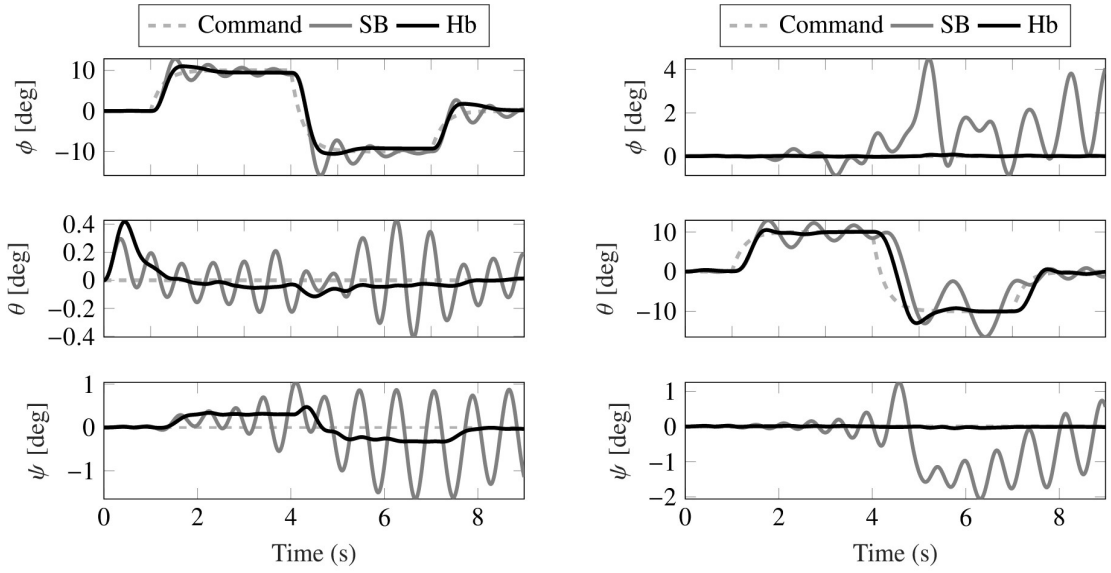


**Figure 3.6:** Tracking performance of roll doublet input (left) and pitch doublet input (right) [19]

### 3.3.4. Kinematics Based INDI

In the derivation of basic INDI one inverts the dynamics of force or moment equations. Since these dynamics contain information about the airframe and actuator models, it is not possible to be completely free of model uncertainty. Therefore, the application of INDI to kinematics has been researched [20]. The derivation procedure is the same, but which variables are set to $\boldsymbol{x}$ and $\boldsymbol{u}$ are different. Here, $\boldsymbol{x} = [V, \psi, \gamma]$, and $\boldsymbol{u} = [a_x, a_y, a_z]$. The resulting state space equation is shown below:

$$\begin{bmatrix} \dot{V} \\ \dot{\psi} \\ \dot{\gamma} \end{bmatrix} = \begin{bmatrix} f(V) \\ f(\psi) \\ f(\gamma) \end{bmatrix} + \begin{bmatrix} 1 & 0 & 0 \\ 0 & \frac{1}{V} & 0 \\ -\frac{\sin\gamma}{V\cos(\gamma+1)} & 0 & \frac{1}{V\cos(\gamma+1)} \end{bmatrix} \begin{bmatrix} a_x \\ a_y \\ a_z \end{bmatrix} \tag{3.20}$$

After applying the same procedure as before combined with the time-scale separation principle, the guidance law can be expressed as:

$$\begin{bmatrix} a_x \\ a_y \\ a_x \end{bmatrix} = \begin{bmatrix} a_{x0} \\ a_{y0} \\ a_{z0} \end{bmatrix} + \begin{bmatrix} 1 & 0 & 0 \\ 0 & V & 0 \\ \sin\gamma & 0 & \frac{1}{V(\cos\gamma+1)} \end{bmatrix} \begin{bmatrix} \nu_{\dot{V}} - \dot{V}_0 \\ \nu_{\dot{\psi}-\dot{\psi}_0} \\ \nu_{\dot{\gamma}-\dot{\gamma}_0} \end{bmatrix} \tag{3.21}$$

Figure 3.7 shows the block diagram of the kinematics-based INDI guidance law. The shaded region contains the INDI, with a PID controller in front. The system model is a point-mass model. The inner loop is represented as a first-order low pass filter, under the assumption that it has been stabilised. The expression can be found below.

$$\begin{cases} \dot{a}_x = -\dfrac{1}{\tau_{a_x}} a_x + \dfrac{1}{\tau_{a_x}} a_{xc} \\ \dot{a}_y = -\dfrac{1}{\tau_{a_y}} a_y + \dfrac{1}{\tau_{a_y}} a_{yc} \\ \dot{a}_z = -\dfrac{1}{\tau_{a_z}} a_z + \dfrac{1}{\tau_{a_z}} a_{zc} \end{cases} \tag{3.22}$$

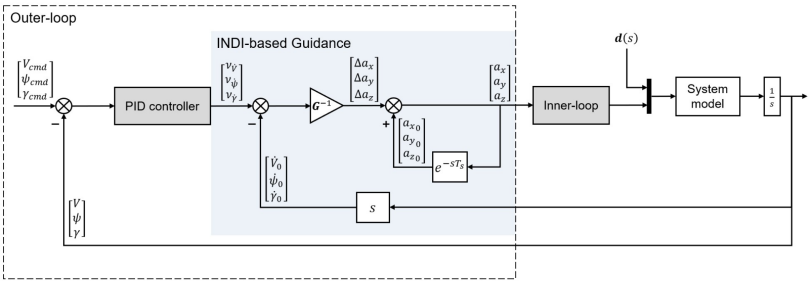


**Figure 3.7:** Kinematics-based INDI block diagram [20]

From the simulation results, it is evident that the states overshoot less and closely follow the reference trajectory. However, this control system is developed under the assumption of a stable attitude loop, which may not hold in the event of an actuator failure, as the attitude would not be directly affected. To address this limitation, future work will extend the current point-mass model to a full six degree-of-freedom representation. This extension will also enable the controlled injection of actuator failures for more realistic evaluation.

# 4

# Real-World Effects and Stability Analysis

Some real-world effects may negatively impact performance and stability. In this chapter, these effects are explained, along with possible coping mechanisms. Finally, stability analyses are introduced.

## 4.1. Delay and Dynamic Effects

From simulations it is observed that even small measurement delays are of significant concern when using INDI [3]. Because by using INDI the demanded angular acceleration is considered to be an incremental step in time from the measured angular acceleration, any noticeable delay will violate the assumption of the incremental step, causing loss of performance [21].

### 4.1.1. Influence of Measurement Delays

The derivation by Sieberling et al. is used to explain why time delay causes problems in the application of real-world sensors [21]. Consider the linearising control law for INDI:

$$\Delta\delta = (\mathbf{M}_c)_\delta^{-1}\bar{\mathbf{J}}(\boldsymbol{v} - \dot{\boldsymbol{\omega}}_0) \tag{4.1}$$

In the presence of time delay, the measured angular acceleration experiences a delay, denoted by subscript $\tau$, hence Equation 4.1 becomes:

$$\Delta\delta = (\mathbf{M}_c)_\delta^{-1}\bar{\mathbf{J}}(\boldsymbol{v} - \dot{\boldsymbol{\omega}}_\tau)$$

If one uses this as the system input, it becomes evident that not all terms will be cancelled:

$$\begin{aligned} \dot{\boldsymbol{\omega}} &= \dot{\boldsymbol{\omega}}_0 + \bar{\mathbf{J}}^{-1}(\mathbf{M}_c)_\delta(\mathbf{M}_c)_\delta^{-1}\bar{\mathbf{J}}(\boldsymbol{v} - \dot{\boldsymbol{\omega}}_\tau) \\ \dot{\boldsymbol{\omega}} &= \boldsymbol{v} + \dot{\boldsymbol{\omega}}_0 - \dot{\boldsymbol{\omega}}_\tau = \boldsymbol{v} + \dot{\boldsymbol{\omega}}_{\Delta\tau} \end{aligned} \tag{4.2}$$

which shows that the closed-loop system is not linearised, as an extra term remains that is varying with time $\dot{\boldsymbol{\omega}}_{\Delta\tau}$. This variable represents the difference in the angular acceleration at two different points in time. As the delay decreases, its influence decreases as well.

### 4.1.2. Obtaining the Angular Acceleration

Time delays are inherent to the PH-LAB Cessna Citation, arising from both intrinsic delays within the FBW system and data buses, as well as delays introduced by signal filtering in the control design [17]. Hence, this problem must be addressed in the design of its control system. Time delays inevitably occur in the control system due to the process of acquiring the angular acceleration required for INDI. If accelerometers are not available, the angular accelerations have to be obtained in a different manner. One of the solutions posed in literature is the use of a predictive filter to obtain the angular accelerations necessary for INDI [21]. This predictive filter aims to adjust the system to account for the introduced time delay, since elimination is impossible. The predictive filter will not cause larger problems with sensor noise than a first or second-order filter, since the amplification is much smaller than for differentiation. Moreover, an advantage of linear prediction is that it guarantees bounded-input bounded-output stability. The linear predictive filter used is shown in Equation 4.3:

$$\dot{\omega}_t = \sum_{i-1}^{5}[\theta_{\omega_j}\omega_{(t-idt} + \theta_{r_j}r_{(t-idt]} + \epsilon \tag{4.3}$$

where $r_j$ is the reference angular rate with $j$ changing for roll, pitch and yaw rate. The coefficients ($\theta$) are computed by least-squares estimation. This requires a data collection $H$ of angular rates and angular rate references, and a data set of predicted angular accelerations $z$. The final equation to obtain the coefficients is then:

$$\theta = (H^T H)^{-1} H^T z \tag{4.4}$$

The predictive filter is designed for an aircraft with an ideal response. In reality, the response is not ideal since control surface deflections are not instant but have their own dynamics, meaning the controller is more sensitive to model uncertainties than a regular INDI controller using a differentiator. In addition, when designing such a filter offline, these require training resulting in less robustness regarding noise and disturbances [3]. A solution could be updating the filter online, which does require more computational effort.

Alternatively, a simpler first- or second-order filter can be used, but these introduce the aforementioned delays. A popular solution for this problem is to apply the filter used to obtain the angular acceleration to the control surface deflection as well, to synchronise with $\dot{\boldsymbol{x}}_0$ [7] [16] [17] [20] [22]. After application of this filter, the subscript $0$ is often replaced by subscript $f$ denoting the filter. Such a filter has been used during a test flight for the PH-LAB Cessna Citation as well [7]. The used second-order filter is shown in Eq. (4.5) where $\omega_n$ could be lowered to 20 rad/s and $\zeta = 1$ before serious performance degradation was observed.

$$\frac{\omega_{n_{fil}}^2}{s^2 + 2\zeta\omega_{n_{fil}} s + \omega_{n_{fil}}^2} \tag{4.5}$$

### 4.1.3. Actuator Dynamic and Compensation

Research on the intrinsic delays has been performed as well. To reduce the actuator dynamics induced delays, more aggressive inputs can be used. This potentially could lead to actuator saturation because of physical limits, which may cause stability issues [23]. In multiple researches, Pseudo Control Hedging (PCH) has been proposed to face this problem [7] [10]. The effect of actuator saturation is solved by modifying the virtual control input rather than the actuator output. If the input error signal becomes too large for the actuators to handle, a signal $v_s$ (the input under the actuator dynamics) is produced that counteracts the virtual control law of the first-order reference system. This helps prevent the system from attempting to track the commanded references during actuator saturation. A resulting first-order reference system with a saturation filter is shown in Figure 4.1. In affine nonlinear systems, the PCH signal $v_s$ can

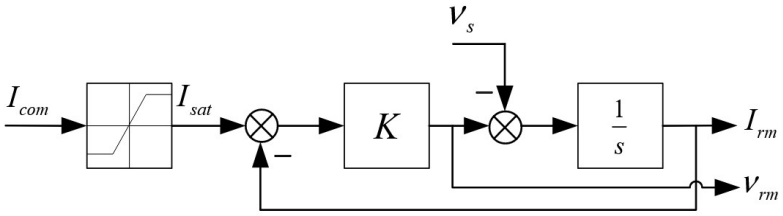


**Figure 4.1:** First order reference system with saturation filter [10]

be determined using:

$$\begin{aligned} v_s &= [\dot{x}_0 + G(x_0, u_0)(u_{des} - u_0)] - [\dot{x}_0 + G(x_0, u_0)(u - u_0)] \\ &= G(x_0, u_0)(u_{des} - u) \end{aligned} \tag{4.6}$$

A flight test on the PH-LAB Cessna Citation proved successful under a control system using INDI with PCH [7]. Here, the PCH signal was obtained using

$$\boldsymbol{v}_h = \underbrace{\boldsymbol{M}_{c_\delta}(\hat{\boldsymbol{x}}_0, \boldsymbol{J}_{\hat{p}}(\hat{\boldsymbol{p}})^{-1}}_{L_{G_{\boldsymbol{h}}}}[\boldsymbol{u} - \hat{\boldsymbol{\delta}}] \tag{4.7}$$

As the PCH signal only depends on the aerodynamic model's CE $M_{c_\delta}$, it can be added to the incremental control method without introducing new model dependencies.

A different manner to compensate for actuator dynamics induced delays is a novel version of the incremental nonlinear control allocation (INCA) method that uses a first-order actuator dynamics model included in the dynamic inversion loop, which is handled elaborately in Section 3.3 [15]. The resulting Dynamic INCA (D-INCA) controller allows for more aggressive inputs, no longer requiring the usage of, for example, PCH. In addition, an adaptive version of D-INCA (AD-INCA) is introduced that uses online parameter estimation for the on-board actuator model, increasing robustness.

## 4.2. Noise and Bias

Accurate and timely sensor measurement are important for the success of INDI autoland systems. The performance of INDI partly relies on feedback to compute control corrections, making sensor characteristics a big factor in overall system stability and robustness. Sensor dynamics include several aspects, but most importantly noise and bias. These factors do not only introduce time delays (see Section 4.1.1) but also impact the accuracy and reliability of the state estimation, which can influence performance [3].

Noise refers to all unwanted random variations that affect the FCS. Noise can originate from multiple sources, such as intrinsic electronic noise in sensor hardware, environmental noise i.e. vibration-induced noise in accelerometers, and communication and quantisation noise in digital signal processing. Since the sensor-based control algorithm depends on acceleration measurements, sensor noise can be problematic. Unfortunately, inertial measurements from gyros and accelerometers always introduce some level of noise and bias. In fact, during a flight test of an NDI controller, noise in the lateral accelerometer caused issues that led to an unsuccessful flight [24].

Therefore, both noise affecting the airframe and noise present in measured feedback signals are considered important factors and will be included during the design of the controller. This can be realised by adding random signals to the measured feedback signals or the airframe input which will simulate the effect of noise on the controller. This noise can simply be white noise and can be introduced to one or more variables during simulation. In addition to the above, if gyro measurements are differentiated to obtain the angular acceleration, additional noise is introduced [7]. This adds to the importance of this analysis. Possible noise reduction techniques include but are not limited to Kalman Filtering (KF) and the use of complementary filters [25] [19]. In addition, using wavelet filtering techniques or an artificial neural network may increase performance relative to low-pass filtering, but these techniques also introduce time lags and reduce the effective sensor bandwidth [26].

Bias is a systematic measurement offset where a sensor consistently reports a deviation from the true value. It is present for all accelerometers and gyros and is independent of the aircraft dynamics [26]. An illustration of bias is shown in Figure 4.2. Unlike random noise, bias is persistent and can lead to cumulative errors if not corrected, which may lead to trajectory deviations during landing [21].

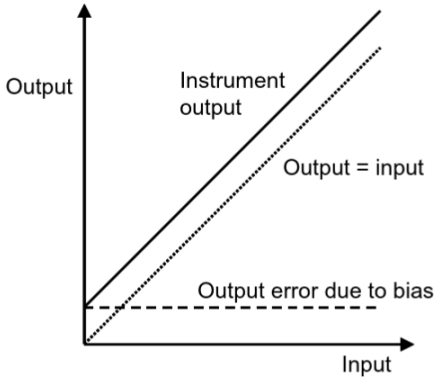


**Figure 4.2:** Sensor with a bias error [26]

Fortunately, the bias characteristics for the PH-LAB Cessna Citation have been recorded in the past and can be found in Section 7.1 [3] [7]. It should be noted however that these values are approximations and cannot be assumed to be true in the application of real flight. Alternatively, bias can be estimated online, for example using adaptive filtering techniques as described in Section 3.3 for more accurate inclusion.

## 4.3. Stability Analyses

INDI controllers are based on incremental inputs, providing a higher level of robustness in the presence of model mismatches. This is achieved through the integration of sensor information, which enhances the system's ability to adapt to disturbances. Although recent flight tests have demonstrated working INDI control systems [7] [17], there are still theoretical gaps regarding their robustness to uncertainties, time delays and controller sampling frequency [9]. The controller sampling frequency is often referred to as "required to be high enough", without quantification. Sometimes, a working sampling frequency obtained through experimentation is given, i.e. the 100 Hz documented by Stam and de Visser (for innovative control effectors) [15]. However, insufficient sampling rates can degrade controller performance [27]. Understanding how sampling frequency and time delays influence system stability is crucial to ensure the controller's effectiveness in real-world applications.

### 4.3.1. Discrete-Time Stability

It is possible to reduce the discrete-time system of INDI controllers to a single transfer function, enabling stability assessment via the characteristic polynomial of this transfer function [3]. The system is asymptotically stable if all roots of the characteristic polynomial have a magnitude smaller than one. Jury's stability criterion then offers a tabular method to check the system's stability without solving for the roots individually. Stability regions have been mapped for an INDI control system applied to the PH-LAB Cessna Citation model. The resulting regions can be found in Figure 4.3 for a baseline system without time delays or control effectiveness uncertainties. The results indicate that a sampling time of less than 0.02 s is sufficient to ensure a decent stable region concerning variations in $F$, $K_u$ and $K_x$, given the typical values of the aircraft.

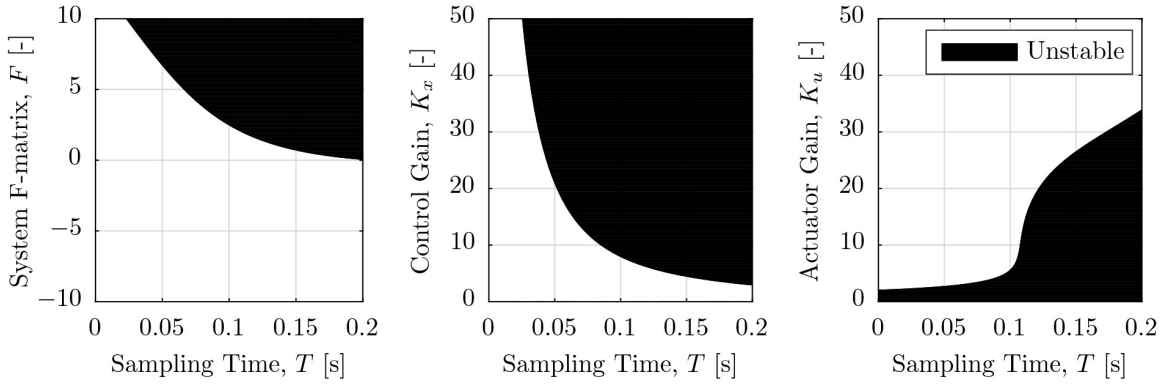


(a) $K_u = 13$, $K_x = 7$ (b) $F = 2$, $K_u = 13$ (c) $F = 2$, $K_x = 7$

**Figure 4.3:** Stability for baseline INDI controller [3]

To analyse the impact of measurement delays on INDI controller stability, four system configurations were examined:

1. Baseline system without delays (Figure 4.3c)
2. System where only the state derivative measurement is delayed (Figure 4.4a)
3. System where only the actuator measurement is delayed (Figure 4.4b)
4. System where both measurements are delayed equally (Figure 4.4c)

The results indicate that the baseline system and the system with equally delayed measurements exhibit the largest stable regions, highlighting the importance of synchronisation. Furthermore, it was observed that the combination of a discrete-time controller and a continuous-time system, when combined with actuator measurement delays, leads to a decrease in system stability. This finding emphasises the preference to avoid using a unit delay in actuator measurements for maintaining stability. Additionally, it was found that delays in state derivative measurements and actuator measurements affect stability differently. State derivative delays amplify control inputs, resulting in faster instability due to negative feedback, while

actuator delays tend to dampen control inputs and result in a slower onset of instability due to positive feedback. This distinction suggests that while INDI controllers can tolerate some delays, they are more sensitive to delays in the state derivative measurements. Control effectiveness (CE) uncertainty does not

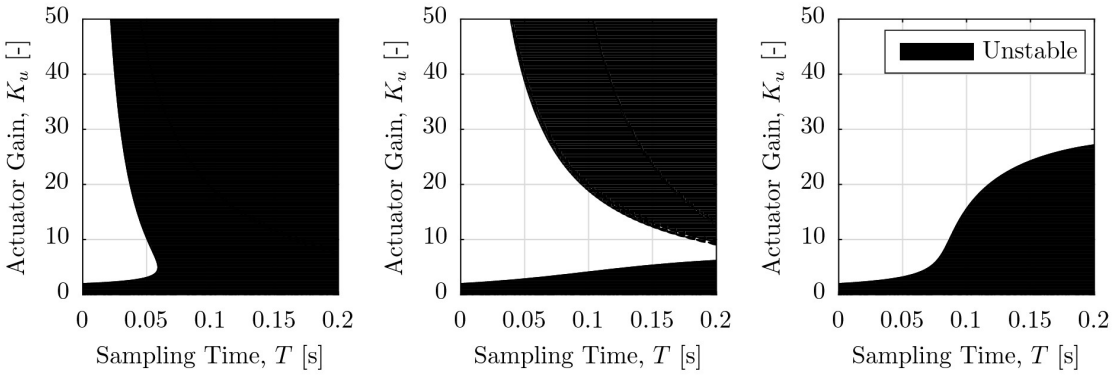


(a) State derivative (b) Actuator (c) Actuator and state derivative

**Figure 4.4:** Stability with delays: $F = 2$, $K_x = 7$ [3]

significantly affect the stability of INDI controllers as long as the sampling time remains below 0.02 s in this case [3]. Over a wide range of CE uncertainties, stability is maintained. However, for low or negative values of the uncertainty ratio ($\gamma$), instability can occur. This behaviour is observed not only in discrete-time systems but also in continuous-time closed-loop systems, underscoring the importance of accurate control parameter tuning.

### 4.3.2. Frequency-Domain and Time-Domain Analysis

A stability analysis can determine robustly stable time-delay regions [27]. Such an analysis may employ both frequency-domain and time-domain methods. For example, the frequency-domain approach utilises the analytic curve frequency sweeping method in combination with the edge theorem, providing a suitable framework for robust stability assessment. Frequency sweeping is a technique used to analyse the frequency response of a system by varying the input signal frequency over a range and observing the output. It helps to identify system characteristics such as resonance, bandwidth, stability margins, and dynamic behaviour. In the time domain, the stability of retarded time-delay systems (TDSs) can be evaluated using existing stability results, while sub-polytopic uncertainties can be analysed by verifying vertex conditions.

The effectiveness of these methods was validated through simulations, including applications to a pendulum system and an INDI-controlled short-period aircraft dynamics model [27]. The study also explored the impact of a zero-order hold filter on stability and proposed extensions for future research. Specifically, it suggested applying these stability analysis methods to Incremental Backstepping (IBS), a competing incremental control technique, to compare time-delay stability regions between IBS and INDI. Additionally, the need to extend stability results to systems with multiple incommensurate delays and distributed delays was highlighted, as these are more representative of real-world applications. Further research was suggested to develop matrix inequalities for handling norm-bounded uncertainties, offering a more manageable but possibly more conservative approach to robust stability analysis.

The stability and performance of INDI controllers applied to single-input single-output (SISO) linear time-invariant (LTI) systems has been analysed [22]. By deriving analytical transfer functions for the incremental controller whilst incorporating elements such as actuator dynamics, sensor noise, time delays and model mismatches, the impact of time delays on system stability can be assessed by determining the time delay margin. The time delay margin is the maximum allowable time delay before the system becomes unstable. This margin can be found by analysing the closed-loop characteristic equation with an introduced time delay term. By examining the roots and identifying critical values for the time delays resulting in instability, the system's time delay margin follows. To share these results, two time delays ($\tau_1$ sensor delay and $\tau_2$ actuator delay) are plotted relative to each other for different gains, see Figure 4.5. This investigation allows for the following conclusions:

- The actuator delay $\tau_2$ can always be increased for small sensor delays $\tau_1$, meaning that the system is more vulnerable to sensor delays than actuator delays
- For a large sensor delay, the system only remains stable with a similar size of actuator delay
- Increasing the control gain will result in smaller stability regions and reduces the power of synchronisation

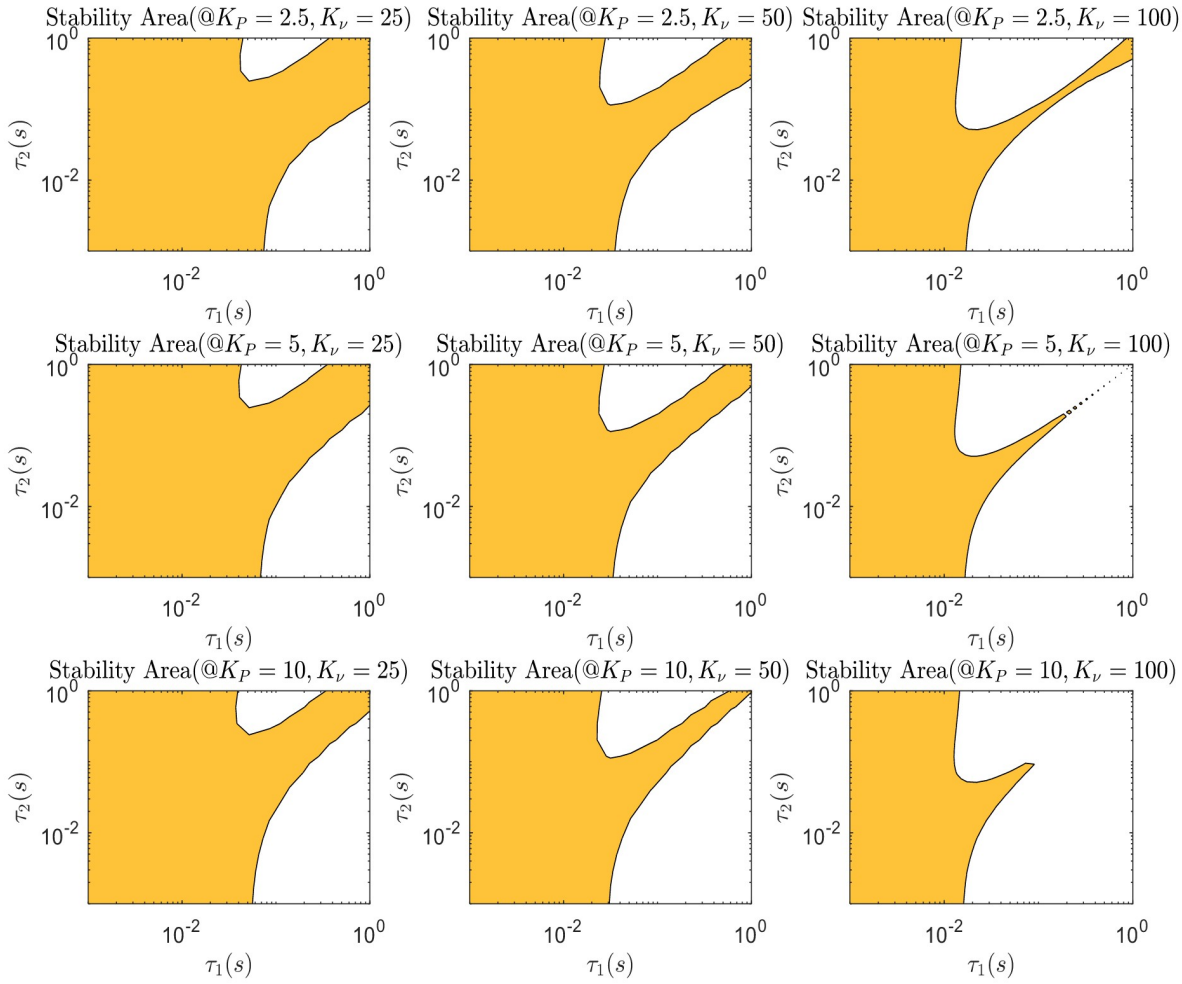


**Figure 4.5:** Stability areas of two time delays for the incremental controller with different gains [22]

This analysis highlights the role of synchronisation in maintaining stability. For lower control gains, synchronised time delays do not necessarily lead to instability, but for $K_v = 100$, increasing synchronised time delays eventually results in instability. Furthermore, actuator measurement delays do not destabilise the closed-loop system as long as the sensor delay remains within the delay margin. However, sensor time delay is a critical factor for stability, and its impact can be mitigated by introducing a synchronisation delay in the actuator measurement loop. While this approach enhances delay tolerance, it also reduces the stability margin, requiring higher control gains, which in turn may lead to instability, resulting in a tradeoff. In addition to analysing time delay effects, the influence of sensor and filter dynamics compensation on stability margins has been researched [22]. By deriving and comparing open-loop transfer functions for different compensation strategies, it is possible to assess how incorporating compensation into the actuator measurement loop affects gain margin, phase margin, and time delay margin. Results indicate that stability margins improve when sensor and filter dynamics are accounted for in the control loop. Moreover, it was found that compensating for additional linear dynamics aimed at measurement noise attenuation further enhances robustness. However, these modifications also influence the overall system response, highlighting the tradeoffs involved in stability enhancement [22].

The introduction of Pseudo Control Hedging (PCH, see Section 4.1.3) in a control system requires further analysis on the influence on stability. PCH is a popular method to handle actuator nonlinearities such as saturation. A possible approach involves comparing the open-loop transfer functions with and without PCH by examining their ratio, as described by Eq. (4.8).

$$R(s) = \frac{L_{u,PCH}}{L_u} = \frac{s + K_r}{s + K_r + K_v T_{act}(K_p - K_r)} \tag{4.8}$$

The results show that the influence of PCH on stability is highly dependent on the relative values of control gains. When properly configured, PCH increases stability margins by shifting gain and phase in the low-frequency domain, improving robustness. However, if misconfigured (specifically when the proportional gain $K_p$ is lower than the hedging gain $K_r$) PCH can reduce stability, and this negative effect becomes more pronounced for higher values of the actuator gain $K_v T_{act}$. This finding highlights the sensitivity of stability to gain tuning, reinforcing the importance of careful parameter selection in practical implementations [22].

### 4.3.3. Time Delay Margins

Time delay margins are not only of importance for INDI. They have also been investigated for Incremental Backstepping (IBS), a control methodology derived from Lyapunov-based Backstepping, which shares key properties with INDI, particularly in its ability to handle model uncertainties and leverage incremental control principles. [28]. Koschorke et al. investigated time-delay margins for IBS, addressing the broader challenge of designing robust nonlinear control laws without requiring explicit system model knowledge. Rather than relying on traditional time-delay analysis techniques such as Lyapunov-Krasovskii functionals, Koschorke proposed a novel approach to estimate delay margins based on controller gain magnitudes and constrained state variable values. This approach aligns well with the principles of incremental control, where direct measurements of system states and their derivatives are leveraged to enhance robustness against uncertainties. While this work specifically focuses on IBS, its insights are relevant to INDI-controlled systems.

Both approaches aim to achieve robust stability in the presence of model uncertainties, and both benefit from high update rates to mitigate the effects of unmodeled dynamics. The delay estimation methods explored provide a potential framework for analysing the delay margins of INDI controllers, offering a complementary approach to existing frequency-domain stability techniques. By incorporating time delay margin analysis into the design and validation of an INDI-based autoland system, it becomes possible to increase reliability during operation under realistic conditions. Future work could explore the application of Koschorke's delay estimation approach to INDI, assessing its effectiveness in quantifying the robustness of an autoland controller against various sources of delay.

A novel metric called the relative singular perturbation margin ($SPM_R$) allows the stability analysis of MIMO systems in contrast to PM which is limited to SISO systems [29]. Moreover, the specific focus is on stability analysis with respect to delays. The relationship between the $SPM_R$ and the PM is established for SISO systems. The method is limited to a single equilibrium point, while in flight control applications transitions to several equilibrium points shall be considered. Applying the method at these diverse equilibrium points then leads to distinct values. The $SPM_R$ depends on time delays $\tau_a$ and $\tau_m$ and offers insights into the sensitivity of the INDI control approach to delays. If its value is > 1, the phase margin is increased, whilst a value < 1 indicates a reduction in the PM, showing decreased robustness. The equation used to obtain the $SPM_R$ is shown below:

$$SPM_R = \frac{\epsilon^*_{INDI}}{\epsilon^*_{NDI}} \tag{4.9}$$

Delays in the state derivative for a MIMO rate controller of a fixed-wing aircraft increase the $SPM_R$, while delays in the input measurement signal have the opposite effect, complementing previous findings. Furthermore, as the angular rates increase, the robustness decreases. This indicates that higher angular rates make the system more vulnerable to the impact of slower actuator dynamics.

# 5

# Autoland

Current autoland control systems are designed for good performance under nominal flight conditions and are generally unable to deal with very different situations, such as actuator failure or heavy crosswinds. This has fueled interest in the area of fault tolerant control systems (FTCSs) for autoland. This section shows used manners related to path definition applicable to INDI autoland.

## 5.1. Straight Approach Path

Generally, the landing can be divided into three phases; approach, glideslope and flare. Singh et al. have defined a path planning method for small and light-weight UAVs [30]. During approach, the aircraft is aligned with the runway such that the glideslope can be started at a specified height, meaning the critical control is heading control. During the glideslope, the height of the vehicle above the ground is controlled, where the desired height is computed as a function of forward distance. The resulting glideslope is a straight line with the computed flight path angle as its slope. The flare path is an exponential curve intersecting the ground at the touchdown point. The design parameters for this landing are then the touchdown point location and the sink rate at touchdown, allowing for tuning as preferred. The goal of the control design remains to closely track the desired landing trajectory. The trajectory of the glideslope and flare phase can be seen in Figure 5.1.

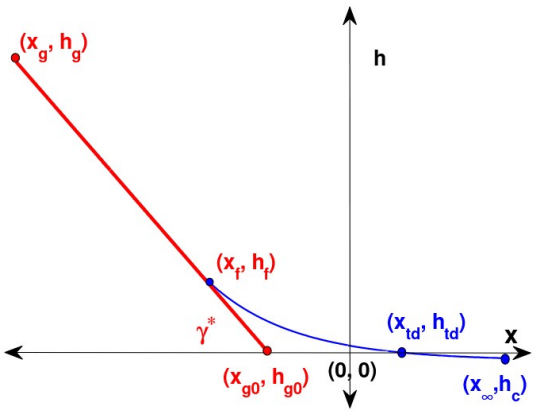


**Figure 5.1:** Landing path per Singh et al. [30]

A flight path angle equal to -3° during the glideslope phase is often used [14]. During flare, the desired altitude can follow a quadratic function in the current x coordinate related to the final x coordinate position at touchdown. This method for determining the desired height during the flare phase is also used by Steinleitner et al. whom have validated their INDI controller with a flight test of a tailwheel aircraft [8]. They include a method to avoid a renewed lift-off. First of all, the commanded height is kept constant as soon as the minimum of the quadratic function is reached (Figure 5.2). This results in a glide-out phase, during which the path inclination parallel to the runway must be maintained. The velocity is decreased, which

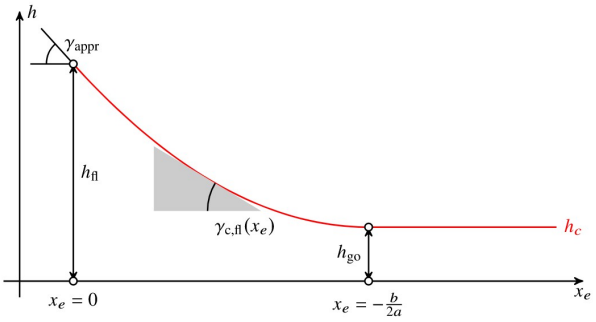


**Figure 5.2:** Flare path per Steinleitner et al. [8]

means the angle of attack increases to maintain altitude. The sink rate and glide path angle are then controlled using the thrust level. The velocity must be reduced sufficiently to avoid lift-off, and the elevator pushed upwards to its limit to create maximum down-force at the rear of the aircraft. Note that this is for a three-wheel aircraft with the goal of a three-point landing.

## 5.2. Curved Approach Path

If rather than a straight approach path a curved approach path is required, the approach phase becomes more important. Sedlmair et al. have developed an automatic landing controller using three-dimensional curved approach paths until touchdown [31]. Use is made of a nonlinear guidance law steering the aircraft along a predefined 3D spline path. The path is defined by $n$ waypoints, in geographic coordinates and are saved in the earth-centered earth-fixed coordinate system. These waypoints are then connected through cubic splines, consequently forming the path. The path is of continuous curvature and twice continuously differentiable, which is a necessity for the path to be flyable [31]. The guidance law calculates the acceleration needed to align the velocity vector $V$ with the line of sight $L$, steering the aircraft onto the predefined path. The acceleration command is computed by

$$a_{\text{cmd}} = \frac{2}{R^2}(V^K \times L_K) \times V^K = [0, a_{\text{h,cmd}}, a_{\text{h,cmd}}]^T. \tag{5.1}$$

where the superscript $K$ denotes a flight-path coordinate system transformation. The vertical acceleration component is transformed to a body-fixed load factor command, $n_{z,\text{cmd}} = \cos(\Phi) a_{\text{v,cmd}}/g$. Similarly, the horizontal acceleration is converted into a bank angle reference by $\Phi_{\text{cmd}} = \arctan(a_{\text{h,cmd}}/g)$. A reference for the heading is necessary in addition to the acceleration commands to implement the sideslip approach technique [31]. For a straight path approach, this would be the runway heading. For a curved approach however, a varying heading command makes more sense. To obtain the heading reference, the tangent direction at the nearest point N on the current spline segment $k$ of the path can be taken, see Figure 5.3.

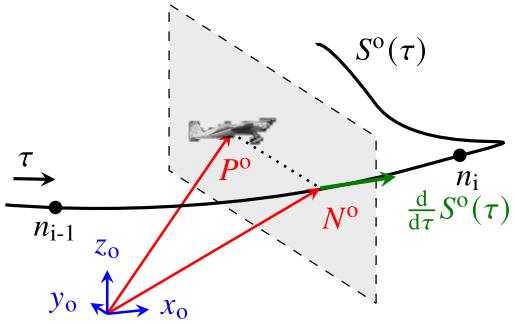


**Figure 5.3:** Heading reference determination for a curved path [31]

The nearest point on a given path is defined as the closest projection point and lies on the spline, denoted as $N = S_k(\tau_N)$, where $S_k(\tau)$ represents the spline at parameter $\tau$. For any point on the path, the tangent

vector is given by the derivative of the spline with respect to $\tau$, i.e., $\frac{d}{d\tau}S_k(\tau)$. The condition for the closest projection point is that the vector from the point $P_0$ to the spline point $S_k(\tau_N)$ is orthogonal to the tangent vector at that point. This condition can be written as:

$$(P_0 - S_k(\tau_N))^T \left.\frac{d}{d\tau}S_k(\tau)\right|_{\tau=\tau_N} = 0 \tag{5.2}$$

This equation ensures that the vector from $P_0$ to $S_k(\tau_N)$ is perpendicular to the tangent at $S_k(\tau_N)$, which is the closest projection point. By expanding and rearranging this condition, it forms a fifth-order polynomial, which can then be solved to find the value of $\tau_N$. Once $\tau_N$ is determined, the heading angle can be computed from the tangent vector at $\tau_N$ as $\left.\frac{d}{d\tau}S_k(\tau)\right|_{\tau=\tau_N}$.

## 5.3. Ground Effect

One of the difficulties of autoland is the existence of the ground effect. This effect is connected to two aerodynamic changes: a decreased induced drag and an effective air cushion. The induced drag decrease starts at about one wingspan above the ground since the ground disrupts the trailing wingtip vortices and limits the vertical component of the airflow around the wingtip, effectively lowering the strength of the downwash. In addition, the air is squeezed between the aircraft's belly and the ground at around $h = \frac{b}{4}$. Salahudden et al. include the ground effect by changing the wind model [14]. Prandtl's interference coefficient ($\sigma$) is computed when $h = b$, and subsequently used to compute a reduced aspect ratio, a lower angle of attack and a lower drag coefficient per Eq. (5.3).

$$\begin{aligned} \sigma &= e^{-2.48(\frac{2h}{b})^{0.768}} \\ A_G &= \left(\frac{AR}{1-\sigma}\right) \\ \Delta\alpha &= -\left(\frac{C_L}{\pi AR}\right)\sigma \\ \Delta C_D &= -\left(\frac{C_L^2}{\pi AR}\right)\sigma \end{aligned} \tag{5.3}$$

The ground effect induces a pitch down moment shortly before touchdown [31]. To compensate for this disturbance, a feedforward controller can be added. The mentioned pitching moment shall be continuously estimated and an additional elevator deflection issued to produce a compensating pitch-up moment, see Eq. (5.4).

$$\delta_{\text{e,fwd}} = (1 - \tanh(a_{\text{ge}} H_{\text{htp}}))\frac{C_{m,ge}}{C_{m,\delta_e}} \tag{5.4}$$

The activation function $(1 - \tanh(a_{\text{ge}} H_{\text{htp}}))$ is involved to ensure the feedforward controller is only active when the ground effect is present. $H_{\text{htp}}$ depends on the tailplane height and takes values between 0 and 1. $a_{\text{ge}}$ is a constant determined from flight test data, and influences the starting height where the ground effect model begins to take effects and develops when moving towards the ground.

# 6

# Controller Evaluation Metrics

After designing a controller, quantitative measures of its performance can be acquired. The design and performance of the control system are important for the overall stability and control of the aircraft, which are collectively referred to as the handling or flying qualities [32]. The evaluation can be done using evaluation metrics that provide quantitative measures of the system's behaviour. These metrics allow for the identification of potential areas for improvement and offer insight into the system's robustness, stability, and efficiency. The metrics discussed in this section are derived from simulation results and can be used in control system analysis. These include classical stability measures such as gain margin (GM) and phase margin (PM), as well as performance-oriented metrics being Root Mean Square (RMS) error and input, which quantify deviations in command tracking, disturbance rejection, and noise attenuation. By systematically evaluating these metrics and comparing them with the set requirements, one can determine how effectively the controller meets its design objectives and its response to external disturbances.

## 6.1. Performance Metrics

One can evaluate the overall performance of the controller using specific metrics extracted from simulations [22]. These evaluation metrics, shown in Table 6.1, then serve as the basis for a sensitivity analysis. By assessing how these metrics respond to variations in several aspects (i.e. gains, bandwidth, time delays), the system's sensitivity to parameter changes can be investigated. This helps to identify sensitive areas that quickly cause instability, which is useful for mitigation purposes. All categories except for the model uncertainty are copied from Lu et al. [22].

**Table 6.1:** Evaluation metrics [22]

| Category | Evaluation Metric | Description | Unit |
|---|---|---|---|
| Stability | GM | Gain Margin | dB |
| | PM | Phase Margin | $^\circ$ |
| | TDM | Time Delay Margin | s |
| Command tracking | RMSer | RMS error for tracking | $m$ |
| | RMSur | RMS input for tracking | $rad$ |
| Disturbance rejection | RMSed | RMS error due to disturbance | $m$ |
| | RMSud | RMS input due to disturbance | $rad$ |
| Noise attenuation | RMSen | RMS error due to noise | $m$ |
| | RMSun | RMS input due to noise | $rad$ |
| Model uncertainty | RMSen | RMS error due to model uncertainty | $m$ |
| | RMSun | RMS input due to model uncertainty | $rad$ |

## 6.2. Stability Metrics

Gain and phase margins are well-established concepts in linear system theory, providing a measure of a system's stability robustness [3]. The gain margin (GM) represents the factor by which the gain can be

increased before the system becomes unstable. In a typical case, it can be determined directly from the Bode plot by measuring the vertical distance between the $|KG(j\omega)|$ curve and the $|KG(j\omega)| = 1$ line at the frequency where the phase $\angle G(j\omega)$ reaches 180° [33].

The phase margin (PM) represents the amount by which the phase of $G(j\omega)$ exceeds -180° at the frequency where $|KG(j\omega)| = 1$. The GM and PM together demonstrate how close the complex quantity $G(j\omega)$ gets to the -1 point, indicating the system's proximity to instability. The stability margins can also be interpreted using the Nyquist plot. As shown in Figure 6.1, both GM and PM provide measures of how close the Nyquist plot approaches the aforementioned -1 point. Again, the GM indicates the maximum amount by which the system gain can be increased before the system becomes unstable. A positive phase margin indicates a stable system (so no encirclements of the Nyquist plot around the -1 point). Due to their widespread use in linear FCSs, they can also be applied to evaluate nonlinear controllers by referencing past values.

The time delay margins (TDMs) can be obtained both numerically and analytically, for example based on controller gain magnitudes and constrained state variable values [28]. If a closed-loop transfer function for the system including time delays is available, the maximum time delay before the system becomes unstable can be found analytically. Alternatively, the system response with different time delays can be simulated, and unstable situations reported (using the GM and PM), in that manner determining the TDM.

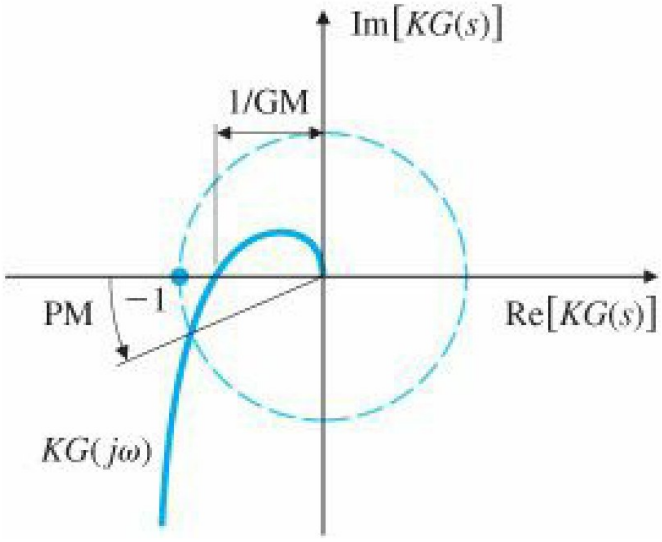


**Figure 6.1:** Nyquist plot for GM and PM definition [33]

## 6.3. Root Mean Square

The Root Mean Square (RMS) is a statistical measure that represents the effective magnitude of a varying signal. It is useful in the evaluation of a control system, as it provides a quantitative measure of deviations, control effort, and system performance under disturbances. RMS is defined mathematically as:

$$x_{rms} = \sqrt{\frac{\sum_{i=1}^{n} x_i^2}{n}} \tag{6.1}$$

where $x_i$ represents the individual data points (such as tracking errors or control inputs), and $n$ is the number of samples. In control system evaluation, RMS can among others be used for command tracking, disturbance rejection and noise attenuation, as shown in Table 6.1. All metrics containing the RMS are explained below.

- RMS Tracking Error: To measure command tracking performance, the deviations between the actual response and the reference signal are recorded at each sampling time. The RMS of these deviations

is then computed, providing an aggregate measure of the accuracy and consistency of the controller. A lower RMS tracking error indicates better command tracking performance.

- RMS Input: The RMS of the control input provides insight into the actuation effort required to achieve the desired performance. It quantifies the average magnitude of the control signal over time, helping to assess energy efficiency and actuator workload.
- Disturbance Rejection: To assess how well the controller compensates for external disturbances, the same RMS calculation is performed after introducing both horizontal and vertical wind gusts. This metric helps evaluate the system's robustness in maintaining stability and accurate tracking despite external influences.
- Noise Attenuation: The ability of a controller to suppress sensor noise can be evaluated by adding white noise to sensor measurements and computing the RMS tracking error and RMS input. A controller with strong noise attenuation properties will exhibit a low RMS error even in the presence of significant measurement noise.
- Model Uncertainty: To assess the robustness to model uncertainties of the controller, the same methodology can be applied after adapting the control effectiveness matrix, for example on purpose deviating by 10% of the actual model. A low RMS error means the controller is relatively robust against model uncertainty.

By analysing these RMS-based metrics, the performance and robustness of a control system can be evaluated.

# 7

# Aircraft Characteristics and Controller Requirements

This chapter presents the PH-LAB Cessna Citation aircraft characteristics and the performance requirements for the controller. This provides the foundation for designing and evaluating the autoland system that ensures safe and precise landings under realistic flight conditions.

## 7.1. PH-LAB Cessna Citation Characteristics

The PH-LAB Cessna Citation aircraft belongs to the Faculty of Aerospace Engineering of Delft University of Technology and is used for research purposes. The aircraft has been modified to serve as a multipurpose research platform, which resulted in the inclusion of a Flight Test Instrumentation System (FTIS) [34], Fly-By-Wire (FBW) system [35] and multiple sensor systems. The FBW system has been developed in-house and inherited all of the features and performance limitations of the original analog electric autopilot system. This results in limits on the pitch and roll rates of $+1/-1.5$ °/s and $\pm 10$ °/s during cruise flight respectively [7]. The servo loops use a proportional controller with servo-actuator positions as a feedback signal, such that the deflection angles of the control surfaces can be commanded directly. The relationship between this quantity and the deflection of the control surfaces does not have a one-to-one ratio. Actually, a reduction in control effectiveness of around $40$%, $60$% and $50$% is perceived for the aileron, elevator and rudder channel respectively.

The bias, noise, delay and sampling time characteristics of the aircraft were presented by van 't Veld [3]. The control surface deflections ($\delta_a, \delta_e, \delta_r$) are measured using a single synchro system for each type of control surface and transmitted to the FTIS as a group. The angular rates (p, q, r), attitude angles ($\phi, \theta$), and lateral acceleration ($n_y$) are measured by the Attitude and Heading Reference System (AHRS). The PH-LAB is equipped with two independent AHRS units, and the data is sent to the FTIS through an ARINC data bus. Additionally, true airspeed ($V_{TAS}$) is measured by two independent Digital Air Data Computers (DADCs), with the data also transmitted to the FTIS via the ARINC data bus. The measurement bias estimates of the angular rates, attitude angles and lateral accelerations are obtained using the difference between the mean of both AHRSs. The bias of the airspeed was recovered similarly by using the difference between the mean of both DADCs. Since only one synchro system was used during the flight test, the bias of the control surface deflections was determined based on the mean between two periods of straight flight. As the elevator settings for the two periods of straight flight differed, only the results of the aileron and rudder were included. The resulting characteristics are presented in Table 7.1 and Table 7.2.

**Table 7.1:** PH-LAB flight test data bias characteristics (Synchro) [3]

| Mean | 100-400s | 3660-3900s | Bias |
|---|---|---|---|
| $\delta_a$ [rad] | $-1.21 \cdot 10^{-2}$ | $-7.63 \cdot 10^{-3}$ | $4.42 \cdot 10^{-3}$ |
| $\delta_e$ [rad] | $1.07 \cdot 10^{-2}$ | $3.58 \cdot 10^{-2}$ | n.a. |
| $\delta_r$ [rad] | $-3.64 \cdot 10^{-2}$ | $-3.44 \cdot 10^{-2}$ | $2.02 \cdot 10^{-3}$ |

**Table 7.2:** PH-LAB flight test data bias characteristics (AHRS & DADC) [3]

| | 100 - 400 sec | | | 3660 - 3900 sec | | |
|---|---|---|---|---|---|---|
| Mean | AHRS1 | AHRS2 | Bias | AHRS1 | AHRS2 | Bias |
| $\phi$ [rad] | $-2.60 \cdot 10^{-4}$ | $1.26 \cdot 10^{-3}$ | $1.52 \cdot 10^{-3}$ | $1.02 \cdot 10^{-2}$ | $1.17 \cdot 10^{-2}$ | $1.51 \cdot 10^{-3}$ |
| $\theta$ [rad] | $5.98 \cdot 10^{-2}$ | $5.70 \cdot 10^{-2}$ | $2.86 \cdot 10^{-3}$ | $2.68 \cdot 10^{-2}$ | $2.30 \cdot 10^{-2}$ | $3.81 \cdot 10^{-3}$ |
| $p$ [rad/s] | $-1.67 \cdot 10^{-5}$ | $-4.06 \cdot 10^{-5}$ | $2.39 \cdot 10^{-5}$ | $5.28 \cdot 10^{-6}$ | $1.05 \cdot 10^{-6}$ | $4.22 \cdot 10^{-6}$ |
| $q$ [rad/s] | $5.53 \cdot 10^{-5}$ | $3.40 \cdot 10^{-5}$ | $2.13 \cdot 10^{-5}$ | $-3.89 \cdot 10^{-5}$ | $-6.94 \cdot 10^{-5}$ | $3.06 \cdot 10^{-5}$ |
| $r$ [rad/s] | $-6.35 \cdot 10^{-5}$ | $-5.96 \cdot 10^{-5}$ | $3.88 \cdot 10^{-6}$ | $7.26 \cdot 10^{-5}$ | $6.51 \cdot 10^{-5}$ | $7.46 \cdot 10^{-6}$ |
| $n_y$ [g] | $6.37 \cdot 10^{-4}$ | $-1.85 \cdot 10^{-3}$ | $2.49 \cdot 10^{-3}$ | $-9.11 \cdot 10^{-3}$ | $-1.12 \cdot 10^{-2}$ | $2.07 \cdot 10^{-3}$ |
| | DADC1 | DADC2 | Bias | DADC1 | DADC2 | Bias |
| $V_{TAS}$ [m/s] | 101.9 | 100.1 | 1.74 | 134.2 | 131.5 | 2.68 |

Sensor characteristics for the PH-LAB were also obtained by Grondman et al. following a signal analysis of flight data [7]. More recent research shows different data for the IMU, which indicate a higher sampling rate and lower delay [36]. These new values are added in brackets after the first ones. In addition, a frequency analysis showed that the airflow signals are affected by a 10 Hz disturbance, which is caused by the excitation of the eigenmodes of the air data boom during flight. The results are presented in Table 7.3

**Table 7.3:** Sensor characteristics PH-LAB [7] [36]

| Signal | Noise $(\sigma^2)$ | Bias | Resolution | Delay [ms] | Sampling Rate [Hz] |
|---|---|---|---|---|---|
| $p, q, r, \dot{\theta}, \dot{\phi}, \dot{\psi}$ [rad/s] | $4.0 \cdot 10^{-7}$ | $3.0 \cdot 10^{-5}$ | $6.8 \cdot 10^{-7}$ | 90 (15) | 52 (1000) |
| $\theta, \phi$ [rad] | $1.0 \cdot 10^{-9}$ | $4.0 \cdot 10^{-3}$ | $9.6 \cdot 10^{-7}$ | 90 | 52 |
| $f_x, f_y, f_z$ [g] | $1.5 \cdot 10^{-5}$ | $2.5 \cdot 10^{-3}$ | $1.2 \cdot 10^{-4}$ | 117 | 52 |
| $V_{TAS}, V_{CAS}$ [m/s] | $8.5 \cdot 10^{-4}$ | 2.5 | $3.2 \cdot 10^{-2}$ | 300 | $16,8$ |
| $h$ [m] | $4.5 \cdot 10^{-3}$ | $8.0 \cdot 10^{-3}$ | $3.0 \cdot 10^{-1}$ | 300 | 16 |
| $\dot{h}$ [m/s] | $5.5 \cdot 10^{-4}$ | $4.5 \cdot 10^{-2}$ | $8.1 \cdot 10^{-2}$ | 300 | 16 |
| $M$ [-] | $1.0 \cdot 10^{-8}$ | $7.0 \cdot 10^{-7}$ | $6.3 \cdot 10^{-5}$ | 300 | 8 |
| $\delta_a, \delta_e, \delta_r$ [rad] | $5.5 \cdot 10^{-7}$ | $2.4 \cdot 10^{-3}$ | - | $\sim 0$ | 100 |
| $\alpha_{\text{boom}}, \beta_{\text{boom}}$ [rad] | $7.5 \cdot 10^{-8}$ | $1.8 \cdot 10^{-3}$ | $9.6 \cdot 10^{-5}$ | 100 | 100 |
| $\alpha_{\text{body}}$ [rad] | $4.0 \cdot 10^{-10}$ | - | $1.0 \cdot 10^{-5}$ | 280 | 1000 |

All the values presented in this section are derived from real flight data and can be incorporated into the control system design to better reflect real-world conditions. This data also reassures the importance of including noise and bias, as mentioned in Section 4.2, since both are indeed present in the PH-LAB Cessna Citation.

## 7.2. Requirements

The development of an autoland controller based on the INDI method requires a set of performance and safety requirements. These requirements are used to ensure that the controller meets both operational and safety standards for aircraft landing operations. The purpose of this section is to define the key performance metrics and constraints that the INDI autoland controller must satisfy to ensure a safe and smooth landing process.

The requirements listed here will serve as a benchmark for evaluating the controller's performance across different flight conditions and in the presence of disturbances such as wind gusts, turbulence, or system failures. These metrics not only focus on the precision of the landing process but also account for the system's ability to maintain stability throughout the approach and touchdown phases. By meeting these requirements, the INDI autoland controller will be able to operate autonomously in a variety of real-world

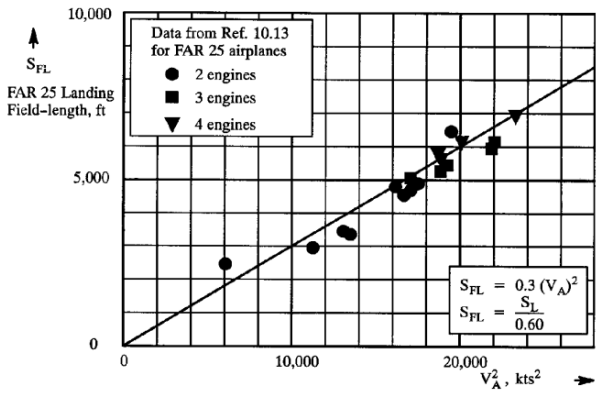


**Figure 7.1:** $V_A$ determination for known field length [39]

scenarios. The regular Cessna Citation II model has a Maximum Takeoff Weight (MTOW) of 15100 lb (or 6849 kg) [37]. Assuming the PH-LAB Cessna Citation is not significantly less heavy such that it falls below the 5670 kg limit, it falls under CS-25 regulations [38]. However, from CS25.20.b1 it is stated that "In the absence of an appropriate investigation of operational implications these requirements do not necessarily cover automatic landings." [38]. Still, the requirements from this guidebook will be looked into for inspiration and relevance.

### 7.2.1. Velocity Requirements

During the approach, assuming a straight line flight path, the approach speed must satisfy $V_A \geq 1.3V_{S_{approach}} = 1.3\frac{2(W_L/S)}{\rho C_{L_{max_{approach}}}}$ or from Figure 7.1 if the field length is known until the airplane reaches the screen height [39]. This screen height is equal to 50 ft (15.24 m). After this, a transition is started until touchdown, with speed $V_{TD}$. During the final approach, the aircraft must be in landing configuration. Although the touchdown speed is not specified in the FARs, it is often approximated by $V_{TD} = 1.15V_{S_{approach}}$. Using this touchdown speed and the flight path angle, the sink rate can be determined using:

$$V_{sink} = V_{TD} \sin(\gamma) \tag{7.1}$$

Sink rates at touchdown greater than 10 ft/s are considered to cause damage to the aircraft and are classified as hard landings for general aviation [39] [38]. In general, a sink rate at touchdown between 1 ft/s and 6 ft/s is considered acceptable for a smooth landing [40]. Furthermore, the flare speed $V_{FL}$ can be assumed to be $V_{FL} \approx 0.95V_A$. From this, the following requirements are set for velocities:

**Table 7.4:** Velocity Requirements

| Requirement | Description |
|---|---|
| REQ-V-1 | The approach velocity shall be $V_A \geq 1.3V_{S_{approach}}$ |
| REQ-V-2 | The maximum flare velocity shall be $V_{FL} \approx 0.95V_A$ |
| REQ-V-3 | The maximum touchdown velocity shall be $V_{TD} = 1.15V_{S_{approach}}$ |
| REQ-V-4 | The maximum sink rate is 10 ft/s but the desirable sink rate shall lie in the range of 1 to 6 ft/s |
| REQ-V-5 | The load factor shall lie in the range of 0.8-1.2 |

### 7.2.2. Flight Path and Trajectory

For an autoland system, visual flight rules (VFR) do not apply. Instead, the procedure shall be conducted under Instrument Flight Rules (IFR). An IFR approach can be nonprecision (only lateral guidance) or precision (both lateral and vertical guidance). According to ICAO Standards, the flare command must be given at an altitude of around 50 ft to 60 ft [41]. The actual flare then begins at around 30-40 ft. The IFR landing procedure is shown in Figure 7.2. One of the main factors in the flight trajectory is the flight path

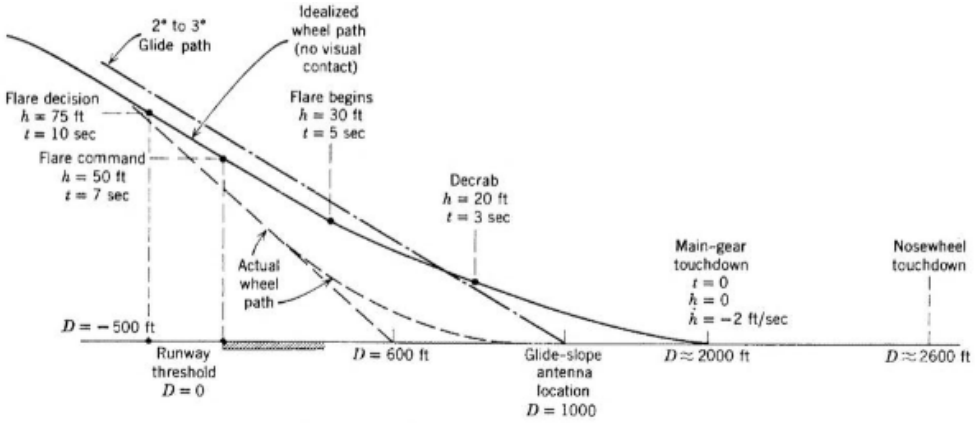


**Figure 7.2:** IFR landing of a jet aircraft [41]

angle $\gamma$. A glide path angle of 2°-3° is assumed to be achievable during the approach phase. The flare path depends on the chosen method as described in Chapter 5, from which a flight path angle will follow. This angle determines the sink rate (see Eq. (7.1)), for which requirements already exist (Table 7.4). Hence, only a soft requirement on the flight path angle during approach will be set. Regarding the longitudinal position from the runway threshold (where the flare command starts) and lateral position from the runway's center line at touchdown, some acceptable ranges are provided in Figure 7.3 [41]. Furthermore, it is preferable to stay within $\pm 1.5°$ of the runway's centerline during the final approach for a stable, safe approach. This leads to the flight path and trajectory requirements shown in Table 7.5

| Variable | Limits (95%) | Reason for Limits |
|---|---|---|
| Longitudinal position from threshold (ft) | 800–2300 | Touchdown on runway with adequate braking distance |
| Airspeed (kts) | 110–145 | Lower limit to maintain control; upper to limit braking effort |
| Lateral position from runway's center line (ft) | ±27 | Touchdown with main gear more than 5 ft from runway edge |
| Lateral velocity (ft/sec) | ±8 | Limit risk of leaving runway after touchdown |
| Sink rate (ft/sec) | 0–5 | Limit landing gear/tire damage |
| Pitch attitude (degrees) | 0–5 | Limit risk of a noise-wheel landing or tail drag |
| Roll attitude (degrees) | ±5 | Limit risk of damage to wing tips or engine nacelles |

**Figure 7.3:** Acceptable range of variables at touchdown for jet transport aircraft [41]

**Table 7.5:** Flight path and trajectory requirements

| Requirement | Description |
|---|---|
| REQ-FP-1 | The flare command must be given at an altitude between 50 ft and 60 ft |
| REQ-FP-2 | The actual flare shall begin at an altitude between 30 ft and 40 ft |
| REQ-FP-3 | The flight path angle during approach shall lie between 2° and 3° |
| REQ-FP-4 | The lateral position shall be within $\pm 1.5°$ of the runway's centerline during the final approach phase |
| REQ-FP-5 | At touchdown, the longitudinal position from the threshold shall lie between 800 ft and 2300 ft |
| REQ-FP-6 | At touchdown, the lateral position from the runway's centerline shall be within $\pm 27$ ft |

### 7.2.3. Actuator and Attitude Limits

Since the aircraft used for this research does exist in real life, the actuator limits are known as well. These limits must be respected to ensure a safe landing and prevent structural damage. The aileron deflection must lie within -19° to 15°, the elevator deflection within -17° to 15° and the rudder deflection within $\pm 22°$. Moreover, all actuators have an absolute maximum rate limit of 19.7°/s [7]. This results in the following set of requirements:

**Table 7.6:** Actuator and attitude requirements

| Requirement | Description |
|---|---|
| REQ-PL-1 | The aileron deflection shall remain in the range of $-19° \leq \delta_a \leq 15°$ |
| REQ-PL-2 | The elevator deflection shall remain in the range of -17° $\leq \delta_e \leq 15°$ |
| REQ-PL-3 | The rudder deflection shall remain in the range of -22° $\leq \delta_r \leq 22°$ |
| REQ-PL-4 | All actuator rates shall be smaller than 19.7°/s |

### 7.2.4. All Requirements

The final list of requirements can be observed in Table 7.7. This list will be used to evaluate the control system, next to inherent requirements such as maintaining stability and staying within the operational limits of the aircraft. Since this research is about the design of a controller, not all aircraft-related requirements are considered a part of the scope. Furthermore, a final column is created to show the origin of the requirement. The origins are Roskam et al., Siegel et al., Kayton et al. and Grondman et al. respectively [39] [40] [41] [7].

**Table 7.7:** List of requirements

| Requirement | Description | Origin |
|---|---|---|
| REQ-V-1 | The approach velocity shall be $V_{\mathrm{A}} \geq 1.3 V_{\mathrm{S_{approach}}}$ | Roskam |
| REQ-V-2 | The maximum flare velocity shall be $V_{\mathrm{FL}} \approx 0.95 V_{\mathrm{A}}$ | Roskam |
| REQ-V-3 | The maximum touchdown velocity shall be $V_{\mathrm{TD}} = 1.15 V_{\mathrm{S_{approach}}}$ | Roskam |
| REQ-V-4 | The maximum sink rate is 10 ft/s but the desirable sink rate shall lie in the range of 1 to 6 ft/s | Siegel |
| REQ-V-5 | The load factor shall lie in the range of 0.8-1.2 | Roskam |
| REQ-FP-1 | The flare command must be given at an altitude between 50 ft and 60 ft | Kayton (ICAO) |
| REQ-FP-2 | The actual flare shall begin at an altitude between 30 ft and 40 ft | Kayton |
| REQ-FP-3 | The flight path angle during approach shall lie between -2° and -3° | Kayton |
| REQ-FP-4 | The lateral position shall be within $\pm 1.5°$ of the runway's centerline during the final approach phase | Kayton |
| REQ-FP-5 | At touchdown, the longitudinal position from the threshold shall lie between 800 ft and 2300 ft | Kayton |
| REQ-FP-6 | At touchdown, the lateral position from the runway's centerline shall be within $\pm 27$ ft | Kayton |
| REQ-PL-1 | The aileron deflection shall remain in the range of $-19° \leq \delta_a \leq 15°$ | Grondman |
| REQ-PL-2 | The elevator deflection shall remain in the range of -17° $\leq \delta_e \leq 15°$ | Grondman |
| REQ-PL-3 | The rudder deflection shall remain in the range of -22° $\leq \delta_r \leq 22°$ | Grondman |
| REQ-PL-4 | All actuator rates shall be smaller than 19.7°/s | Grondman |

# Part III

## Additional Results

# 8

# Fusion Filter Design

As explained, the IMU based altitude computation is prone to cumulative errors. Sensor fusion can mitigate these effects by combining the DADC measurement with the IMU based computation, thereby increasing robustness and accuracy. Two fusion methods were investigated: a complementary filter and a Kalman filter. Both were tuned, evaluated, and compared in order to select the most suitable approach.

## 8.1. Complementary Filter

In addition to the Kalman filter, a complementary filter was considered. The error between the DADC sensor measurement and the IMU-based altitude computation can be expressed by:

$$\hat{e}_h = \hat{h} - h_s \tag{8.1}$$

Where $h_s$ is the sensor measurement and $\hat{h}$ the IMU-based altitude computation. This represents the difference between two altitude estimates rather than the true error.$\hat{e}_h > 0$ indicates that the IMU estimate is higher, which requires a negative correction, while $\hat{e}_h < 0$ works the other way around. A controller with a negative gain can be used to decrease $\hat{e}_h$ and still use $\hat{h}$ by having:

$$h_{fb} = \hat{h} + P\hat{e}_h \tag{8.2}$$

With $h_{fb}$ the altitude that is fed back to the outer control loop and $P$ the negative gain. The gain determines the balance between reliance on the IMU estimate and the DADC measurement. A block diagram of the complementary filter is shown in Figure 8.1.

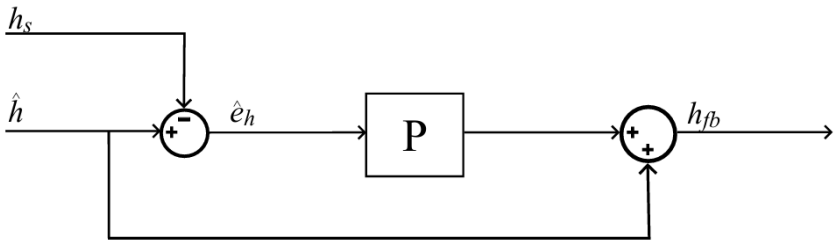


**Figure 8.1:** Altitude feedback complementary filter block diagram

## 8.2. Tuning

Both filters require tuning based on performance metrics and error characteristics. The complementary filter tuning refers to the gain $P$, while the Kalman filter tuning refers to $R_k$ and $Q_k$. Turbulence was included in the simulations to evaluate robustness.

### 8.2.1. Setup

Since a simulation environment is used, the ”actual” altitude without delay is known at all times. The error between this altitude and the filter output ($e_{fb} = h - h_{fb}$) is compared with the error experienced with the

DADC measurement ($e_s$). The latter error serves as a reference for an acceptable error, as this is the error experienced in regular situations. These errors are computed during the approach and flare phase, and the maximum absolute value is saved. As the flare phase requires more accuracy than the approach phase, a larger error with the actual altitude is deemed acceptable during the approach phase. The metrics included:

- **RMSer$_{act}$**: RMS($h$-$h_{ref}$)
- **RMSer$_{con}$**: RMS($h_{ref} - h_{fb}$)
- **Control effort**: variance and RMS of elevator deflection
- **Load factor deviation**
- **Final sink rate**
- **Maximum errors**: during approach (Max $e_{app}$), flare (Max $e_{flare}$) and touchdown (Max $e_{final}$) of the filter relative to the actual altitude

### 8.2.2. Kalman Filter Tuning

Tuning showed that $Q_k$ strongly influenced performance, while $R_k$ had a smaller effect. Therefore, the tuning was focused on small steps of $Q_k$ and larger steps of $R_k$. A similar analysis as for the controller's gain tuning was performed, where several performance metric plots are used for comparison. Several of these plots are shown in Figure 8.2. The Kalman set index refers to sets of $R_k$ and $Q_k$ which can be

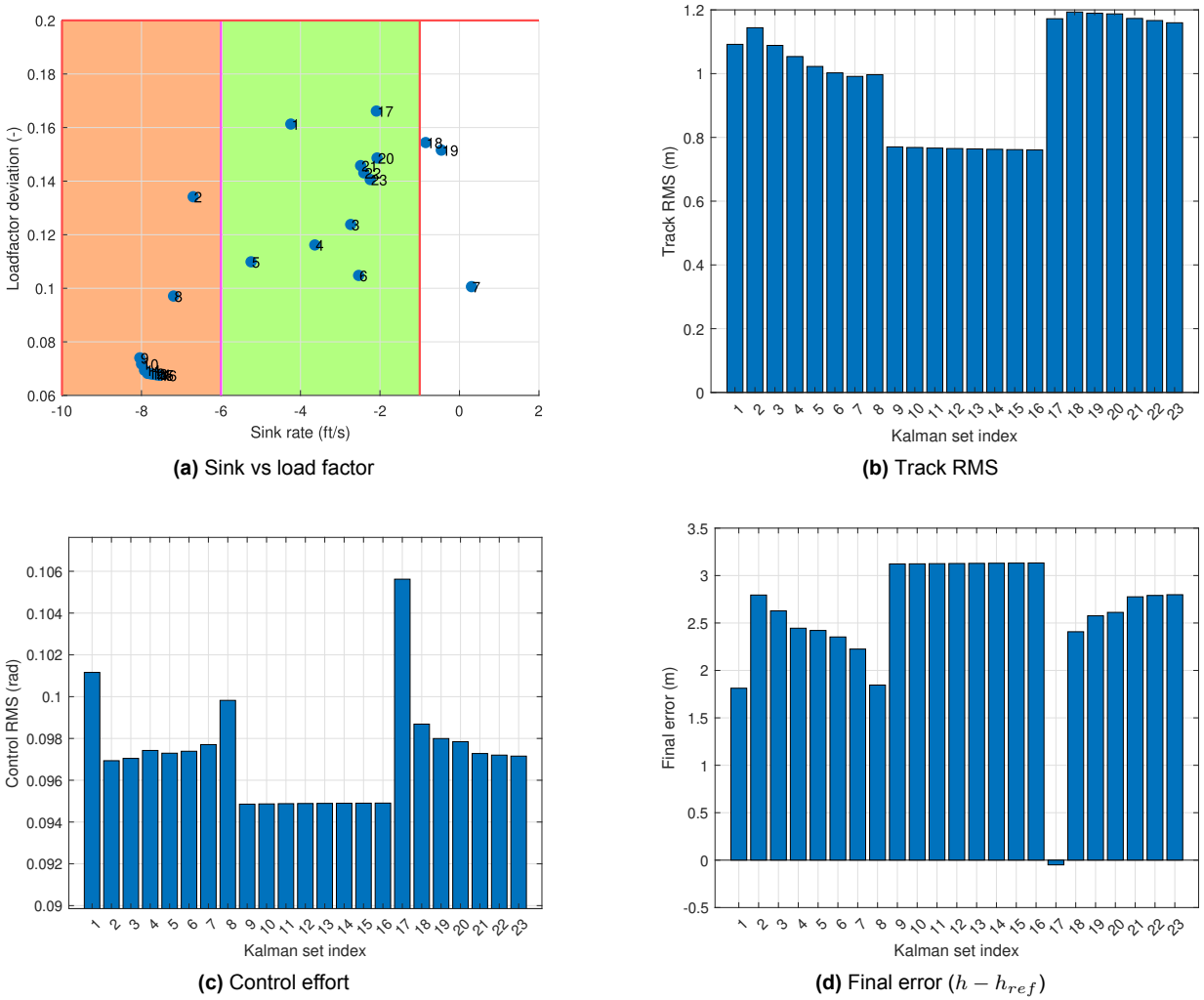


**(a)** Sink vs load factor

**(b)** Track RMS

**(c)** Control effort

**(d)** Final error ($h - h_{ref}$)

**Figure 8.2:** Kalman filter gain tuning

described by the mathematical expression below.

$$(Q_k, R_k) \in \left\{Q_k^{(1)},\ Q_k^{(2)},\ Q_k^{(3)}\right\} \times \{0, 2, 4, 6, 8, 10, 12, 14\}, \tag{8.3}$$

where

$$Q_k \in \left\{\text{diag}(10^{-5},\ 10^{-4},\ 10^{-7}),\ \ 0,\ \ \text{diag}(10^{-4},\ 10^{-3},\ 6.25 \times 10^{-6})\right\}.$$

A few conclusions can be drawn from these plots. First of all, a lower $Q_k$ gives the best results for all metrics. Second of all, with a $Q_k$ of 0, results are not dependent on $R_k$. This indicates that $R_k$ is not used, resulting in larger errors at touchdown, see Figure 8.2d. Sets 7, 18 and 19 do not comply with the sink rate requirement, while sets 2 and 8-18 are above the desired sink rate. All sets comply with the load factor deviation requirement. Interestingly, a higher $R_k$ gives better results on the final error for the first $Q_k$, but worse results for the third $Q_k$. The control effort and the tracking error decrease when increasing $R_k$. All in all, this analysis has led to the choice of set 6 because of its low load factor deviation, desirable final sink rate and low control effort, which gives $Q_k = \text{diag}([1e-5, 1e-4, 1e-7]), R_k = 10$.

### 8.2.3. Complementary Filter Tuning

The tuning of the complementary filter was done following the same procedure as the Kalman filter. Increasing the magnitude of the proportional gain $P$ enhances the influence of the DADC output, with $P = 0$ corresponding to the pure estimate. The DADC's main contribution lies in its compensation of the cumulative integration error present in the altitude estimate. The complementary filter gain $P$ was tuned between -0.1 and -0.9. Some of the relevant results are shown in Figure 8.3. Control effort decreases

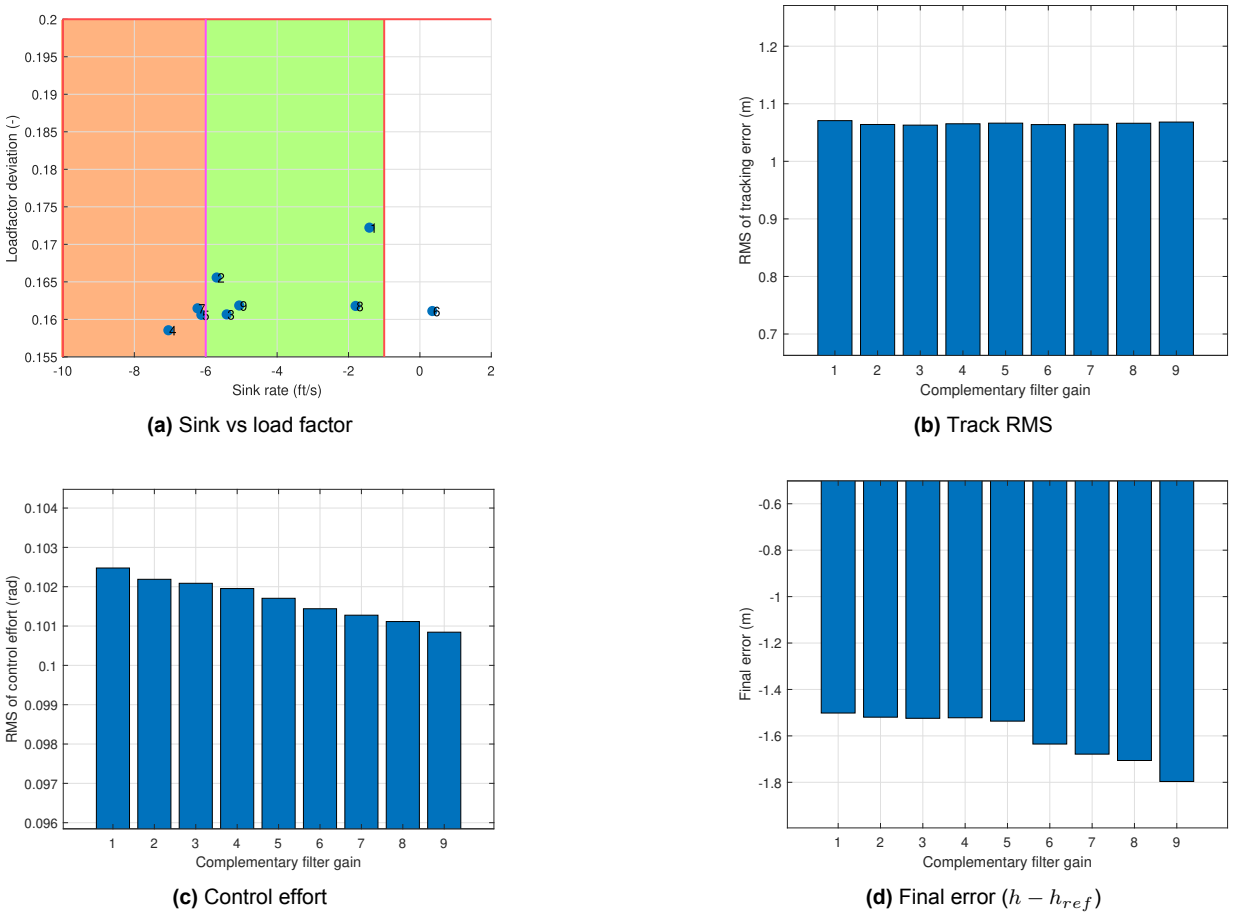


**(a)** Sink vs load factor

**(b)** Track RMS

**(c)** Control effort

**(d)** Final error ($h - h_{ref}$)

**Figure 8.3:** Complementary filter gain tuning

slightly with larger gains. The metrics that are most affected are the maximum load factor deviation, the final sink rate, and the final error. The final error's magnitude increases along with the gain, which is

consistent with earlier findings. A gain of -0.6 results in a sink rate outside the allowed range (Figure 8.3a), while -0.4, -0.5 and -0.7 lie outside the desired range, although slightly. A gain of $P = -0.3$ was selected, offering a good balance between accuracy, desirable sink rate, and low load factor deviation.

## 8.3. Final Filter Selection

After tuning the Kalman filter and complementary filter, a tradeoff was conducted using the same set of performance metrics applied during their tuning phase, along with the errors relative to the actual signal at different instances. Table 8.1 summarises the results for the chosen configuration of each filter. The

**Table 8.1:** Comparison of best-performing Kalman and complementary filter configurations

| Filter | $RMSer_{act}$ | $RMSer_{con}$ | RMSur | VARur | Min/Max n | Sink | Max $e_{app}$ | Max $e_{flare}$ | Max $e_{final}$ |
|---|---|---|---|---|---|---|---|---|---|
| Kalman | 1.75 | 1.00 | 9.74e-02 | 4.45e-04 | 0.90 | -2.54 | -2.36 | -0.95 | -0.33 |
| Compl. | 1.18 | 1.06 | 1.02e-01 | 1.06e-03 | 0.84 | -5.41 | -0.91 | 0.73 | 0.32 |

Kalman filter achieved lower control effort and reduced variance, leading to smoother actuator behaviour and tracking. It also yields a smaller minimum load factor, which contributes to safer and more comfortable flight dynamics. The complementary filter demonstrates an advantage in terms of altitude accuracy, particularly during the approach phase. During the approach phase, the Kalman filter is less accurate relative to the actual altitude, resulting in a larger $RMSer_{act}$ and Max $e_{app}$. During the flare phase, the maximum error is 0.2 m higher in magnitude than the complementary filter, and the final error is equal but opposite in sign. The fact that the complementary filter records an opposite sign is surprising, as this means that the fed back altitude is lower than the actual altitude. This could be dangerous if the magnitude were larger, as the system would think it had touched down before it actually did.

To further evaluate the quality of the filters, the errors are compared to the DADC measurement error. The DADC records a mean error of $\approx 0.85 - 0.90$ m, the Kalman filter error lies in the same range, and the complementary filter yields a mean error of only $\approx 0.30$ m. This means that the Kalman filter provides a situation very similar to that when using the DADC measurement, and the complementary filter improves accuracy. The error relative to the actual altitude can be observed in Figure 8.4b. The Kalman filter's error spikes in the beginning, but reduces towards the end. The complementary filter's error is very consistent.

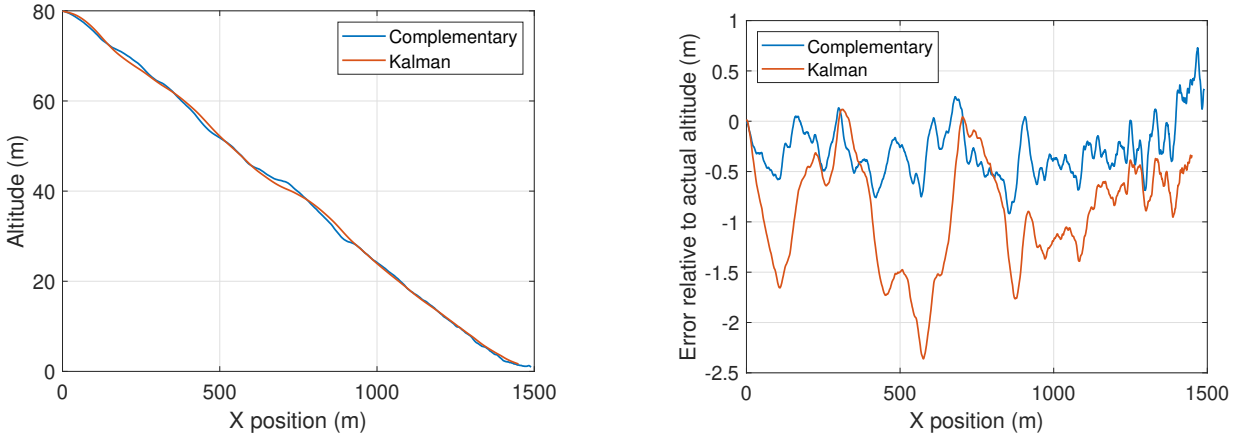


**(a)** Altitude computation

**(b)** Error relative to the actual altitude

**Figure 8.4:** Performance comparison of the Kalman and complementary filter

In conclusion, the analysis suggests that the Kalman filter offers the most balanced option. While its accuracy is slightly lower than that of the complementary filter, the smoother control effort, reduced load factor deviations, and stable behaviour during flare and touchdown make it the more reliable choice. The complementary filter remains an interesting alternative in situations where maximum accuracy is prioritised over stability, but for the purpose of this study the Kalman filter is the preferred method.

# 9

# Verification & Validation

An important aspect of control system development is the process of verification and validation (V&V). In this work, these steps are applied both at the level of the aircraft model and the control system components. Verification ensures that the model and controller behave as intended, for example by applying test inputs and checking for logical, stable responses. Validation, in the absence of real flight data, is performed by comparing simulated responses to those that are theoretically or qualitatively expected from real aircraft behaviour (mostly flight dynamics) and to the simulation results of Pollack et al., who studied the same aircraft under different flight conditions [42]. This section outlines the procedures used to perform verification and validation in this simulation context.

## 9.1. Aircraft Model

Prior to using the simulation model for the Cessna Citation II PH-LAB aircraft, the model must be verified and validated to ensure correct functioning. This process is carried out in steady horizontal flight by applying pulse inputs to individual actuators and analysing the model's responses. In the model, angles are expressed in radians, rates in rad/s and velocities in m/s. A positive elevator pulse input produces a negative pitch rate response, consistent with the expected negative control derivative (negative $C_{m_{\delta_e}}$). The correct functioning of the throttle was verified by applying a 10% increase, which resulted in the expected velocity increase. The results are shown in Figure 9.1.

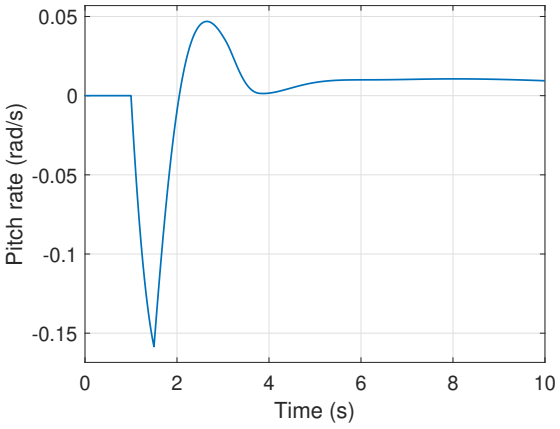


**(a)** Pitch rate response to elevator pulse after 1 second

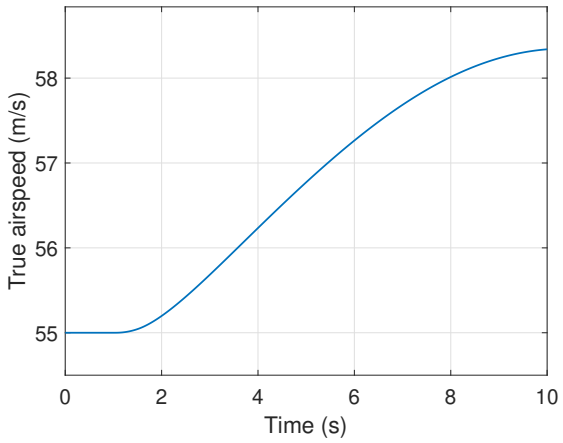


**(b)** Velocity response to 10% throttle step input after 1 second

**Figure 9.1:** Pitch rate and velocity V&V

To verify the lateral direction dynamics, positive pulse inputs were applied to the rudder and aileron. The corresponding roll and yaw rate responses are shown in Figure 9.2. A rudder pulse results in a negative yaw rate, revealing a negative $C_{n_{\delta_r}}$. The associated role rate response reflects the dihedral effect. Similarly, the aileron deflection yields a negative roll rate such that $C_{l_{\delta_a}} < 0$. This is accompanied by adverse yaw.

These effects confirm that the cross-coupling between lateral and directional dynamics is represented correctly.

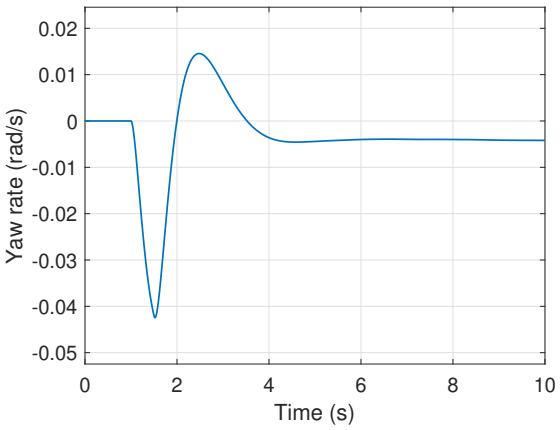


**(a)** Yaw rate response to $\delta_r = 5°$ pulse

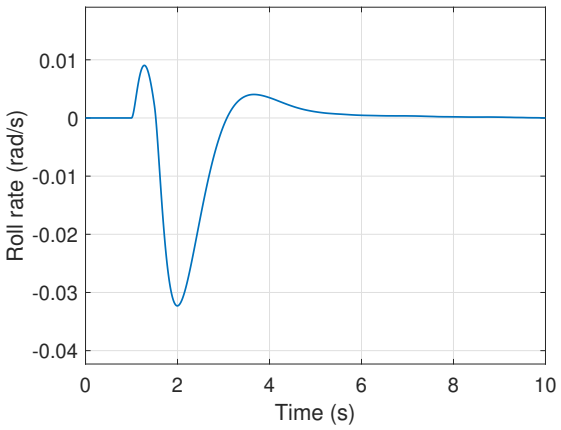


**(b)** Roll rate response to $\delta_r = 5°$ pulse

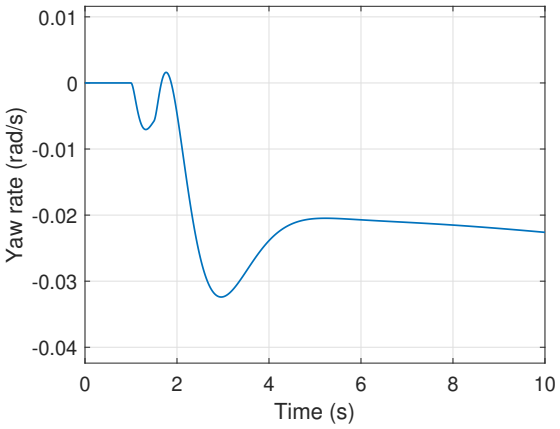


**(c)** Yaw rate response to $\delta_a = 5°$ pulse

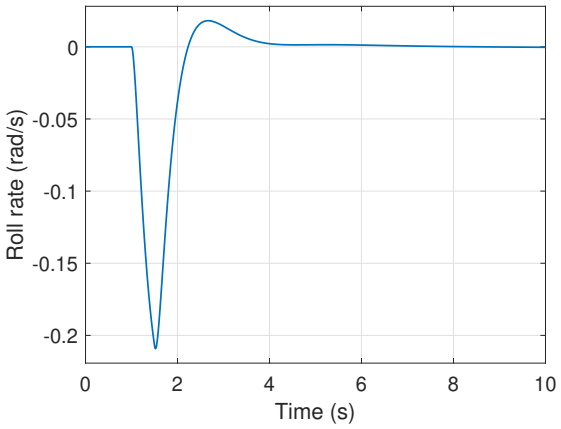


**(d)** Roll rate response to $\delta_a = 5°$ pulse

**Figure 9.2:** Roll and yaw rate responses to positive rudder ($\delta_r$) and aileron ($\delta_a$) pulse inputs

Although no flight data is available for validation, the model's response is consistent with theoretical expectations for aircraft dynamics, including coupling phenomena. This provides sufficient verification of the model's correct functioning, ensuring its suitable for the purposes of this study.

## 9.2. INDI Controller

Next to the aircraft model, the controller must be verified and, if possible, validated. The evaluation is conducted in two steps. First, the basic functioning of the controller is verified by analysing control surface deflections, body rates, and correct movement, after following a predefined path. Second, the controller's behaviour is compared with results from an INDI study on the same aircraft, which serves as an external reference.

### 9.2.1. Trajectory Tracking

The V&V of the INDI controller is performed using a simulated reference scenario in which the controller is tasked with following the predefined flight path. By analysing the resulting trajectory, control surface deflections, and body rates, the controller's ability to stabilise and guide the aircraft as intended is assessed. Results are shown here for the base case without delays, sensor noise, biases, or turbulence (Figure 9.3), although the same procedure was applied throughout the development process.

The aircraft's horizontal movement progresses in almost linear fashion (Figure 9.3b), while roll and yaw rates/angles remain negligible as expected. The pitch rate and elevator deflection show a transient

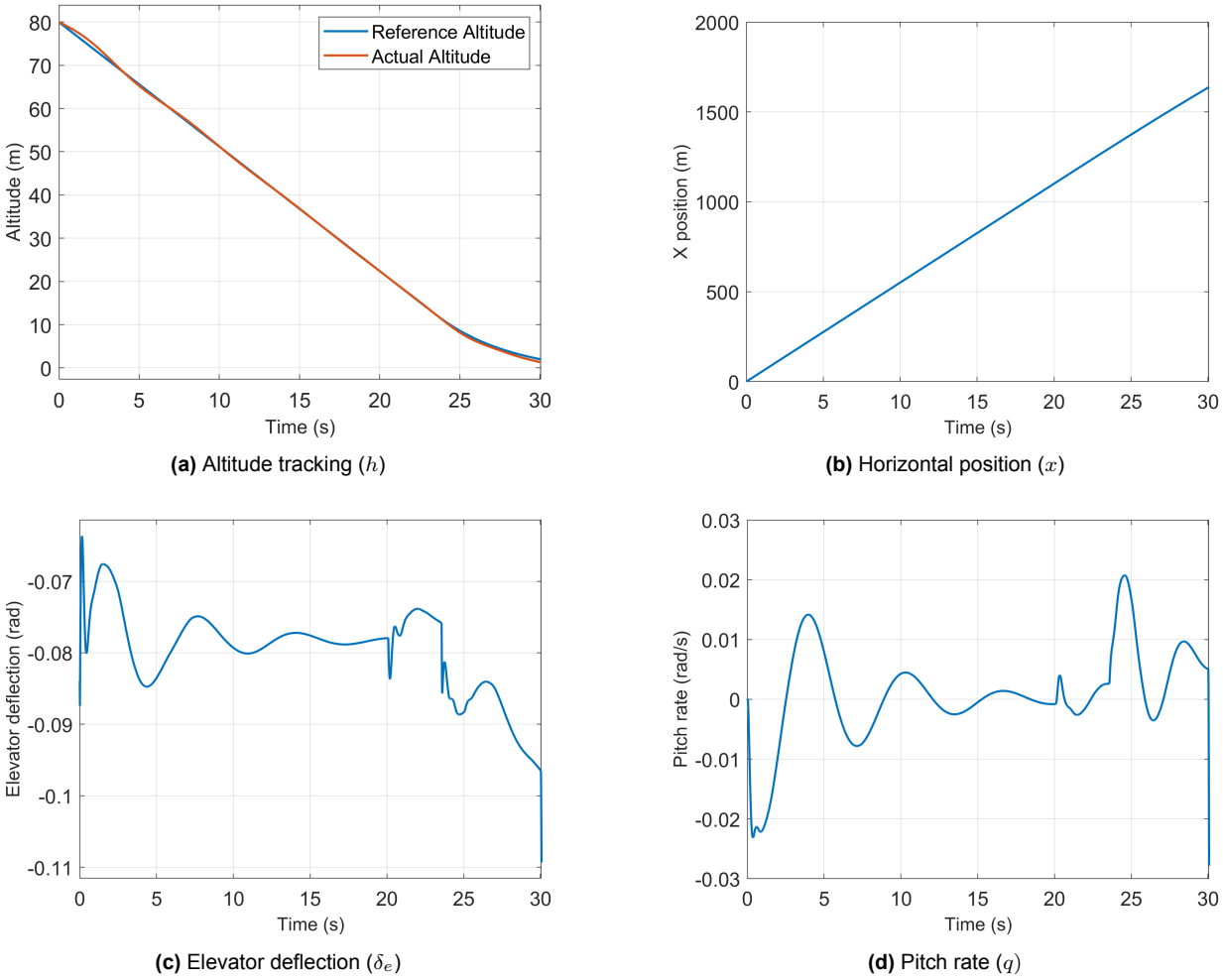


**(a)** Altitude tracking ($h$)

**(b)** Horizontal position ($x$)

**(c)** Elevator deflection ($\delta_e$)

**(d)** Pitch rate ($q$)

**Figure 9.3:** V&V of the INDI controller for trajectory tracking

response as the controller corrects the mismatch between the trimmed -2° flight path angle and the commanded -3°. After an adjustment, the elevator deflection settles into a new equilibrium, demonstrating the controller's capability to stabilise around a new operating point. After about 20 seconds, the start of the flare manoeuvre becomes visible, recognisable by the deviation from the previously stabilised elevator deflection. The initial jump can be attributed to the change from the approach phase gains to the flare-specific ones.

### 9.2.2. Similar Study

Further verification was performed using simulation data from Pollack et al., who investigated the same aircraft under steady, straight flight conditions [42]. The aircraft was trimmed to an altitude of 3600 m at 100 m/s in clean configuration, and subjected to a commanded pitch-up rate of $0.8°/s$ over 8 seconds, matching the conditions in this present study. The model response was compared directly with the data reported by Pollack, and is shown in Figure 9.4. The pitch angle increases by slightly more than 6° in both cases (Figure 9.4b), indicating that the overall motion of the aircraft is similar. The pitch rate response in this study shows a small undershoot and negligible overshoot (Figure 9.4a). In contrast, Pollack reports more overshoot and oscillatory behaviour, which can be attributed to some of their assumptions made when deriving the control law [42]. The elevator deflection difference required in the present model is somewhat larger in magnitude but follows a similar path (Figure 9.4c). Overall, the responses are consistent in both magnitude and structure, which supports the fidelity of the implemented controller.

It should be noted that Pollack performed some actual flight tests, but under different commanded paths. Although this prevents a direct validation, the similar responses of the two simulation studies together with

Pollack's flight test confirmation strengthen confidence in the model behaviour.

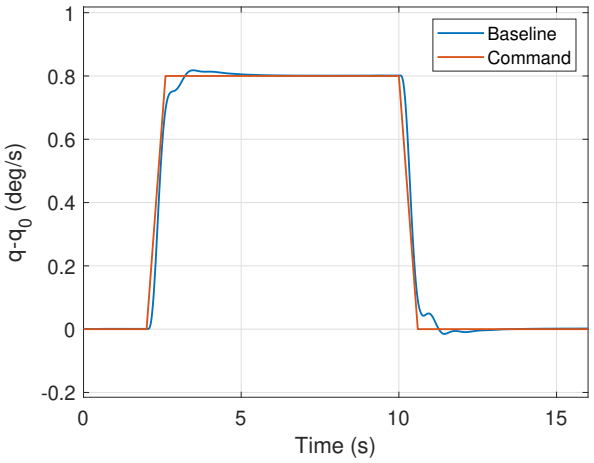


**(a)** Pitch rate tracking ($q$)

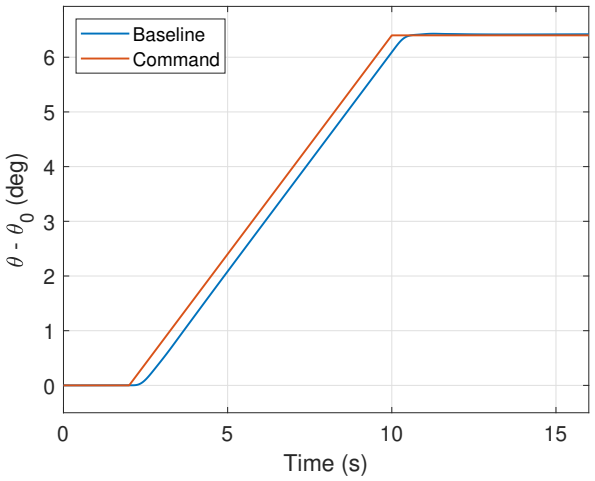


**(b)** Pitch angle ($\theta$)

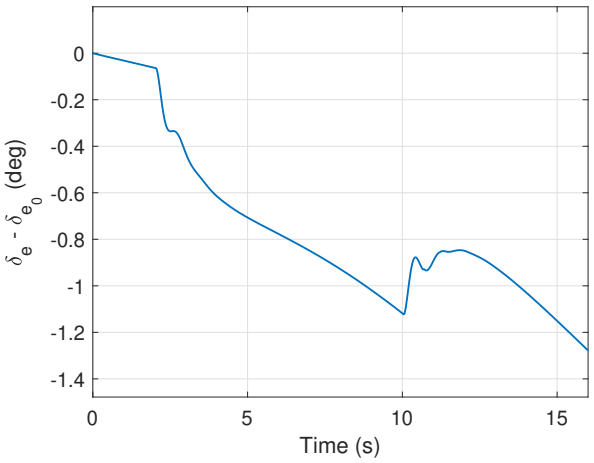


**(c)** Elevator deflection ($\delta_e$)

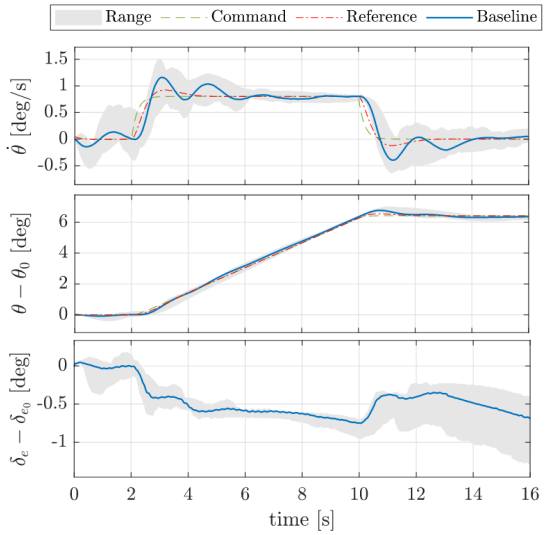


**(d)** Pollack et al. response to pitch-up manoeuvre [42]

**Figure 9.4:** Responses to a pitch-up manoeuvre of 0.8 deg/s for 8 seconds in trimmed, steady, horizontal flight.

# 10

# Performance Evaluation

To evaluate the controller's performance, the effects of factors such as turbulence, delays, noise, bias, and model uncertainty are examined. Although these aspects are part of the controller during the design phase, this analysis isolates their individual impact on the overall performance.

## 10.1. Real-World Factors

Turbulence is computed using the discrete Dryden Wind Turbulence Model to evaluate the disturbance rejection capabilities. The used block parameters can be found in Table 10.1 and represent light to moderate turbulence [43]. The atmospheric turbulence is generated by filtering white noise to produce wind disturbances that match the desired velocity spectral characteristics defined by the Dryden model. Since only longitudinal motion is of interest, lateral turbulence is neglected. Note that the intensity refers to the low altitude intensity at 6 m.

**Table 10.1:** Block parameters for Dryden model

| Parameter | Intensity | Wind direction | Turbulence level | Scale length | Wingspan | Sample time |
|---|---|---|---|---|---|---|
| Value | 10 (m/s) | 0 (°) | Moderate (-) | 260 (m) | 13.325 (m) | 0.01 (s) |

Next to its disturbance rejection capability, INDI control is inherently robust to model uncertainties. While accurate knowledge of the control effectiveness may improve performance, INDI does not require it to be exact. To demonstrate this robustness in simulation, one can intentionally introduce an error in the control effectiveness matrix used in the incremental step, while the aircraft model remains unchanged.

Because INDI relies heavily on sensor feedback, sensor quality is considered. Noise and bias are added to the signals according to the characteristics listed in Table 7.3. In addition, these feedback signals are not instantaneous and experience some delays as explained in Section 4.1. To demonstrate the influence of these delays, the performance of an "Ideal" controller without such delays is shown. The "Realistic" controller contains the sensor delays as shown in Table 7.3. The updated IMU delays are used and rounded up to 20 ms, the dynamic pressure is assumed to experience the same delay as $V_{TAS}$ (300 ms). Furthermore, the actuator dynamics are included and can be described by a first-order transfer function:

$$A(s) = \frac{13}{s + 13} \tag{10.1}$$

**Table 10.2:** Controller configurations

| Controller | Actuator dynamics | Actuator pure time delay | Sensor pure time delay |
|---|---|---|---|
| Ideal | Yes | No | No |
| Realistic | Yes | Yes | Yes |

In addition to this, a pure time delay of 40 ms is added for the realistic controller [7]. Table 10.2 gives an overview of the two controller configurations.

## 10.2. Performance under Real-World Effects

To account for real-world effects individually, performance metrics inspired by Table 6.1 are used. Each category is assessed under the ”Ideal” and ”Realistic” configuration.

Table 10.3 summarises the results. For command tracking, delays increase the RMS error from 0.40 m to 0.57 m in the default case, yet the maximum load factor deviation and final sink rate remain within acceptable limits. Across all configurations and categories, including delays does not increase control effort, which remains relatively constant. This indicates that the controller effectively corrects deviations from the reference path without requiring excessive control commands, as also reflected in the modest increase in the load factor.

Disturbance rejection produces the largest deviation in RMS tracking error, as turbulence pushes the aircraft away from the reference path. Nevertheless, the controller guides it back smoothly, and the maximum load factor deviation remains small. Sensor attenuation has a noticeable effect on the controller, increasing the control effort by about 10%. This actuator activity leads to a slightly increased maximum load factor deviation, but all metrics remain within the required limits.

Finally, with an intentional 80% error in the control effectiveness matrix, the controller maintains tracking performance comparable to the baseline case. The maximum load factor deviation is higher, however, given the similar control effort, this appears to result from a single manoeuvre rather than a systematic issue. These results confirm INDI’s inherent robustness to model uncertainties. Overall, the controller satisfies all requirements and demonstrates resilience to the main real-world effects that degrade performance.

**Table 10.3:** Controller performance evaluation

| Category | Metric | Description | Unit | Ideal | Realistic |
|---|---|---|---|---|---|
| Command tracking | RMSer | RMS error for tracking | m | 0.40 | 0.57 |
| | RMSur | RMS input for tracking | rad | 8.09e-02 | 7.91e-02 |
| | Max/Min $n$ | Max experienced $n$ dev. | - | 0.089 | 0.12 |
| | Sink Rate | Sink rate during touchdown | ft/s | -1.87 | -1.79 |
| Disturbance rejection | RMSed | RMS error due to disturbance | m | 0.69 | 0.79 |
| | RMSud | RMS input due to disturbance | rad | 8.05e-02 | 8.02e-02 |
| | Max/Min $n$ | Max experienced $n$ dev. | - | 0.086 | 0.11 |
| | Sink Rate | Sink rate during touchdown | ft/s | -4.75 | -2.76 |
| Sensor attenuation | RMSen | RMS error due to noise and bias | m | 0.37 | 0.66 |
| | RMSun | RMS input due to noise and bias | rad | 8.77e-02 | 8.79e-02 |
| | Max/Min $n$ | Max experienced dev. $n$ | - | 0.083 | 0.14 |
| | Sink Rate | Sink rate during touchdown | ft/s | -1.71 | -1.67 |
| Model uncertainty | RMSen | RMS error due to model uncertainty | m | 0.41 | 0.56 |
| | RMSun | RMS input due to model uncertainty | rad | 8.09e-02 | 7.96e-02 |
| | Max/Min $n$ | Max experienced $n$ dev. | - | 0.096 | 0.15 |
| | Sink Rate | Sink rate during touchdown | ft/s | -1.88 | -1.18 |

To further assess the controller’s performance, all requirements as defined in Table 7.7 are evaluated. The first set of requirements concerns the velocity constraints. The approach speed is designed as 55 m/s IAS. Figure 10.1 shows the true airspeed (TAS) and indicated airspeed (IAS) during landing, along with the flare command and the first allowable landing position. Both velocity trajectories remain below the maximum flare velocity $V_{FL}$ and the maximum touchdown velocity $V_{TD}$, satisfying REQ-V-2 and REQ-V-3. A flight path angle of -3° is used for the design of the reference path during the approach phase, compliant with REQ-FP-3. The flare command occurs at 55 ft, which lies within the prescribed range, while the actual flare begins at 40 ft, consistent with REQ-FP-2. Finally, the touchdown point is located 343 m ($\approx 1125$ ft) behind the flare command point, which lies within the longitudinal bounds of REQ-FP-5.

The remaining requirements can be assessed either by direct computation or are inherently satisfied, as they were explicitly used in the design of the reference path and controller. Table 10.4 summarises all

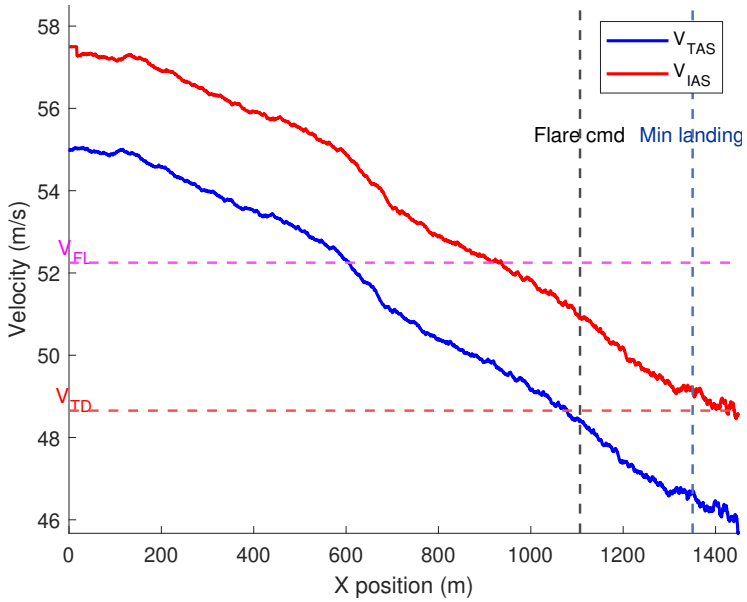


**Figure 10.1:** TAS and IAS during landing

requirements, the corresponding verification method, and whether they are met. As shown, all requirements are satisfied. The final sink rate of -2.54 ft/s lies within the desirable range of REQ-V-4, while the minimum load factor remains at 0.90, thereby satisfying REQ-V-5. Finally, the elevator deflection and rate remain within the prescribed limits.

**Table 10.4:** Requirement compliance summary

| Requirement | Limit | How | Satisfied |
|---|---|---|---|
| REQ-V-1 | $V_A \geq 1.3V_{S_{approach}}$ | Trim velocity | ✓ |
| REQ-V-2 | Max $V_{FL} \approx 0.95V_A$ | Figure 10.1 | ✓ |
| REQ-V-3 | Max $V_{TD} = 1.15V_{S_{approach}}$ | Figure 10.1 | ✓ |
| REQ-V-4 | Max $\dot{h}_{final}$ = [-1 to -10] ft/s | $\dot{h}_{final}$ =-2.54 ft/s | ✓ |
| REQ-V-5 | Max load factor = [0.8 - 1.2] | Min $n$ = 0.90, max $n$ = 1.09 | ✓ |
| REQ-FP-1 | Flare command altitude [50 to 60] ft | Reference path driver | ✓ |
| REQ-FP-2 | Flare start altitude [30 to 40] ft | Reference path driver | ✓ |
| REQ-FP-3 | Flight path angle [-2° to -3°] | Reference path driver | ✓ |
| REQ-FP-4 | Lateral position approach $\pm 1.5°$ of centerline | No deviations | ✓ |
| REQ-FP-5 | Longitudinal position [800 to 2300] ft from flare command | Figure 10.1 | ✓ |
| REQ-FP-6 | Lateral position landing [$\pm 27$] ft from centerline | No deviations | ✓ |
| REQ-PL-1 | Aileron deflection limits [-19° to 15°] | Used in trim | ✓ |
| REQ-PL-2 | Elevator deflection limits [-17° to 15°] | Max = $-0.5°$, Min = -9.1° | ✓ |
| REQ-PL-3 | Rudder deflection limits [-22° to 22°] | Used in trim | ✓ |
| REQ-PL-4 | Actuator rates $< 19.7°/s$ | Max rate is $19.2°/s$ | ✓ |

# 11

# Conclusions & Recommendations

This chapter presents the conclusions and recommendations for this report. The objective of this research was to design and evaluate an Incremental Nonlinear Dynamic Inversion (INDI) controller for autoland of the PH-LAB Cessna Citation aircraft in a simulated environment, with particular focus on stability, performance degradation, and mitigation strategies. The findings demonstrate that performance degradation caused by delays can be reduced, highlighting the potential of INDI for autoland applications.

A review of recent INDI developments highlighted the importance of accurate and fast acceleration feedback for performance. Hybrid INDI, which fuses model-based and sensor-based feedback, was identified as a promising approach in the absence of an angular accelerometer. The model-based contribution captures high-frequency dynamics, while the sensor-based part ensures robustness to model mismatches. This eliminates the need to take the derivative of the pitch rate signal, which amplifies the noise in the acceleration feedback signal.

One of the most important identified limiting factors for performance was the delay in altitude measurements from the Digital Air Data Computer (DADC). In turbulent conditions, this delay caused aggressive elevator deflection commands, leading to oscillatory elevator behaviour, degraded path tracking, and excessive load factor deviations. To mitigate these effects, a new IMU-based altitude estimation was developed. The method combines a coordinate transformation and double integration of the linear accelerometer measurements from the IMU, which are subject to much smaller delays. To address the cumulative errors inherent to the double integration, a Kalman filter was applied to fuse this estimate with the delayed DADC signal, providing corrections. This solution smoothed elevator deflections, reduced load factor deviations, and improved path-following accuracy.

Actuator delays produced similar oscillatory behaviour in the elevator. Pseudo Control Hedging (PCH) mitigated these delays to some extent, but it is not effective against sensor delays. In particular, synchronisation between elevator deflection and angular acceleration feedback is important for performance. To address this, a cross-correlation-based delay estimator was introduced to determine the delay between these signals. The estimator successfully identified delays during controlled manoeuvres, allowing for compensation in the elevator deflection feedback. Variable delays did not introduce additional challenges, as their magnitude was small compared to the nominal delay.

The INDI controller demonstrated that it can maintain performance under challenging conditions. It successfully followed longitudinal approach paths, landed safely in turbulence, and tolerated delays larger than those reported for this aircraft in prior studies. Moreover, all operational requirements, including landing performance, flight path computation, and actuator constraints, were satisfied. When subjected to increased IMU delays, the controller required slightly higher control effort, but only gradual performance degradation. Similarly, growing actuator delays were manageable until the time delay margin was reached. Severe turbulence increased load factor deviations and occasionally led to deviations in the final sink rate, though performance generally remained acceptable until high turbulence levels were reached, where stability may be compromised.

While the research objective has been fulfilled, some limitations remain. The control has been limited to the longitudinal axis, leaving lateral dynamics and the challenge of coordinated turns, crosswind landings, and curved approach paths for future development. Likewise, the ground effect and touchdown dynamics

have not been included. These factors would increase the validity of the controller and the trust in a real-world application. Moreover, the IMU-DADC fusion approach could be expanded with radar altimeter measurements to further increase reliability or reduce the delay. Finally, if the actuator delay is too large for PCH, a different approach such as adaptive or learning-based extensions could be considered.

Overall, the results show that the main research question: ”Which measures are required to successfully mitigate the causes of performance degradation and stability issues in an INDI autoland system?” has been answered. The combination of hybrid INDI, Pseudo Control Hedging, delay estimation, IMU-based altitude estimation, and sensor fusion mitigates the primary causes limiting performance and stability. Along the way, all sub-questions were addressed, from understanding the state-of-the-art and defining autoland requirements, to identifying the causes of performance degradation and finding methods for their mitigation. These findings demonstrate the potential of the proposed framework for practical autoland applications and contribute to safer landings, helping reduce the risk of incidents during approach and touchdown.

# References


[1] Christian Weiser et al. “Flight Testing Total Energy Control Autopilot Functionalities for High Altitude Aircraft”. en. In: *ResearchGate*. ISSN: 2024-2204. 2024. URL: https://www.researchgate.net/publication/377273718_Flight_Testing_Total_Energy_Control_Autopilot_Functionalities_for_High_Altitude_Aircraft (visited on 03/06/2025).

[2] EASA. *Annual Safety Review 2024 | EASA*. en. July 2024. URL: https://www.easa.europa.eu/en/document-library/general-publications/annual-safety-review-2024 (visited on 02/19/2025).

[3] R. C. van ’t Veld. “Incremental Nonlinear Dynamic Inversion Flight Control”. en. In: (2016). URL: https://repository.tudelft.nl/record/uuid:f85a9c88-7bdb-42cd-a01c-aa85251d365c (visited on 02/06/2025).

[4] Christopher Miller. “Nonlinear Dynamic Inversion Baseline Control Law: Architecture and Performance Predictions”. en. In: *AIAA Guidance, Navigation, and Control Conference*. Portland, Oregon: American Institute of Aeronautics and Astronautics, Aug. 2011. DOI: 10.2514/6.2011-6467. (Visited on 02/06/2025).

[5] Rasmus Steffensen et al. “Nonlinear Dynamic Inversion with Actuator Dynamics: An Incremental Control Perspective”. In: *Journal of Guidance, Control, and Dynamics* 46.4 (Apr. 2023). Publisher: American Institute of Aeronautics and Astronautics, pp. 709–717. DOI: 10.2514/1.G007079. URL: https://arc.aiaa.org/doi/10.2514/1.G007079 (visited on 02/04/2025).

[6] Xuerui Wang et al. “Stability Analysis for Incremental Nonlinear Dynamic Inversion Control”. In: *Journal of Guidance, Control, and Dynamics* 42.5 (May 2019). Publisher: American Institute of Aeronautics and Astronautics, pp. 1116–1129. DOI: 10.2514/1.G003791. (Visited on 10/07/2025).

[7] Fabian Grondman et al. “Design and Flight Testing of Incremental Nonlinear Dynamic Inversion-based Control Laws for a Passenger Aircraft”. In: *2018 AIAA Guidance, Navigation, and Control Conference*. AIAA SciTech Forum. American Institute of Aeronautics and Astronautics, Jan. 2018. DOI: 10.2514/6.2018-0385. (Visited on 02/06/2025).

[8] Andreas Steinleitner et al. “Automatic Take-Off and Landing of Tailwheel Aircraft with Incremental Nonlinear Dynamic Inversion”. In: *AIAA SCITECH 2022 Forum*. American Institute of Aeronautics and Astronautics, 2022. DOI: 10.2514/6.2022-1228. (Visited on 02/18/2025).

[9] Yingzhi Huang et al. “Time-Delay Margin and Robustness of Incremental Nonlinear Dynamic Inversion Control”. In: *Journal of Guidance, Control, and Dynamics* 45.2 (2022), pp. 394–404. DOI: 10.2514/1.G006024. (Visited on 02/15/2025).

[10] Shaojie Zhang et al. “Incremental Nonlinear Dynamic Inversion Attitude Control for Helicopter with Actuator Delay and Saturation”. en. In: *Multidisciplinary Digital Publishing Institute* 10.6 (June 2023), p. 521. DOI: 10.3390/aerospace10060521. (Visited on 02/05/2025).

[11] Hoijo Jeong et al. “Hybrid Incremental Nonlinear Dynamic Inversion-based Control of UAV in Urban Wind Environment”. en. In: *International Journal of Control, Automation and Systems* 22.12 (Dec. 2024), pp. 3653–3665. DOI: 10.1007/s12555-024-0539-3. (Visited on 02/26/2025).

[12] Ole Pfeifle et al. “Cascaded Incremental Nonlinear Dynamic Inversion for Three-Dimensional Spline-Tracking with Wind Compensation”. In: *Journal of Guidance, Control, and Dynamics* 44.8 (2021), pp. 1559–1571. DOI: 10.2514/1.G005785. (Visited on 02/18/2025).

[13] Ehab Safwat et al. “Robustness Analysis of Modified Incremental Nonlinear Dynamic Inversion for Small UAVs”. en. In: *Automatic Control and Computer Sciences* 54.2 (Mar. 2020), pp. 128–138. DOI: 10.3103/S0146411620020078. (Visited on 02/25/2025).

[14] Salahudden Salahudden et al. “Decoupled incremental nonlinear dynamic inversion control for aircraft autonomous landing with ground-effect”. en. In: *Aerospace Science and Technology* 149 (June 2024), p. 109156. DOI: 10.1016/j.ast.2024.109156. (Visited on 02/13/2025).

[15] Noah Stam et al. “Adaptive Dynamic Incremental Nonlinear Control Allocation for Aircraft With Innovative Control Effectors”. In: *AIAA SCITECH 2025 Forum*. AIAA SciTech Forum. American Institute of Aeronautics and Astronautics, Jan. 2025. DOI: 10.2514/6.2025-0082. URL: https://arc.aiaa.org/doi/10.2514/6.2025-0082 (visited on 02/05/2025).

[16] Beau Smit et al. “Adaptive Incremental Nonlinear Dynamic Inversion Flight Control for Consistent Handling Qualities”. In: *AIAA SCITECH 2022 Forum*. AIAA SciTech Forum. American Institute of Aeronautics and Astronautics, Dec. 2021. DOI: 10.2514/6.2022-1394. URL: https://arc.aiaa.org/doi/10.2514/6.2022-1394 (visited on 02/10/2025).

[17] Ewoud J. J. Smeur et al. *Adaptive Incremental Nonlinear Dynamic Inversion for Attitude Control of Micro Air Vehicles | Journal of Guidance, Control, and Dynamics*. 2016. URL: https://arc-aiaa-org.tudelft.idm.oclc.org/doi/full/10.2514/1.G001490 (visited on 02/05/2025).

[18] Chong-Sup Kim et al. “Stability Margin and Structural Coupling Analysis of a Hybrid INDI Control for the Fighter Aircraft”. en. In: *International Journal of Aeronautical and Space Sciences* 22.5 (Oct. 2021), pp. 1154–1169. DOI: 10.1007/s42405-021-00394-8. (Visited on 03/05/2025).

[19] Y. Kumtepe et al. “Flight Control Law Design using Hybrid Incremental Nonlinear Dynamic Inversion”. en. In: *AIAA SciTech Forum* (2022). DOI: 10.2514/6.2022-1597. (Visited on 02/26/2025).

[20] Yeji Kim et al. “Incremental Nonlinear Dynamic Inversion-based Fault-Tolerant Guidance for UAV”. In: *AIAA SCITECH 2024 Forum*. American Institute of Aeronautics and Astronautics, Jan. 2024. DOI: 10.2514/6.2024-2564. (Visited on 02/14/2025).

[21] S. Sieberling et al. “Robust Flight Control Using Incremental Nonlinear Dynamic Inversion and Angular Acceleration Prediction”. In: *Journal of Guidance, Control, and Dynamics* 33.6 (2010), pp. 1732–1742. DOI: 10.2514/1.49978. (Visited on 02/10/2025).

[22] Zhidong Lu et al. *Stability and Performance Analysis for SISO Incremental Flight Control*. Nov. 2020. DOI: 10.48550/arXiv.2012.00129. URL: http://arxiv.org/abs/2012.00129 (visited on 02/14/2025).

[23] Ewoud J. J. Smeur et al. “Prioritized Control Allocation for Quadrotors Subject to Saturation”. en. In: (2017). URL: https://repository.tudelft.nl/record/uuid:54c4659a-3a6d-4d44-873d-aec6ae5e2376 (visited on 02/17/2025).

[24] Thomas Lombaerts et al. “Design and Flight Testing of Nonlinear Autoflight Control Laws”. en. In: *ResearchGate*. Aug. 2012. DOI: 10.2514/6.2012-4982. (Visited on 03/07/2025).

[25] Tito J. Ludeña Cervantes et al. “Flight Control Design using Incremental Nonlinear Dynamic Inversion with Fixed-lag Smoothing Estimation”. en. In: *International Journal of Aeronautical and Space Sciences* 21.4 (Dec. 2020), pp. 1047–1058. DOI: 10.1007/s42405-020-00273-8. URL: https://doi.org/10.1007/s42405-020-00273-8 (visited on 03/07/2025).

[26] Paul Groves. *Principles of GNSS, Inertial, and Multisensor Integrated Navigation Systems, Second Edition*. en-US. 2013. URL: https://ieeexplore.ieee.org/document/9101092 (visited on 03/07/2025).

[27] I. Z. El-Hajj. “Determination of Stable Time-delay Regions in Incremental Control Systems”. en. In: (2020). URL: https://repository.tudelft.nl/record/uuid:87236104-b735-4af7-bf26-98be7b3377bc (visited on 02/11/2025).

[28] J. F. R. Koschorke. “Advanced Flight Control Design and Evaluation”. en. In: (2012). URL: https://repository.tudelft.nl/record/uuid:24c0bfab-3243-4ffa-9c96-10a4721fb23a (visited on 02/11/2025).

[29] Tito J.L. Cervantes et al. “Singular Perturbation Margin of INDI-Based Flight Control Systems With Delays”. en. In: *ResearchGate* (Mar. 2025). DOI: 10.1109/TAES.2025.3551210. (Visited on 03/19/2025).

[30] Shashiprakash Singh et al. “Automatic path planning and control design for autonomous landing of UAVs using dynamic inversion”. In: *2009 American Control Conference*. ISSN: 2378-5861. June 2009, pp. 2409–2414. DOI: 10.1109/ACC.2009.5160444. (Visited on 02/12/2025).

[31] Nicolas SedImair et al. “(PDF) Flight Testing Automatic Landing Control for Unmanned Aircraft Including Curved Approaches”. en. In: *ResearchGate* (Dec. 2024). DOI: 10.2514/1.G005917. (Visited on 02/04/2025).

[32] Robert C. Nelson. *Flight stability and automatic control*. en. 2. ed. Boston, Mass.: WCB, McGraw Hill, 1998.

[33] Gene F. Franklin et al. *Feedback control of dynamic systems*. en. 6. ed. Upper Saddle River, NJ: Pearson, Prentice-Hall, 2010.

[34] A. Muis et al. “Development of a flexible flight test instrumentation system”. en. In: (2006). URL: https://repository.tudelft.nl/record/uuid:b9e448b2-7bb3-41af-b433-7dc720a5d909 (visited on 02/25/2025).

[35] Peter Zaal et al. “Design and Certification of a Fly-by-Wire System with Minimal Impact on the Original Flight Controls”. In: *AIAA Guidance, Navigation, and Control Conference*. American Institute of Aeronautics and Astronautics, June 2012. DOI: 10.2514/6.2009-5985. (Visited on 02/25/2025).

[36] Ramesh B. Konatala et al. “Flight Testing Reinforcement Learning based Online Adaptive Flight Control Laws on CS-25 Class Aircraft”. en. In: *AIAA SCITECH 2024 Forum*. Orlando, FL: American Institute of Aeronautics and Astronautics, Jan. 2024. DOI: 10.2514/6.2024-2402. (Visited on 04/16/2025).

[37] GlobalAir.com. *CITATION II Specifications, Cabin Dimensions, Performance*. en. URL: https://www.globalair.com/aircraft-for-sale/specifications?specid=184 (visited on 03/06/2025).

[38] EASA. *Easy Access Rules for Large Aeroplanes (CS-25) - Revision from June 2022*. en. June 2022. URL: https://www.easa.europa.eu/en/document-library/easy-access-rules/easy-access-rules-large-aeroplanes-cs-25 (visited on 03/06/2025).

[39] Jan Roskam et al. *Airplane Aerodynamics And Performance*. English. DARcorporation, 1997. (Visited on 03/06/2025).

[40] Diana Siegel et al. “Development of an Autoland System for General Aviation Aircraft”. en_US. In: (Oct. 2011). Accepted: 2011-10-27T18:46:36Z. URL: https://dspace.mit.edu/handle/1721.1/66604 (visited on 03/06/2025).

[41] Myron Kayton et al. *Avionics Navigation Systems, Second Edition ( PDFDrive )*. June 1997. URL: http://archive.org/details/avionics-navigation-systems-second-edition-pdfdrive (visited on 03/06/2025).

[42] Tijmen Pollack et al. “Design and flight testing of flight control laws integrating incremental nonlinear dynamic inversion and servo current control”. In: *AIAA Scitech 2019 Forum*. AIAA SciTech Forum. American Institute of Aeronautics and Astronautics, Jan. 2019. DOI: 10.2514/6.2019-0130. (Visited on 02/14/2025).

[43] David J. Moorhouse et al. *Background Information and User Guide for MIL-F-8785C, Military Specification - Flying Qualities of Piloted Airplanes*. Tech. rep. AFWAL-TR-81-3109. Flight Dynamics Laboratory, Control Dynamics Branch, Sept. 1981, pp. 177–207.